LARGE-SCALE SWEPT-WING ICE ACCRETION MODELING IN THE NASA
GLENN ICING RESEARCH TUNNEL USING LEWICE3D

BY

BROCK DEMONT WIBERG

THESIS

Submitted in partial fulfillment of the requirements
for the degree of Master of Science in Aerospace Engineering
in the Graduate College of the
University of Illinois at Urbana-Champaign, 2013

Urbana, Illinois

Adviser:

Professor Michael B. Bragg

Abstract

The study of aircraft icing is necessary to ensure the safety of commercial, military, and general aviation aircraft. The certification of modern commercial transports requires manufacturers to demonstrate that these aircraft can safely operate during icing conditions consistent with the standards set forth by the Federal Aviation Administration (FAA). While some of these tests are performed on actual aircraft in flight, this is often very expensive and does not provide an adequately controlled matrix of test conditions. Computational tools are used throughout the design and certification of anti-ice systems. However, computational methods alone are not sufficient for aircraft certification. Icing wind tunnels are used for aircraft certification to reduce costs, provide a controlled test matrix of conditions, and validate computational icing tools.

The size of aircraft models that can be tested in icing wind tunnels is limited by the size and capability of existing facilities. Large wings, such as those found on modern narrow and wide-body commercial transports, cannot fit in existing test sections without being dramatically scaled. Two methods of scaling exist. The first involves geometrically scaling a section of the reference wing to fit inside the tunnel test section and then scaling the icing conditions in order to maintain icing similitude. The second method maintains the full-scale leading edge of the reference geometry but replaces the aft section of the wing with a tail that is designed to produce similar flow around the leading edge but with a considerably shorter chord length, reducing model size and blockage. This type of model is called a hybrid and is used to generate full-scale ice shapes so that, in the simplest cases, no icing scaling is necessary. However, the methods can be combined so that the hybrid model design is used to maintain geometric similitude while icing scaling is employed to account for differences in pressure, velocity, or other conditions.

Modern commercial transport aircraft have large, swept wings. While a broad set of experimental data exist in the literature for airfoil and straight wing icing, there is a distinct lack of data for large, swept wings. Such data is needed in order to better understand the 3D icing physics on swept wings and to allow computational tools to be developed and validated for 3D ice features such as scallops.

In this thesis, computational tools were used to better understand the flow over a large-scale, swept-wing, hybrid model mounted vertically in the NASA Glenn Icing Research Tunnel (IRT). Fluent, a commercial

CFD code, was used to calculate flows around the flapped-hybrid model in the IRT, mounted with the root at the floor and the tip at the ceiling of the test section. Inviscid analysis reveals that the upwash ahead of the model causes the local lift coefficient to increase significantly across the swept model due to the effect of the floor and ceiling. This change in spanwise loading is shown to move the attachment line location farther down the leading edge for stations on the model which are farther outboard. Two techniques for controlling this effect are explored. 1) A flap with three spanwise segments is shown to be ineffective in controlling the spanwise load distribution on the swept model with aspect ratio near unity. The effectiveness improves as aspect ratio is increased, but increasing the aspect ratio requires significant geometric scaling, resulting in limited applicability to large-scale models. 2) Twisting the model is shown to be an effective method of reducing the effective angle of attack across the model, compensating for the upwash and making the load distribution on the model more uniform. Twist adds complexity to the model and may not be necessary for producing quality ice shapes in the region of interest on the hybrid model, depending on the objectives of the research. LEWICE3D was used to simulate droplet impingement and ice accretion on the swept model in the IRT test section. Attachment line location is shown to be the primary driver of icing similarity. It is shown that on the flapped-hybrid model, the attachment line can be uniformly shifted on the leading edge by changing the angle of attack or flap deflection. This results in a range of angle of attack and flap angle combinations (α-δ pairs) corresponding to a given attachment line location at the tunnel centerline. For a wind tunnel test at local elevation, it is shown that the heat transfer coefficient will by higher due to the increased density as compared to the in-flight icing conditions at altitude. A similitude method is applied to the hybrid model and the resulting ice shapes are compared. Finally, it is shown that for the droplet size considered, if the attachment line is matched, the model can be operated with the leading edge at an angle of attack other than that of the flight baseline and still produce ice shapes representative of the reference ice shapes generated on the baseline aircraft in free air. Operating at a higher angle of attack with lower flap angle is shown to reduce the overall model lift coefficient and the spanwise variation in attachment line position and, therefore, ice shape.

"I will give unto the children of men line upon line,

precept upon precept, here a little and there a little..."

<div align="right">2 Nephi 28:30</div>

Acknowledgments

A sincere thank you to all those who have helped me as I have pursued a Master's degree and completed the research contained in this thesis. While an exhaustive list can not be attempted here, I hope my gratitude is evident and that I have taken the time to reciprocate the love and support you have shown me.

Thank you to my parents, Brent and Kathee Wiberg, for instilling in me a curiosity and an understanding of hard work and persistence. You truly understand the concept of teaching correct principles and letting your children govern themselves. Any accomplishments I may achieve are ours to share.

Thanks also to my wife, Jashley, for patiently enduring time apart for many years as I have pursued my education. You brightened the journey with your sweetness and optimism. You made it a blessing to come home at night, no matter how late. No man has a better wife than me and no son a better mother than Bryson.

I would also like to thank Prof. Michael Bragg for his willingness to take of what little time he has to mentor his students. Few could, in addition to serving in his various administrative capacities, continue actively in significant research interests, and no one could do it as remarkably well. Thanks for keeping the emphasis on learning and research when it would have been perfectly reasonable to have put your focus elsewhere.

Thank you to the team at the University of Illinois at Urbana-Champaign including Brian Woodard, Gustavo Fujiwara, and Chris Triphahn. I would also like to acknowledge the help of Andy Broeren of NASA Glenn, Ben Paul, Adam Malone, and John Vassberg of the Boeing Company, and Professor Eric Loth from the University of Virginia for their support and guidance in completing this work. A special thanks to Colin Bidwell, also of NASA Glenn, for his generous and extensive help with LEWICE3D.

Table of Contents

List of Tables

List of Figures

Nomenclature

Symbols

A_c =   accumulation parameter

b =   wing span

c =   chord length

C_l =   sectional lift coefficient

C_L =   3D lift coefficient

C_{m0} =   sectional zero-lift pitching moment coefficient at $c/4$

C_p =   2D pressure coefficient

C_P =   3D pressure coefficient

d =   twice the leading-edge radius of curvature

h_c =   convective heat transfer coefficient

k =   turbulent kinetic energy

K_0 =   modified inertia parameter

M =   Mach number

n_0 =   stagnation point freezing fraction

Nu =   Nusselt number

P =   static pressure

P_t =   stagnation pressure

q =   dynamic pressure

R =   ideal gas constant of air

Re =   Reynolds number

s =   wrap distance or arc length measured from the hilite

T =   static temperature

V =   freestream velocity

We	=	Weber number
x	=	Cartesian coordinate with axis pointing from nose to tail of aircraft
y	=	Cartesian coordinate with axis pointing from center of aircraft to right wing
z	=	Cartesian coordinate with right-handed axis normal to the xy-plane
α	=	angle of attack
β	=	impingement efficiency
γ	=	hybrid nose droop angle
γ_{air}	=	specific heat ratio of air
δ	=	flap deflection angle
η	=	ratio of y position to wing semispan, $b/2$
θ	=	ice horn angle
Λ	=	wing sweep angle
λ	=	wing taper ratio
μ	=	dynamic viscosity
ν	=	kinematic viscosity
ρ	=	freestream air density
τ	=	icing exposure time
ω	=	specific turbulence dissipation rate

Subscripts

a	=	property of air
b	=	in the CRM body-fixed reference frame
f	=	flap element
fs	=	full-scale
h	=	hybrid element
le	=	leading edge
me	=	main element
sw	=	parallel to the freestream
2D	=	2D parameter or parameter from the plane whose normal is tangent to the wing leading edge
3D	=	3D parameter

∞	=	freestream condition
$\parallel$	=	parallel to the wing leading-edge tangent line
$\perp$	=	normal to the wing leading-edge tangent line

Abbreviations and Acronyms

AIAA	=	American Institute of Aeronautics and Astronautics
AR	=	Aspect Ratio
CFB	=	Clean Flight Baseline
CFD	=	Computational Fluid Dynamics
CFR	=	Code of Federal Regulations
CRM	=	Common Research Model
CRM65	=	65% Scale Common Research Model
IB	=	Inboard
IFB	=	Iced Flight Baseline
IPS	=	Ice Protection System
IRT	=	Icing Research Tunnel
LWC	=	Liquid Water Content
MS	=	Midspan
MVD	=	Median Volume Diameter
NACA	=	National Advisory Committee for Aeronautics
NASA	=	National Aeronautics and Space Administration
NRA	=	NASA Research Announcement
NS	=	Navier-Stokes
OB	=	Outboard
ONERA	=	Office National d'Études et de Recherches Aérospatiales or The French Aerospace Lab
PLWC	=	Portion Liquid Water Content
RANS	=	Reynolds Averaged Navier-Stokes
SF	=	Scale Factor
SST	=	Shear Stress Transport
TWE	=	Total Water Exposure

UIUC   =   University of Illinois at Urbana-Champaign

WB   =   Wing-Body

Chapter 1

Introduction

1.1 Motivation

The study of aircraft icing is critical to the safe operation of commercial, military, and general aviation aircraft. The formation of ice on lifting surfaces simultaneously decreases lift and increases drag, presenting serious risk to aircraft safety by effectively shrinking the flight envelope.

Aircraft icing research began in 1928 when the National Advisory Committee for Aeronautics (NACA) approved Research Authorization 247 to determine the conditions under which ice forms on the structures of aircraft [1]. This first look at aircraft icing resulted from the U.S. Air Mail Service's frequent encounters with ice during around-the-clock operations between New York and Chicago. Initial testing required research pilots to seek out clouds where icing conditions were likely to be encountered with their instrumented Vought VE-7 aircraft. The need for a laboratory environment that would allow better control of icing conditions than was available during flight tests was recognized immediately. Laboratory research followed in that same year when a refrigerated wind tunnel began operations at the Langley Research Center. At the end of World War II, NACA built the Icing Research Tunnel (IRT) at the Lewis Research Center. The main focus of icing research at that time remained in support of the war effort with the goal of measuring the impact of ice on overall aircraft performance. In 1958 the National Aeronautics and Space Administration (NASA) replaced its predecessor, NACA. The modern icing research program was organized at NASA Lewis in 1978 and the Lewis Research Center was renamed the NASA John H. Glenn Research Center in 1999 [2]. The IRT has had several upgrades but is still used today to simulate icing conditions by injecting supercooled water droplets into refrigerated air as it is circulated through the tunnel test section.

In 1964 the Federal Aviation Administration (FAA) issued Appendix C of Title 14 Parts 25 and 29 in the U.S. Code of Federal Regulations (CFR) which sets standards for selecting values of icing related cloud variables for the design of in-flight ice protection systems (IPS) for aircraft and rotorcraft [3]. While these regulations are important for setting forth a standard collection of icing conditions for use in certification, it is a common misconception that Title 14 Appendix C specifies methods by which one must demonstrate

compliance with federal regulations. The certification of an aircraft is highly specific to the type of craft and its intended use. A manufacturer must work directly with FAA certification engineers to determine a plan for demonstrating compliance with federal regulations. Despite this, there are non-mandatory guidelines available in Advisory Circular 25-25 which describe "an acceptable means for showing compliance with the airplane certification requirements related to performance and handling characteristics of transport category airplanes for flight in the icing conditions defined in appendix C of Title 14, CFR part 25" [4].

Because the precise methods used to certify an aircraft are not mandated, a designer will most often choose a method that minimizes the overall cost of the certification program while ensuring that compliance is demonstrated. A manufacturer certifying a small, general aviation aircraft may choose to perform actual flight tests to obtain ice accretions and determine aerodynamic and handling characteristics with iced surfaces because doing so is relatively inexpensive and straight forward. However, flight testing a large commercial transport represents a huge cost due to the test aircraft and operations as well as the expense of making changes to achieve compliance late in the design process. Manufacturers of larger aircraft need to test anti-ice systems early so that these expenses can be mitigated. Additionally, flight testing does not provide an adequately controlled matrix of test conditions for commercial aircraft certification, even when a lead aircraft is used to produce a simulated cloud. This results in a continued need for icing wind tunnel testing and has driven an effort to apply computational tools to the aircraft certification process.

The use of computational tools for icing applications began in the 1970's. Computational fluid dynamics (CFD) was used to predict the aerodynamic performance of iced airfoils. This in turn initiated an effort to experimentally validate these computations which led to the first flowfield measurements of airfoils with ice. Computational methods have continued to mature and now play an important, though indirect, role in aircraft certification and IPS design. However, computational methods alone are not sufficient for aircraft certification. It will likely be a decade or more before CFD tools can be used to accurately and consistently determine critical parameters like the maximum lift on iced wings. Thus, manufacturers rely heavily on icing wind tunnel tests to determine impingement regions, ice shapes, and to test anti-ice systems.

1.2   Previous Work

A thorough understanding of the effect of ice on airfoils and straight wings has been established as a result of research conducted in recent decades. A detailed summary of icing performance effects on airfoils and straight wings based on results available in the public domain was provided by Lynch and Khodadoust [5]. The work carefully reviewed these results in the context of aerodynamic performance and control degradation

caused by ice accretions. Bragg et al. [2] identified characteristics of the flowfield leading to the associated performance effects on these airfoils and straight wings. In addition, four classes of ice accretions were proposed based on the flowfield features generated by the ice which set the context for an international collaboration seeking to provide high-fidelity, full-scale aerodynamic data for iced airfoils. This six phase research effort used the NACA 23012 airfoil in icing wind tunnel and aerodynamic wind tunnel experiments. Ice accretions on both subscale and full-scale models were generated in the IRT at NASA Glenn. Subsequent aerodynamic experiments were performed at the ONERA F1 pressurized wind tunnel using a 6 ft. (1.83 m) chord wing with NACA 23012 section and high-fidelity, 3D castings of the previously generated ice accretions. This research effort, in addition to providing high-fidelity aerodynamic data, resulted in validated subscale model simulation methods that produce full-scale aerodynamic characteristics.

In a more recent work, Diebold et al. [6] proposed a classification system for ice shapes on 3D swept wings similar to the classification of Bragg et al. [2] for airfoils and identified areas where more research is required to fully understand swept-wing icing effects. This classification system serves as a starting point for the research on swept-wing aerodynamics with ice shapes that is discussed in Section 1.3.

Because wind tunnel testing is crucial to aircraft certification, but the size of models that can be tested in the icing tunnels is limited to the physical dimensions of existing facilities, experimental scaling techniques have been developed. One such technique is to scale the airfoil geometrically as in traditional aerodynamic wind tunnel testing. This in turn requires that the test conditions be changed in order to scale the ice accretions themselves. The tunnel conditions can also be adjusted to account for other tunnel limitations such as maximum test section velocity. Anderson [7] presents an overview of these methods, experimental evaluation, and resources for performing similitude calculations.

Another technique for generating ice shapes experimentally - and that which is being used in the current project - is to create an airfoil that retains the full-scale leading edge of the reference airfoil but with a shorter, redesigned aft section. These airfoils, called hybrids, are carefully designed so that the flow in the vicinity of the leading edge matches closely that of the full-scale airfoil at a given design condition. This allows a physically smaller model to be used in the wind tunnel while generating full-scale ice shapes. In 1956, Uwe von Glahn tested a NACA 65(1)-212 airfoil along with truncated models in the NACA Lewis IRT to determine the effect on velocity distribution and impingement characteristics [8]. Two subscale airfoil sections were created with full-scale leading edges by truncating the airfoil at 50% and 30% chord and attaching a simple sliding flap system. Even with this crude system the results showed that by deflecting the flap the local velocity distribution in the impingement region could be made substantially the same as that of the full-chord airfoil [8]. By maintaining a full-scale leading edge only to the extents of the droplet

impingement region, Saeed et al. [9] showed that an aft section can be designed so that a flap is not needed for a specific test case. While a modern hybrid airfoil is carefully designed for a specific angle of attack, α, and set of flight conditions, the addition of a flap is still common to extend its useful range to off-design cases. Saeed et al. [10, 11] set forth methods for designing truncated airfoils to simulate full-scale ice accretions through a range of α or sectional lift coefficient, C_l. These design methods were validated experimentally using a half-scale business jet 2D model in the NASA Lewis IRT [12]. Fujiwara et al. [13] highlighted additional benefits of using hybrid models beyond physical size reduction including reduced aerodynamic loading and tunnel blockage as compared to the full-scale airfoil.

Despite the extensive base of literature on the impact of ice accretions on airfoil aerodynamics and the use of hybrid airfoils for full-scale icing simulation, the current understanding of these concepts does not extend into 3D swept wings. There is a distinct lack of data in the literature for icing on 3D swept wings. The question remains as to how well the current understanding of the aerodynamics of iced airfoils and straight wings will apply to 3D swept wings and how existing expertise may be used to further this understanding.

1.3 Large-Scale Swept-Wing Ice Accretion Project

In order to better understand aircraft icing on large-scale, swept wings, NASA, the FAA, The French Aerospace Lab (ONERA), the University of Illinois at Urbana-Champaign (UIUC), and the Boeing Company have embarked on a collaborative, seven-phase research project [14]. This project, modeled after the international collaboration that studied icing on airfoils and straight wings, seeks to expand the understanding of highly 3D ice accretions and their corresponding aerodynamic effects. The project will be used to validate both experimental and computational methods. To this end, ice accretion and aerodynamic experiments, CFD simulations, and LEWICE3D simulations will be performed. The effort is currently underway with significant progress already made in several of the initial phases. Broeren et al. [14] provided an overview of this project and a summary of the progress as of May 2013.

A large model with a swept-wing configuration that is representative of a modern transport aircraft was needed as a baseline for this project. Additionally, the model could not be proprietary or export controlled so that the work performed could benefit all parties involved and be used to enhance aircraft safety domestically and abroad. The Common Research Model (CRM) was selected during Phase II as the baseline model [14]. A body of literature for the CRM is available in the public domain including the model geometry [15], computational results [16–20], and experimental data [21, 22]. This information makes the

CRM a convenient baseline model and will allow the contributions from this project to be utilized more effectively by both academics and aircraft manufacturers.

The CRM was designed by Boeing as part of a collaboration with NASA [15]. The CRM features a fuselage similar to a modern wide-body aircraft with a transonic wing having a quarter-chord sweep of 35 deg. The supercritical wing was designed for a cruise Mach number of $M = 0.85$. The aircraft body extends to 10% semispan with a yehudi break at 37% semispan and 8 deg. of washout from side-of-body to tip. The full configuration includes a body, wing, nacelle, pylon, and horizontal tail. The wing was designed to perform well with and without the nacelle and pylon. The full configuration including the horizontal tail and nacelle-pylon group is shown in Figure 1.1. Vassberg et al. [15] described the details of the CRM layout and aerodynamic design. The CRM design was used to produce test articles on which aerodynamic tests were performed as part of the initial collaboration [15, 21, 22]. The CRM has also been used in the AIAA Drag Prediction Workshops [18, 23]. Table 1.1 compares the CRM to wide-body commercial transport aircraft in use today.
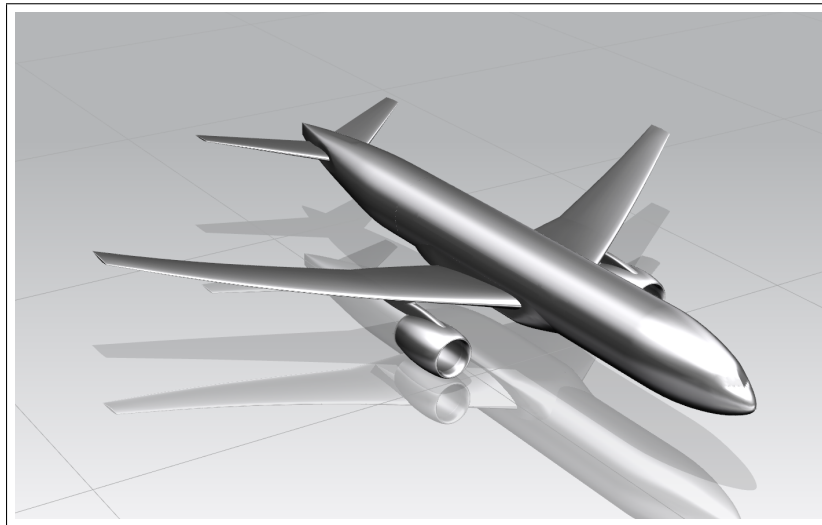
Figure 1.1: Full Configuration of the Common Research Model [15]

While the CRM offered many distinct advantages as the baseline model, one challenge of the CRM model is its large physical size. The full-scale CRM, with a wing span of 192.8 ft. (58.8 m), posed two major problems. First, to effectively create ice shapes representative of the full-scale ice shapes in the NASA IRT, hybrid models need to be designed as discussed in Section 1.2. These hybrid models retain the full-scale leading edge of the reference wing. The larger the reference geometry, the more aggressive the hybrid design must be in order to fit in the existing icing tunnel test section. This can cause problems during testing

5

Table 1.1: Comparison of the Common Research Model with Existing Wide-Body Aircraft[†], Adapted from Broeren et al. [14]

Aircraft	Span (ft.)	Mean Aerodynamic Chord (ft.)	Area (ft.^{2})	Aspect Ratio	Taper Ratio	Quarter Chord Sweep (deg.)
CRM	192.8	23.0	4,130	9.0	0.28	35
Airbus A330-200	198.0	23.9	3,892	9.5	0.22	30
Boeing 747-400	211.4	29.8	5,417	7.7	0.28	37
Boeing 777-200	199.9	26.5	4,389	8.7	0.27	31
Boeing 787-9	197.0	20.6	3,880	9.6	0.18	32

† Data for existing wide-body airplanes was compiled from publicly available sources that may use different conventions to define the geometric parameters.

because more aggressive models are more likely to have adverse effects such as flow separation. The second problem is more subtle in that, while a clean wing can easily be scaled for any size tunnel, an ice shape casting will be attached to the wing model later in the project when the iced wing is tested in the ONERA F1 tunnel. The small features of the full-scale ice shapes for a model of the original CRM's size would not be accurately represented when scaled small enough for the tunnel. These combined problems led the team to select a 65% scaled version of the CRM design (CRM65) as the baseline model for the project. The CRM65 is comparable in size to a modern single-aisle commercial transport aircraft. Table 1.2 compares the CRM65 with existing narrow-body commercial jetliners. Because the 65% scaled CRM is still representative of a large commercial transport airplane, risks associated with an excessively large baseline model were avoided while still meeting the requirements of the program. A more detailed description of the CRM65 as well as the aerodynamic and geometric parameters are given in Section 2.1.1.

Table 1.2: Comparison of the 65% Scaled Common Research Model with Existing Narrow-Body Aircraft[†], Adapted from Broeren et al. [14]

Aircraft	Span (ft.)	Mean Aerodynamic Chord (ft.)	Area (ft.^{2})	Aspect Ratio	Taper Ratio	Quarter Chord Sweep (deg.)
CRM65	125.3	15.0	1,745	9.0	0.28	35
Airbus A320	112.0	14.1	1,320	9.5	0.21	25
Boeing 737-800	112.6	13.0	1,341	9.5	0.16	25
Boeing 757-200	124.8	16.7	1,847	7.8	0.21	25

† Data for existing narrow-body airplanes was compiled from publicly available sources that may use different conventions to define the geometric parameters.

The work presented in this thesis falls under Phase III of the Large-Scale Swept-Wing Ice Accretion Project [14] and is funded under a NASA Research Announcement (NRA). The objective of Phase III is to better understand how ice shapes on a large-scale, swept-wing can be replicated in existing icing tunnels using a hybrid model. Understanding how ice accretes on this model, and identifying key indicators in flowfields that result in successful representation of full-scale icing, is critical to the ultimate goal of performing such testing for aircraft certification as well as considering the ability of CFD to accurately model ice accretion in this environment.

The CRM65 configuration used for this research includes only the body and wing for simplicity. Three spanwise stations were selected on the wing for which wind tunnel articles will be designed, analyzed, fabricated, and eventually tested in the IRT. The design process for these wind tunnel models is being developed as part of phase III, providing a methodology for future work by aircraft manufacturers in testing anti-ice systems on large wing sections. The design of these models is the subject of Section 2.2. The ice shapes obtained from these tests will later be used to create artificial ice shapes for the test articles used in the aerodynamic testing campaign in the ONERA F1 tunnel. How these spanwise stations were selected is detailed in Section 2.1.4. The station used in the current work is located at 64% semispan and is referred to as the midspan (MS) station.

1.4 Objective

The current research presents several flowfield and icing simulations of a hybrid wing model in the IRT. These simulations were performed at conditions matching a subset of those for which baseline data sets were produced by the Boeing Company as described in Section 2.1. The goal of this study is to understand and develop the capability to produce full-scale ice shapes using a hybrid, swept-wing model with a full-scale leading edge in the IRT. Doing so requires a fundamental understanding of the flow physics of large, swept wings in the presence of tunnel walls and how such flows can be made similar to the flow on the reference wing in flight. These objectives are summarized below:

- Improve the understanding of droplet trajectories and leading-edge impingement in the presence of tunnel walls, especially for large, swept models. This implies an understanding of the underlying flow physics as the flowfield governs the droplet trajectories.

- Improve the understanding of how these characteristics impact ice formation and the resulting shape on 3D wing models while considering the limitations of computational tools in modeling 3D icing physics.

- Understand the impact of attachment line location on ice shape and evaluate its effectiveness as the primary indicator of ice shape matching for 3D swept models. Investigate the effect of angle of attack and flap angle on attachment line position.

- Develop the methodology necessary to validate 3D swept IRT model design by showing that ice shapes can be produced which are representative of the full-scale ice shapes grown in free air.

Chapter 2

Methods

In order to explore the use of hybrid models to simulate icing on large-scale, swept wings it was first necessary to select a baseline wing geometry that meets the requirements of the project. The model needed to be representative of a modern commercial transport aircraft of sufficient size to test the proposed hybrid methods but not so large as to threaten the project with undue risk. The selection process including how these conditions were met is discussed in Sections 2.1 and 2.1.1. Aerodynamic and icing analyses were then performed on this geometry to provide a baseline data set for comparison with forthcoming IRT simulations. The Boeing Company performed these analyses, generating the Clean Flight Baseline (CFB) and Iced Flight Baseline (IFB) data sets described in Sections 2.1.2 and 2.1.3. Three discrete spanwise stations of interest were then selected to represent the full wing in future icing simulations and experiments. Section 2.1.4 details the selection of these three stations, emphasizing the midspan (MS) station from which the model for the research in this thesis was designed.

An important aspect of the Large-Scale Swept-Wing Icing Project is to develop a methodology that provides a framework for aircraft manufacturers designing test articles for icing tunnel experiments. An overview of hybrid airfoils is provided in Section 2.2.1, giving context to the wing model design discussed in Section 2.2.3. The majority of the model design is performed in 2D, making simple sweep theory a necessary tool in the design methodology. Its implications in this project are summarized in Section 2.2.2 before the 3D model description is given.

Before icing simulations can be performed, a numerical flow solution is generated which provides velocity vectors for integrating droplet trajectories and pressure and temperature for icing physics. An overview of the Icing Research Tunnel (IRT) layout and the mesh topology used for these CFD simulations is provided in Section 2.3.1. Details into the 3D IRT mesh creation, mesh validation, and flow solution generation are found in Sections 2.3.2, 2.3.3, and 2.3.4, respectively. The icing simulations were performed using a parallel version of the NASA Glenn Three-Dimensional Grid Based Ice Accretion Code (LEWICE3D) [24]. A brief overview of the 2D version of this ice accretion code, known simply as LEWICE [25], is given in Section 2.4.1. This is followed by a more detailed overview of LEWICE3D in Section 2.4.2. Some important differences between

LEWICE and LEWICE3D are highlighted in Section 2.4.3 including a description of how to compare their outputs using simple sweep theory.

The chapter ends with a summary of the test conditions used for the exercises in this work. The cases were selected from the icing conditions used by Boeing to generate the CFB and IFB data sets. These conditions and the reasons for their selection are summarized in Section 2.4.4.

2.1 Baseline Wing

The Common Research Model (CRM) [15] was selected as the baseline geometry because it is a large, modern, swept-wing transport airplane that is available in the public domain. The CRM was designed by Boeing as part of a collaboration with NASA. The CRM features a fuselage similar to a modern wide-body aircraft with a transonic wing having a quarter-chord sweep of $\Lambda = 35$ deg. (see Table 1.1). The supercritical wing was designed for a cruise Mach number of $M = 0.85$ and lift coefficient of $C_L = 0.50$ at a flight Reynolds number of $Re_c = 40$ million. The aircraft body extends to 10% semispan with a yehudi break at 37% semispan and 8 deg. of washout from side-of-body to tip. The full configuration includes a body, wing, nacelle, pylon, and horizontal-tail (see Figure 1.1). The wing was designed to perform well with and without the nacelle-pylon group. The configuration used in this work does not include the horizontal tail or the nacelle-pylon assembly and is referred to as the wing-body (WB) only configuration.

2.1.1 The 65% Scale Common Research Model

To practically use the full-scale leading edge geometry from the baseline model, it was necessary to scale the CRM to 65% its original dimensions. The 65% scaled CRM (CRM65) remains a large, swept-wing transport aircraft comparable to narrow-body jetliners in use today. See Table 1.2 for a comparison of the CRM65 with modern single-aisle transport aircraft. The CRM65 has a semispan of $b/2 = 751.89$ in. (19.10 m). With a quarter-chord sweep of $\Lambda = 35$ deg., aspect ratio of $AR = 9.0$, and taper ratio of $\lambda = 0.275$, the leading-edge sweep angle is $\Lambda_{le} = 37.15$ deg. Because the CRM was designed to be comparable to a typical wide-body jetliner, this sweep angle on the CRM65 is large compared to other narrow-boy aircraft, a detail that will be important when the effects of placing a swept model in a tunnel test section are considered in Section 3.1.

In order to provide a simpler case for validation studies and to have a reference geometry representative of aft-fuselage mounted engines (such as those found on regional and business jets), a WB configuration was desired in addition to the full configuration with the nacelle-pylon group. Thus, the CRM was first designed

in the WB configuration and a nacelle-pylon assembly was added later. The more complex configuration was then checked to ensure the wing still performed as desired. This design process represents a departure from typical aircraft design but was necessary to ensure a satisfactory WB configuration. This more simple WB configuration is used as the baseline of this study. The wing model is sheared with a spanwise distribution that simulates a nominal 1G loading on the wing. This sheared-wing geometry was used in the aerodynamic and icing analyses described in the following sections.

2.1.2 Clean Flight Baseline

It was necessary to have a baseline set of icing simulations in order to successfully evaluate the quality of ice shapes that would be simulated in the IRT later in the project. Aerodynamic flow simulations must be performed before ice accretion can be modeled. To this end, Boeing [26] determined a generic set of icing mission scenarios for a typical large transport aircraft. These scenarios represent all phases of flight with conditions consistent with those of CFR Title 14 Appendix C icing clouds. Boeing then reviewed the conditions and determined that a subset of the scenarios would be adequate for determining critical ice shape and down selected to a set of icing scenarios to be used in the project. These critical icing scenarios were given case identifiers that will be used hereafter. These identifiers, the aircraft angle of attack associated with a nominal 1G loading, α, and the flight conditions which they represent are given in Table 2.1.

Table 2.1: Boeing Case Identifiers and Associated Flight Conditions

Case	Phase	α (deg.)	P (Pa)	M	$Re_{c_{\mathrm{ref}}}$
WB25	Climb	1.68	30,124	0.81	34.1M
WB33	Hold	3.67	69,702	0.36	28.7M
WB39	Hold	3.64	42,824	0.46	24.8M
WB41	Hold	4.38	84,319	0.35	32.9M
WB47	Hold	4.36	57,209	0.43	28.6M
WB71	ETOPS Hold	4.40	95,956	0.32	33.2M

The flight conditions associated with these scenarios were then used to generate a CFD flowfield on the sheared CRM65 WB configuration for each test case. The well validated, compressible Reynolds Averaged Navier-Stokes (RANS) CFD software OVERFLOW [27–30] with overset grids was used to perform these calculations. These CRM65 flow solutions were performed in free air and form the CFB used for the icing analysis described in the following section. The CFB is also very important for direct comparison with the flow simulations of the 3D-hybrid wing models in the IRT. This direct comparison allows the influence of

11

specific flow parameters on ice growth to be evaluated. Specifically, the attachment line location, sectional pressure distribution, and lift coefficient are important flowfield parameters that help in the initial design and validation of the 3D models.

2.1.3 Iced Flight Baseline

Each of the critical icing scenario missions was accompanied by a set of cloud conditions consistent with CFR Title 14 Appendix C. These conditions form the basis for the IFB analysis that was performed using a parallel version of LEWICE3D known as TRAJMC3D v2.2. A complete description of LEWICE3D is given in Section 2.4.2. A Langmuir D droplet distribution was used in these icing simulations.

While just six cases were used in the CFB aerodynamic analysis, because ice shape is also a strong function of temperature, each aerodynamic flow solution was used to perform several icing simulations at various temperatures. For this reason, a Boeing case identifier is usually followed by a temperature designation in degrees Celsius. Table 2.2 gives the icing conditions for the cases used in this thesis, WB33 T-4, WB47 T-6, and WB71 T-6. A comprehensive matrix of the critical icing scenarios with their case identifiers, CFB conditions of Table 2.1, and IFB conditions of Table 2.2 is given in Table A.1. The IFB ice shapes on the outboard section of the CRM65 wing for Case WB33 T-4 are shown in Figure 2.1 looking down the wing tip toward the fuselage.

Table 2.2: Boeing Case Identifiers and Associated Icing Conditions

Case	T (K)	LWC (g/m^3)	MVD (μm)	τ (min.)	TWE (g/m^2)
WB33 T-4	269.15	0.551	20	45	177,641
WB47 T-6	267.15	0.509	20	45	191,856
WB71 T-6	267.15	0.509	20	15	47,878

The original IFB was produced using a Boeing-modified version of LEWICE3D. This proprietary version includes some source code changes and is based on an older version of LEWICE3D (TRAJMC3D v2.2, see Section 2.4.2) than was used by the author to perform the IRT icing simulations in this research. In order to have a flight baseline set of ice shapes consistent with the ice shapes that would be produced for the IRT simulations, the author generated a new set of baseline ice shapes using the latest version of LEWICE3D. This new set of baseline ice shapes, called the revised IFB, ensures that no differences in IRT and baseline ice shapes are due to changes in LEWICE3D trajectory or icing physics models. All IFB ice shapes shown in this thesis are taken from the revised IFB.
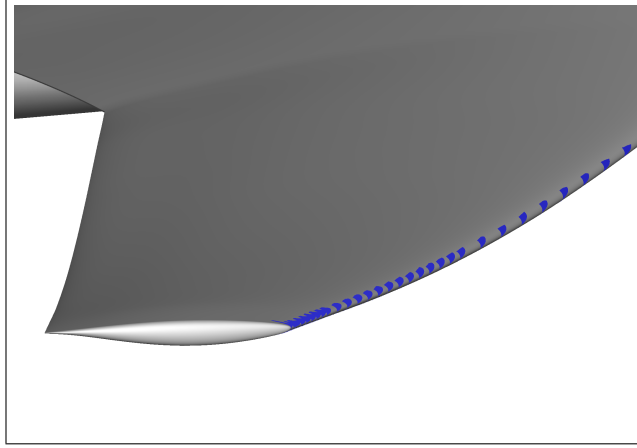
Figure 2.1: Ice Shapes on the CRM65 Wing for Case WB33 at $T = -4°C$ [26]

The conditions of Table A.1 represent both glaze and rime icing conditions. Rime ice is formed when supercooled water droplets from the air impinge on an object and freeze immediately, giving a freezing fraction of unity. Rime icing conditions are characterized by temperatures much below freezing ($T << 0°C$). In these conditions, the heat transfer coefficient, h_c, is not important to the ice shape because the droplets freeze on impact. Glaze ice is formed when temperatures are near freezing ($T \sim 0°C$). Due to the warmer temperatures, droplets do not freeze on impact resulting in a freezing fraction of $n < 1$. Because impinging droplets do not freeze on impact, they form a water film on the surface and run back away from the stagnation or attachment line until they either freeze or blow off the surface. Rime ice shapes tend to conform to the shape of the leading edge while glaze ice shapes often form horns in regions of the leading edge where the heat transfer is higher such as the suction peak. Conditions between glaze and rime icing conditions are called mixed icing conditions. Because glaze icing conditions result in thicker ice shapes, often with long horns, these conditions are good for ice shape comparisons because differences in ice shape are more apparent. The IFB critical icing scenarios include glaze, mixed, and rime icing conditions due to the temperature ranges over which they span. Figure 2.2 compares ice shapes at the midspan station of the CRM65 wing from the IFB for Case WB33.

Each of the IFB ice shapes in Figure 2.2 was generated using the same CFB flow solution. The temperature of the flow was changed during the LEWICE3D icing simulations to vary the icing conditions from glaze to rime. The temperature in turn affects the liquid water content, LWC, or mass of supercooled liquid water in a given volume of air. The shape with the longest horn is formed at $T = -4°C$. Because the temperature is near freezing, not all of the impinging droplets freeze on impact. Instead, a water film layer forms and the water runs away from the attachment line location (shown as a black dot in Figure 2.2). On the lower surface, a thin layer of ice is formed by the water running back from the leading edge. The heat

13
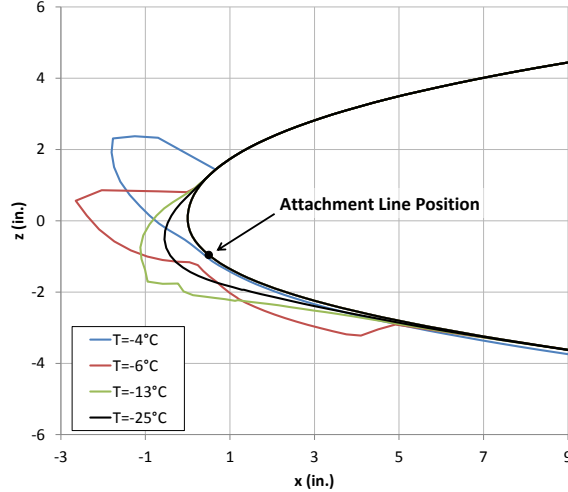
Figure 2.2: IFB Ice Shapes for Case WB33 with T Ranging from Glaze to Rime Icing Conditions

transfer coefficient is low enough that much of the water runs back until it blows off of the wing. On the upper surface, a maximum in the heat transfer coefficient occurs near the suction peak due to the high air velocity in that region. This area of high heat transfer causes the water film to freeze and build up in a horn ice shape. At the lower temperature of $T = -6°$C, the upper and lower horn ice begins to move toward the attachment line position due to the water film freezing more rapidly. As the temperature is cooled further the ice becomes more conformal to the wing geometry because droplets begin to freeze on impact, forming a rime ice shape at $T = -25°$C.

Swept-wing ice in glaze conditions often forms shapes called scallops. These highly 3D shapes which are also called "lobster tails" are similar to a 2D horn ice shape but with varied horn length with span. These features can develop to varying degrees and the icing physics that drives their formation is not well understood. For that reason, current 3D computational icing tools do not attempt to model spanwise variation in ice horns but instead simulate 2D ice shapes at select spanwise stations. In fact, scalloped ice shapes are sometimes formed during icing tunnel tests that are unexpectedly large because smaller ice shapes were predicted numerically, causing problems for IPS certification [31]. Figure 2.3 illustrates glaze ice shapes on a swept wing with complete scallops, incomplete scallops, and no scallops.

The CFB and IFB together set the baseline conditions at which, where possible, the simulations in this research were conducted. Due to limitations of the IRT such as maximum test section velocity at a given blockage level and the inability to control pressure, some conditions could not always me matched. The CFB and IFB conditions will be collectively referred to as the flight baseline conditions throughout this thesis.

(a) Complete Scallops   (b) Incomplete Scallops   (c) No Scallops
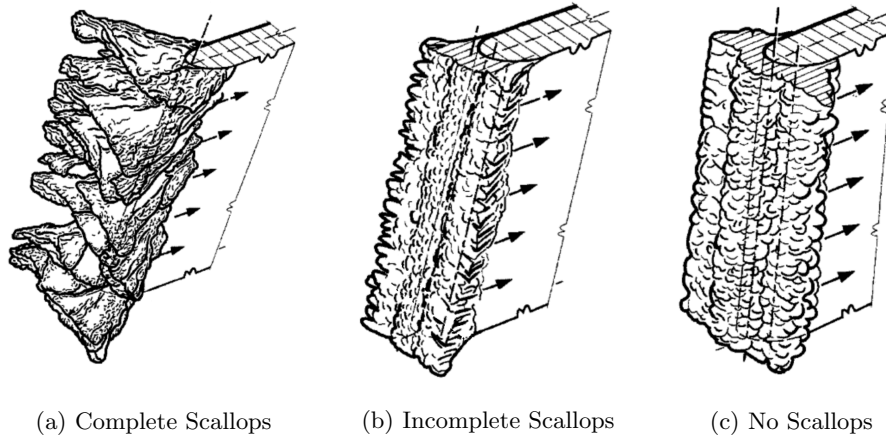
Figure 2.3: Glaze Ice Accretions on a Swept Wing, Adapted From Vargas [32]

2.1.4 Spanwise Station Selection

A hybrid-wing model is designed to represent either a single section or short spanwise region on the full-scale wing. The purpose of the model is to validate 3D model design, validate IRT test methods, and to create ice shapes in the IRT for a matrix of icing conditions that will later be extrapolated into artificial ice shapes that span the full wing for scaled aerodynamic tests. It was determined that three sections would be chosen from the CRM65 wing to be modeled. This number of models represents a good balance of trying to capture the ice across the full wing while limiting the cost and risk associated with designing extra stations and fabricating more test articles. It was important that the stations be placed in spanwise positions such that the full wing was best represented by just three discrete sections along the semispan.

In order to determine which three spanwise positions would best represent the entire wing, the team relied on the CFB and IFB analyses. Station positions of 20%, 64%, and 83% semispan were selected by comparing sectional aerodynamic characteristics and ice shapes across the span. The station at $\eta = 0.20$ is known as the inboard (IB) station. The IB station was selected to represent the wing inside the yehudi break and near the aircraft body. The large size of the wing near the root makes this station the most challenging as a more aggressive shortening of the full-scale airfoil is necessary to reduce the model size to fit inside the IRT. The Scale Factor (SF) of a hybrid airfoil design represents the factor by which the full-scale chord is shortened for the hybrid model and is defined as the full-scale chord divided by the total chord of the hybrid and flap (if present). Though the IB has the largest SF of the three models, it remains substantially larger than the models for the other two stations due to the size of the wing near the root.

The station at $\eta = 0.83$ is known as the outboard (OB) station. The OB station was selected to represent the wing near the wing tip where flow is expected to be more 3D. The precise location was selected

for convenience in that it is the junction between the inner and outer slats on the CRM65 wing. Because the inner slat is typically heated on commercial aircraft and the outer is not, a model at this position is valuable for anti-ice experiments and unheated ice shape verification.

The station at $\eta = 0.64$ is referred to as the midspan (MS) station and is the station which the model used in this thesis was designed to represent in the IRT. The MS station was selected based on the trend in ice horn angle across the span of the wing. The horn angle is defined as the angle that a line drawn from the center of the leading edge cylinder to the tip of the horn makes with the chord line. Ice horn angle has been shown to have important effects on the aerodynamic characteristics of wings [2]. Plotting the upper horn angle with semispan on the IFB for icing conditions which produce horn shapes showed that horn angles tend to increase with semispan nearly linearly up to about $\eta = 64\%$ where they then decrease to the tip. This trend is illustrated in Figure 2.4 where the upper horn angle is plotted for two of the icing cases used in this thesis. Figure 2.4a shows the horn angle, θ, plotted from the aircraft side-of-body to the wing tip for case WB33 at a temperature of $T = -4°C$. A trendline passing through the three stations at $\eta = 0.20$, 0.64, and 0.83 is included. A similar plot for case WB71 at $T = -6°C$ is shown in Figure 2.4b.

(a) Case WB33 T-4 Horn Angle   (b) Case WB71 T-6 Horn Angle
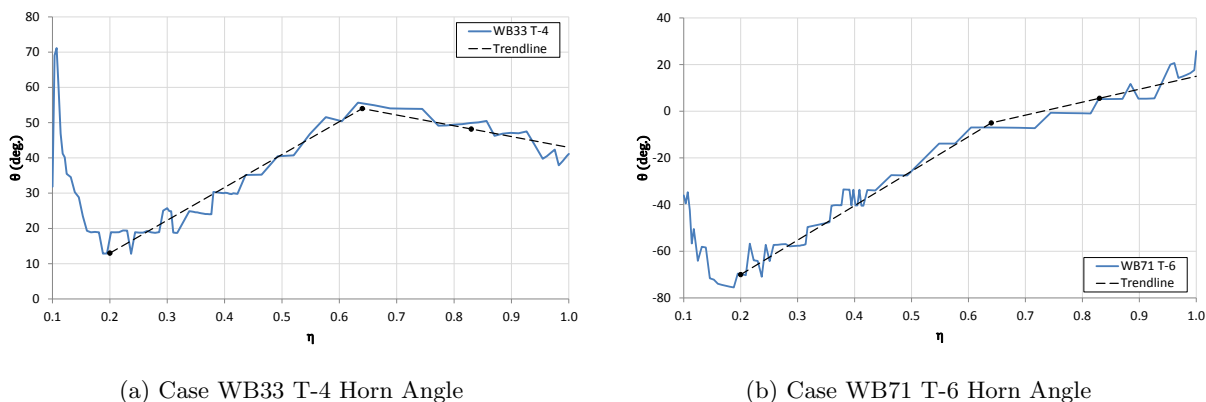
Figure 2.4: Upper Horn Angle with Semispan Location on the IFB for Two Icing Cases

The MS station was selected by the author for the current work for several reasons. First, the MS station is located past the yehudi break in a region of the wing where the flow is similar to that of an infinite, swept wing, making the assumptions of simple sweep theory more applicable (see Section 2.2.2). This is important because the 3D wing model begins as a 2D airfoil design as detailed in Section 2.2. Second, the local chord in the normal direction is of sufficient length to require a hybrid model with $SF = 2$. This SF is larger than that of the OB station ($SF = 1.5$) making it a more challenging design yet the literature shows that hybrid airfoils perform well with SF as high as 2.

2.2 Flapped-Hybrid Model Design

The 3D hybrid model design begins with an airfoil that is designed in 2D using methods that are well documented in the literature [9–12]. The conditions for which these airfoils are designed come from the matrix of icing conditions presented in Table A.1 transformed into 2D using simple sweep theory. The 2D model is validated against the CFB and IFB using CFD tools, in which process a 2D aerodynamic calibration is produced. Finally, the airfoil is extruded into a 3D wing model.

2.2.1 Hybrid Airfoils

Reduced-chord airfoils with a full-scale leading edge and redesigned aft section, called hybrids, can be used to produce ice shapes that agree well with those from the full-scale while dramatically reducing blockage and overall model size [8, 12]. Fujiwara et al. [13] showed that a hybrid has the additional benefit of producing comparable ice shapes at a lower C_l than would be required by a full-scale section. These truncated model characteristics allow model designers to work within limited budgets and current icing wind tunnel constraints including physical tunnel size, turntable and balance load limits, and blockage limits.

In order to produce accurate ice shapes the flowfield and heat transfer characteristics around the leading-edge portion of the hybrid model must match that of the full-scale airfoil. While these could only be matched perfectly by using the full-scale airfoil itself, it has been shown that satisfactory agreement in ice shape can be produced when certain flow characteristics are well matched. Matching the pressure distribution on the leading edge section is an effective way of creating similar flowfields in the region of interest, producing comparable droplet impingement and heat transfer characteristics. Two features of the pressure distribution are of particular importance for 2D ice shapes, the location of the stagnation point or maximum pressure and the location and magnitude of the suction peak or minimum pressure. Fujiwara et al. [13] showed that for airfoils the stagnation point location has a first-order influence on the ice shape, making it the primary indicator of flowfield similarity in the leading-edge icing region. The suction peak also has an important, though somewhat less pronounced, impact on the ice shape that forms on the leading edge of the hybrid airfoil. The location of the suction peak is primarily controlled by the stagnation point location so that when stagnation point is matched well the location of the minimum pressure is also. However, the magnitude of the suction peak may still be quite different from that of the full-scale airfoil when stagnation points are matched. This contributes to a mismatch in the heat transfer coefficient on the upper surface near the leading edge. For glaze icing conditions, the local heat transfer coefficient, h_c, determines whether impinging droplets freeze or run back. Thus, it follows that differing suction peak magnitudes can result in

17

different ice shapes. Fujiwara et al. [13] highlighted the importance of the stagnation point location and the suction peak magnitude and outlined the hybrid design method used to create the 2D design for this work.

Similar results for 3D swept-wing hybrid models have yet to be produced. The design and simulation of the 3D hybrid models for this project thus necessitated the assumption that similar trends would hold true. That is, it was assumed that to first order, good ice shape agreement would be achieved by matching the attachment line location on the model in the region of interest to that of the full-scale wing. It was also desirable to match the suction peak magnitude when possible. These assumptions allowed the team to begin assessing the quality of model designs early and make changes where needed. To show that these assumptions hold true for the MS model is one of the objectives of this thesis.

A hybrid-model design is characterized by several important parameters. As mentioned previously, the SF is the full-scale airfoil chord divided by the total hybrid-model chord and represents the factor by which the baseline geometry is shortened. The upper and lower leading-edge extents are the chordwise length of the full-scale leading edge that is kept from the baseline airfoil, given as a percent of the full-scale chord length. The nose droop angle, γ, is the angle that the hybrid model chord line makes with the full-scale chord line. This can be viewed as representing the elevation of the hybrid trailing edge with respect to the full-scale chord line. Alternatively, it can be viewed as changing the camber of the hybrid airfoil. A more positive nose droop angle causes a lower trailing edge elevation or more camber, shifting more load to the aft of the hybrid. The quarter-chord zero-lift pitching moment coefficient, C_{m0}, affects the camber line curvature of the aft hybrid section such that a more positive C_{m0} will result in a less cambered aft section and, therefore, reduced aft loading. Values of γ can be both negative and positive but C_{m0} is usually negative. Because ice shapes grown on the nose of the hybrid model are compared to the full-scale baseline airfoil, the hybrid angle of attack is measured relative to the full-scale chord line rather than the hybrid chord line. If present, the deflection of the flap may be measured relative to the full-scale chord or other reference. For the current research, the flap angle is measured relative to the horizontal when the hybrid airfoil is rotated such that the full-scale chord is at the local angle of attack corresponding to that station on the CRM65 wing. For the IB, MS, and OB stations that local twist angle is 9.25, -1.05, and -2.21 deg. in the normal direction, respectively. Figure 2.5 illustrates some of the design parameters of hybrid airfoils with the nose from the full-scale airfoil shown bolded. The model shown has $\gamma = 7$ deg., $C_{m0} = -0.32$, $SF = 2$, and upper and lower leading-edge extents at 5% and 10% of c_{fs}, respectively. Note that this combination of values for nose droop and zero-lift pitching moment is more extreme than would be seen on a typical hybrid design in order to illustrate their effects more clearly. The large positive γ brings the tail of the hybrid airfoil well below the

full-scale chord line, giving the appearance of a drooping nose if the hybrid and full-scale chords are aligned. The negative C_{m0} causes a high degree of aft camber, seen in the curvature near the trailing edge.
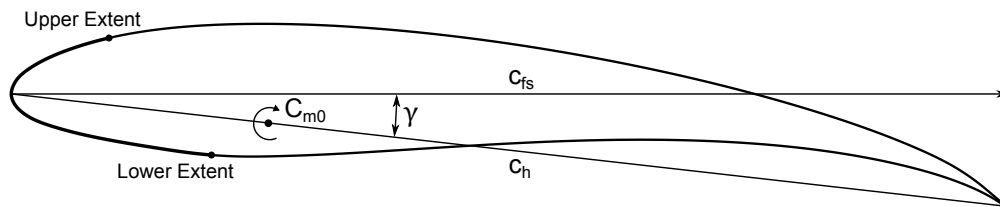
Figure 2.5: Important Parameters of a Typical Hybrid Airfoil

The 2D hybrid model design process is largely automated using several existing codes. It begins by determining the pressure distribution on the full-scale airfoil using XFOIL [33,34]. Next, droplet trajectories are computed using AIRDROP [35] which results in an impingement efficiency distribution, β, for the full-scale airfoil. The impingement efficiency is the vertical distance over which a set of droplets are dispersed in the freestream divided by the arc length over which the same droplets impinge on the airfoil surface. It gives a nondimensional measure of the mass that impinges at each point on the surface of the geometry. The user then determines how much of the full-scale leading edge will be retained on the hybrid model. It is common to set the leading edge extents past the impingement limits on both the upper and lower surface. However, Fujiwara et al. [13] showed that, employing careful engineering judgment, the designer may reduce the leading-edge extents once the resulting ice shapes are well established. The user also chooses a value for SF, γ, and C_{m0} after which PROFOIL [36] is used to design the aft section of the hybrid using an inverse airfoil design method, reducing the airfoil's size as compared to the full-scale reference. XFOIL and AIRDROP are again used to determine the C_p and β distributions on the hybrid design. The last step in a single-element hybrid design is to check for satisfactory matching of the hybrid C_p and β distributions to those of the full-scale baseline found previously. The user can then adjust SF, γ, C_{m0}, and/or the leading edge extents and iterate on the design, if desired. A flowchart of the entire hybrid design process is given in Figure 2.6.

After a hybrid model is designed for a specific set of conditions, it may be effectively used at other conditions by adding a flap. This allows the flowfield to be modified by altering the stagnation point or attachment line on the leading edge of the model by driving changes in circulation with flap deflection. There are tradeoffs for having a flap. The flap adds length to the total chord of the hybrid design requiring that the main element have a more aggressive design for the same total SF and leading edge extents. This causes
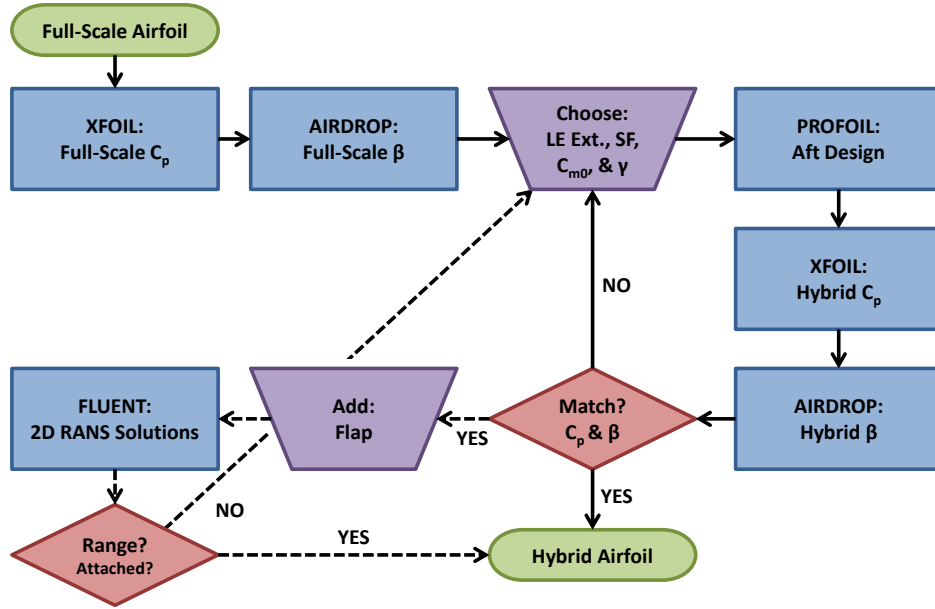
Figure 2.6: Hybrid Airfoil Design Flow Chart

more curvature at the upper and lower leading-edge extents of the model which increases the likelihood of separation due to adverse pressure gradients. However, an external flap can reduce separation near the trailing edge of the main element due to the favorable flow characteristics of the slot. If a flap will be needed on a hybrid model, it should be included in the hybrid design as early as possible. Because the hybrid design process uses inviscid tools, it is also important to check the flapped-hybrid design for separation and other viscous effects using a Navier-Stokes based solver. For the design of the MS model it was necessary to add a flap to the main element of the hybrid so that the model could be used for the full set of critical icing conditions. After adding a simple external flap, 2D RANS flow solutions were generated for the flapped-hybrid model at the desired conditions to verify that the corresponding stagnation point locations could be reached while avoiding flow separation. Some of these simulations are discussed in Section 2.2.3. The optional flap addition and RANS flow verification steps are included in Figure 2.6.

2.2.2 Simple Sweep Theory

Matching the flowfield of a 3D wing using a 2D airfoil simulation is impossible due to 3D effects. However, a reasonable approximation can be obtained by applying simple sweep theory which shows that a 2D cut from a swept 3D wing taken in the direction normal to the leading edge can approximate the flow around that section in 3D if the 2D simulation uses the component of the freestream velocity normal to the leading edge.

Simple sweep theory is based on a swept wing of infinite span and is also known as infinite yawed wing theory for obvious reasons. As the name suggests, the theory involves several simplifying assumptions. The first is that the cross section of the wing is constant with span implying no taper or twist. Also, the sweep, Λ, is measured in the plane containing the freestream velocity vector, $\vec{V}_\infty$, rather than in the traditional chord plane. This assumption is reasonable for small angles of attack. Finally, the theory assumes inviscid flow satisfying the Euler equations. Though none of these assumptions are met by the complex wing geometries on modern commercial transport aircraft, the theory provides a reasonable approximation. This approximation allows 3D swept wings to be modeled using 2D flow tools. Performing initial design iterations in 2D and then validating and refining those designs in 3D saves time and allows a broader initial exploration of the design space. The equations relating normal and streamwise geometric parameters and aerodynamic coefficients are easily obtained from the geometry of a swept wing and those important to the current work are presented here:

$$\alpha_{3D} = \alpha_{2D} cos\Lambda_{le} \tag{2.1}$$

$$c_{3D} = \frac{c_{2D}}{cos\Lambda_{le}} \tag{2.2}$$

$$C_{P_{3D}} = C_{P_{2D}} cos^2\Lambda_{le} \tag{2.3}$$

$$C_{l_{3D}} = C_{l_{2D}} cos^2\Lambda_{le} \tag{2.4}$$

Note that the sweep angle is presented here with a subscript denoting the leading edge. Because sweep theory is derived around the assumption of a constant-chord wing, this subscript would generally not be necessary. However, the distinction that the sweep used within this work is relative to the leading edge is worth emphasizing because these relations will be applied to the tapered wing of the CRM65. McLean [37] discusses simple sweep theory in more detail in addition to elaborating on some of the general characteristics of finite, swept wings in viscous flows. The derivation of these and other simple sweep theory equations not important for the current work are given in his text, *Understanding Aerodynamics* [37].

Because the impingement efficiency distribution is important to the shape of ice that accretes on an airfoil or wing, it was also necessary to relate the β distribution of a normal cut to that of the streamwise cut of the wing. As a relationship for doing this was unknown to the author, one was derived using the definition of impingement efficiency. The complete derivation is presented in Appendix B with the following result:

$$\beta_{3D} = \beta_{2D} \left(\frac{\Delta y_0}{\Delta y} \right) cos\Lambda_{le} \tag{2.5}$$

where Δy_0 and Δy are initial and surface spacing of the impinging droplets in the y direction, respectively. If it is assumed that the droplets do not spread appreciably in the spanwise direction then $\Delta y_0 / \Delta y \approx 1$ and Equation (2.5) simplifies to

$$\beta_{3D} = \beta_{2D} cos \Lambda_{le} \tag{2.6}$$

Equations (2.1)-(2.6) were used in several important ways. First, they allowed informed design of the IRT hybrid models in 2D, enabling a more thorough exploration of the design space before 3D models were created. Second, these equations were used to compare 2D aerodynamic and icing results from the initial 2D hybrid design to those of the CFB and IFB. It is often convenient to refer to analyses conducted in 2D as being in the "normal direction" meaning in the 2D plane normal to the leading edge of the swept wing. Similarly, the "streamwise direction" implies 3D parameters taken in the plane parallel to the freestream flow over a wing or 3D hybrid model.

2.2.3 Wing Model Design

The MS model design began with the 2D design method described in Section 2.2.1. The main element was designed so that a flap would be necessary to add the circulation strength needed to eventually reach all the stagnation points required by the CFB solutions. This results in the flap and main element sharing the loading needed to match the flow in the nose region. It was determined that a flap optimization was beyond the scope of the current work. Therefore, a flap was created using a NACA 6412 airfoil scaled to 1/3 the hybrid main element chord or 1/4 the total of the hybrid main element and flap chords ($c_{h+f} = c_{fs}/SF$). A constant gap and overlap value of 1.5% the total model chord, c_{h+f}, was used so that the flap on the 3D test article would require no translation, reducing complexity and fabrication costs. To avoid variation in gap and overlap for different flap deflections, the NACA 6412 profile was modified to have a constant radius of curvature at the leading edge, the flap pivot point being set at the center of this radius. Upper and lower leading-edge extents are at $x/c_{fs} = 10\%$ with a zero lift pitching moment coefficient of $C_{m0} = -0.05$ and a nose droop angle of $\gamma = -5.5$ deg. The MS airfoil and flap coordinates normalized by chord are given in Appendix C along with the flap pivot location. Note that these are given at a body angle of attack of $\alpha_b = 0$ deg. and a flap deflection of $\delta = 0$ deg. Figure 2.7 shows the final MS 2D flapped-hybrid design with coordinates normalized by full-scale chord, $c_{fs} = 122.72$ in. (3.12 m). It is important to remember that in the context of a hybrid-wing design, these 2D reference and design parameters used for the initial hybrid-airfoil design are taken in the normal direction.

22
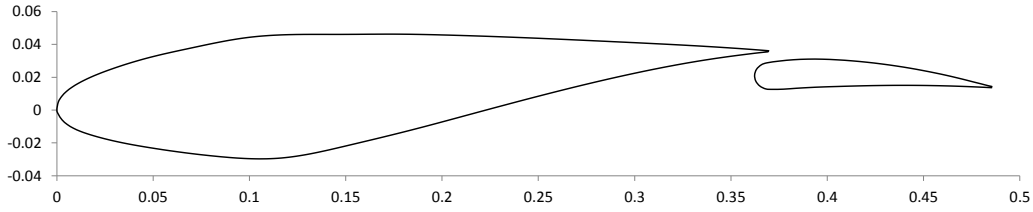
Figure 2.7: Final Midspan Station Flapped-Hybrid Airfoil

As mentioned, 2D RANS simulations of the flapped-hybrid airfoil were performed using the methods of Section 2.3. The flapped hybrid was modeled in the IRT test section with the walls present using a standard set of test section conditions where $V_\perp = 77.2$ m/s, $P = 94.7$ kPa, and $\rho = 1.285$ kg/m^3. The turbulence parameters at the inlet were determined using the method discussed in Section 2.3.4 resulting in a turbulent kinetic energy of $k = 1.08$ m^2/s^2 and specific turbulence dissipation rate of $\omega = 47.34$ s^{-1}. This corresponds to a streamwise test section velocity of 188 knots (96.9 m/s), which is typical in the IRT. The simulation was repeated at various angles of attack for a set of fixed flap deflections. This produced the aerodynamic calibration (aerocal) plot of Figure 2.8.
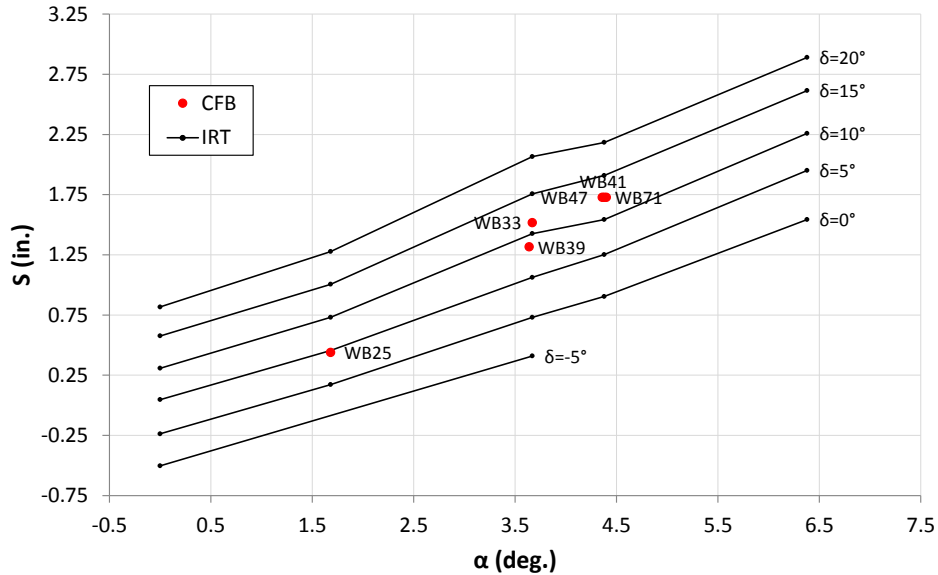
Figure 2.8: Midspan Station 2D Aerodynamic Calibration Plot

The aerocal gives the arc length, s, of the stagnation point location measured from the model hilite, or point with minimum x value, at a CRM65 body fixed reference frame angle of attack of $\alpha_b = 0$ deg.

23

versus the model angle of attack, α, at several flap deflections, δ. Note that s and α are transformed into the streamwise direction because the aerocal is used in 3D comparisons. The attachment line locations for the six critical icing scenarios from the MS station of the CFB are also shown. The aerocal serves two purposes. First, it shows that the flapped-hybrid design is effective in reaching all the stagnation point locations required for the IFB test cases. Second, it serves as a tool for predicting what flap deflections will be required by the 3D model to match attachment line locations at the centerline of the IRT to those of the CFB. When data points from 3D IRT simulations are later included, it also shows trends between the 2D and 3D IRT simulations.

The airfoil design is performed with the full-scale leading-edge chord line at the true local angle of attack at which it rests on the CRM65 wing. It is left at this angle during extrusion so that the 3D model produced is at an angle of attack of zero in the CRM65 body fixed reference frame. The model can then be rotated to an angle of attack consistent with the respective test case in the IRT. This means that if the droplets in the IRT are assumed to travel parallel to the tunnel walls, the test article will be impinged by droplets at the same global angle of incidence as the full-scale wing in flight. The flap is deflected about an axis which is parallel to the trailing edge of the main element so that gap and overlap remain constant for all positive flap deflections in the range needed.

While for the testing of anti-ice systems it may be necessary to retain an actual 3D portion of the wing leading edge, the 3D models for this project are simple extrusions of the airfoil design that was discussed in Section 2.2.1. This means that the models only represent a planar cut of the full-scale wing rather than a spanwise section of the wing. The hybrid airfoil design was extruded along its normal. It was then rotated about the negative z-axis so that the leading edge was at the CRM65 leading-edge sweep angle $\Lambda_{le} = 37.15$ deg. This extrusion was performed with the model at $\alpha = 0$ deg. and the flap at $\delta = 0$ deg. The model was then trimmed so that it measured exactly 72 in. (1.83 m) in the spanwise direction, reaching from floor to ceiling in the IRT. The angle of attack of the model in the IRT is measured in the streamwise direction while the flap deflection angle is given in the normal direction because the hinge axis is along the swept trailing edge. Figure 2.9a shows an orthogonal view of the model in the IRT test section with flow from left to right. Figure 2.9b shows the MS model overlaid on the full-scale CRM65 wing at the $\eta = 64\%$ station. Note how the model chord in the normal direction is half that of the CRM65 when measured from the model centerline leading edge.

An important reference on the 3D model is the hilite. The hilite, often written highlight, is the curve which passes through the minimum x location on the leading edge of the model at each y position, taken in the IRT reference frame. Note that this choice of reference frame makes the hilite a function of angle of
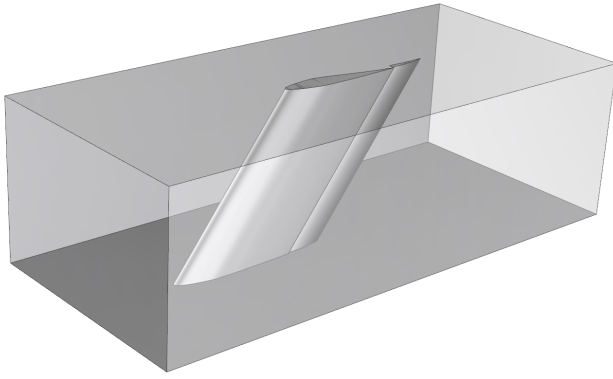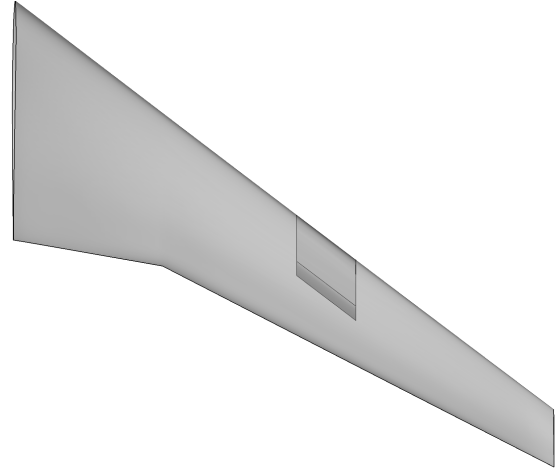
(a) Model in the IRT Test Section   (b) Model on the Full-Scale CRM65 Wing

Figure 2.9: Final Midspan Hybrid Model in the IRT Test Section and on the CRM65 Wing at the Midspan Station

attack. However, the hilite used in this research is defined with the model at $\alpha = 0$ deg. and is therefore unambiguous. Because the MS model has constant cross section with span, the hilite has a constant z value in both the model-fixed and IRT reference frames. All arc distances, s, are taken relative to the hilite point at a given spanwise station with positive values corresponding to the high-pressure surface of the model, unless stated otherwise.

Another important region on the model will be referred to as the region of interest. The region of interest is the portion of the leading edge geometry on which the ice accretions will be documented during IRT testing. For the MS model, this is defined as the section of the leading edge from $y = -6$ to $+6$ in. (-15.2 to $+15.2$ cm) in the spanwise direction from the upper leading-edge extent to the lower in the wrapwise direction, $y = 0$ being the centerline of the model and the IRT. The region of interest is illustrated in Figure 2.10. In general, the leading-edge geometry in this region on a hybrid model is either a 2D cut of the reference model extruded over 1 ft. (30.5 cm) span or a 3D 1 ft. span portion taken from the reference wing. Portions of the model inboard and outboard of the region of interest can be redesigned to improve the similarity between the flow within the region of interest and the flow in the same region on the full-scale wing. However, such a design would require a better understanding of what key flow characteristics should be matched in this region and would add a great deal more complexity to the design of a swept-wing, hybrid model.
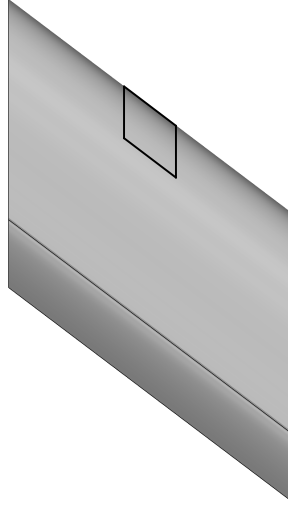
Figure 2.10: Midspan Hybrid Model Region of Interest

2.3 3D Meshing and Flow Solutions

In order to model droplet impingement and ice accretion in LEWICE3D, a flow solution containing a velocity field, static pressure, and static temperature is required. The team at UIUC chose to use ANSYS® Fluent v14.5 for the required 2D and 3D CFD simulations due to their familiarity with the program. The software POINTWISE® was used to create the meshes for these simulations.

2.3.1 IRT Mesh Topology

The IRT test section is 20 ft. (6.10 m) in length with a cross section that is 6 ft. (1.83 m) tall and 9 ft. (2.74 m) wide. The center of the floor mounted turntable is 106.5 in. (2.71 m) from the inlet of the test section. Because the hybrid model is mounted from floor to ceiling, the model span is 72 in. (1.83 m), as described in Section 2.2.3. A tunnel fixed reference frame was used with positive x-axis in the flow direction and positive y-axis pointing toward the ceiling of the tunnel. The origin of this axis system is centered in the IRT test section in the yz-plane with $x = 0$ at the center of the turntable. This results in the root of the model placed at the floor of the IRT being at $y = -36$ in. (91.4 cm), the tip and ceiling at $y = +36$ in., and the walls of the test section at $z = \pm 54$ in. (137.2 cm). A schematic of the current IRT configuration is shown in Figure 2.11.

The 3D mesh used for the tunnel was based on the 2D meshes that were used to validate the hybrid airfoil and flap designs. These 2D meshes were validated prior to their use and a grid resolution study was performed as described in Sections 2.2.1 and 2.3.3. The same meshing topology was then used to perform the flapped-hybrid RANS validation described in Section 2.2.1 and used to create the aerocal plot in Figure 2.8.
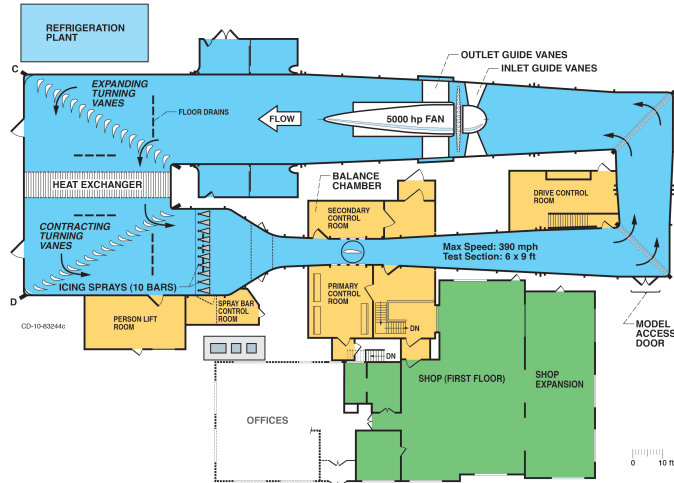
Figure 2.11: Current NASA Glenn IRT Configuration

The 3D mesh consists of a constant cross section representing the IRT test section which is extended an additional 20 ft. (6.10 m) upstream and downstream so that the total mesh length is 60 ft. (18.29 m). The extensions were added to move the inlet and outlet boundaries a sufficient distance from the wing model. The surface grids on the main element and flap of the model were first created using a rectangular structured domain wrapped from upper trailing edge to lower trailing edge with a smaller rectangular domain on the blunt surface of the model trailing edges. An average surface spacing of 1/4 in. (6.35 mm) was used with points clustered near the leading and trailing edges of the main element and flap. These structured domains were then diagonalized to create a highly ordered, unstructured mesh composed of triangular cells. This technique allows higher quality interpolated gridpoint values to be extracted from the flow solution at the model surface while still allowing an entirely unstructured mesh topology.

The tunnel walls used an average gridpoint spacing of 3 in. (7.6 cm) in the flow direction. The domains representing the IRT inlet, outlet, and vertical walls were composed of fully-unstructured triangular cells. The floor and ceiling domains were also fully-unstructured, but the solver in POINTWISE was used to force a higher cell count where the floor and ceiling meet the model root and tip, respectively.

Several meshes were made to model the flow using an inviscid, Euler solver in which case the domains were combined into an unstructured block that was then populated with isotropic tetrahedra. These simple meshes contained a node count of around 5 million gridpoints. However, a Navier-Stokes solution was required to capture separation and other viscous effects in the flow for use in LEWICE3D. Therefore, it was necessary to create an enhanced mesh on viscous surfaces to properly resolve the boundary layer. For meshes that would be used in the RANS solver, anisotropic triangles and tetrahedra were grown on the walls and model surface as described in the following section.

27

2.3.2 Anisotropic Tetrahedral Meshing

The POINTWISE [38] software package features an unstructured solver that uses anisotropic tetrahedra to grow high aspect ratio cells off surfaces on which it is desired to resolve a boundary layer. Anisotropic tetrahedral meshing (T-Rex for short [39]) allows high resolution boundary layer grid cells to transition smoothly into standard, isotropic tetrahedral meshes away from walls. The T-Rex solver also works on 2D domains where anisotropic triangles are grown off of curves and edges as shown in Figure 2.12 on the upper, midchord surface of a hybrid airfoil. The solver uses the grid spacing along the surface and a user-specified initial offset distance to create either pairs of triangles which mimic rectangles in 2D or triads of tetrahedra which mimic triangular prisms in 3D to grow a single layer of cells. Additional layers are then grown with an offset distance which is the product of a growth factor and the offset of the previous layer. When the triangles or tetrahedra in the boundary layer mesh are of the same order of magnitude in volume as the free triangles or tetrahedra far from the walls, the T-Rex solver transitions to regular isotropic cells to populate the remaining volume of the block. This creates a seamless transition in grid spacing and a smooth transition in cell volume between the anisotropic and isotropic triangle/tetrahedra meshes. The outermost T-Rex layer shown in Figure 2.12 terminates in this manner near the center of the image.
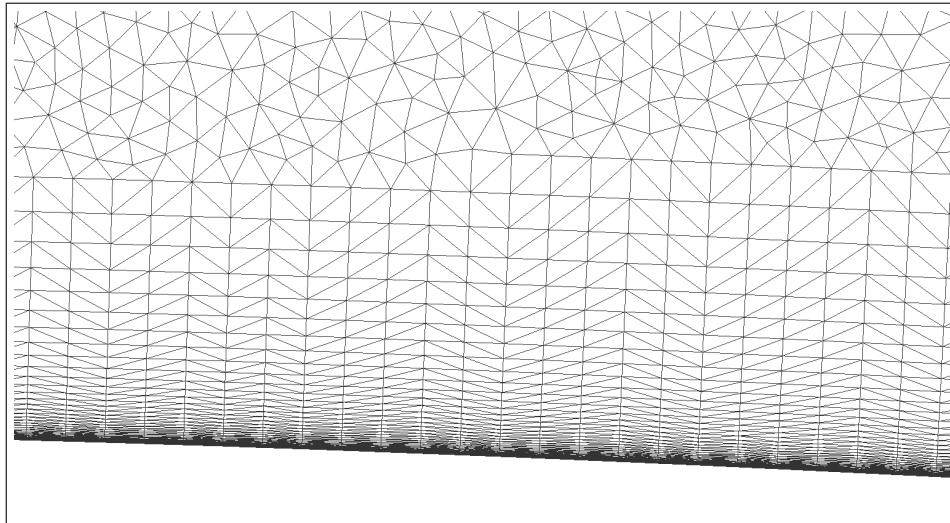
Figure 2.12: 2D Anisotropic Triangular Mesh

Figure 2.13 shows the junction between the 3D flapped-hybrid model and the IRT ceiling with a crinkle cut of the T-Rex volume mesh. On the left side of the image the surface domain of the ceiling is seen with highly unordered triangles typical of a fully-unstructured, isotropic triangle mesh. The lower portion of the image is the low-pressure surface of the main element. The aligned triangles which conform to a rectangular
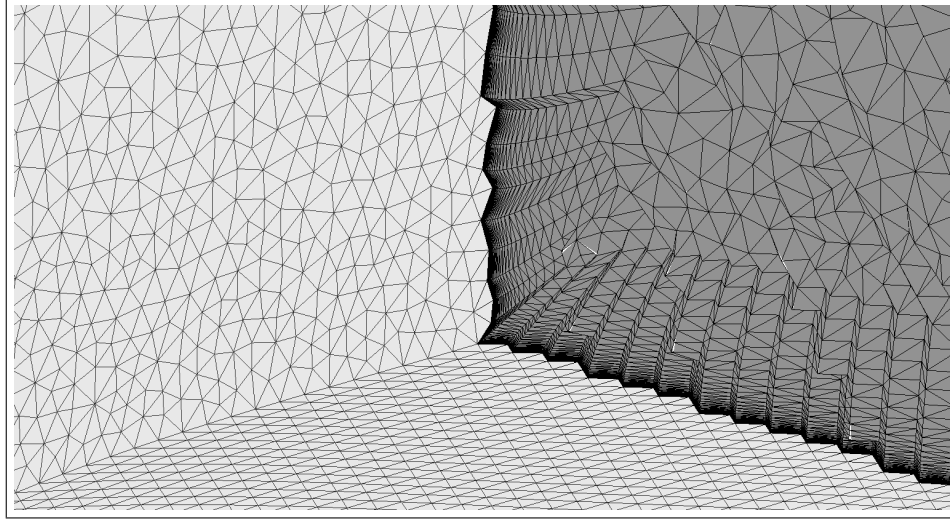
Figure 2.13: 3D Anisotropic Tetrahedral Mesh

topology are the result of the diagonalized structured surface domain described in Section 2.3.1. A cut of the T-Rex layers grown off the two surfaces is shown on the right. The increasing thickness of the layers along with the changing aspect ratio of the cells is clearly observed. As described previously, the T-Rex layers are seen to terminate when the volume of the cells are of the same order as the isotropic tetrahedra of the bulk volume mesh (shown in the upper right corner). The anisotropic tetrahedra in the T-Rex boundary-layer mesh can be recombined into prism layers during export of the mesh. This option can improve convergence characteristics when used with certain CFD software packages such as Fluent. Steinbrenner details the T-Rex extrusion algorithm and provides examples of its use [39].

The T-Rex solver in POINTWISE was selected for the current work due to the quality of unstructured meshes it is capable of producing on curved 3D geometries. The use of fully-unstructured meshes greatly reduces the time required to create a 3D mesh and creates greater flexibility in the physical geometry of the IRT models. T-Rex boundary layer meshes were grown on all viscous surfaces of the IRT meshes. This is done by first creating unstructured domains on all the boundaries of the mesh as described in Section 2.3.1. Before the 3D T-Rex solver can be used, any 2D domains that "cut" the volume in which a boundary layer mesh is desired must have a 2D T-Rex mesh generated. To this end, the T-Rex solver was used first on the inlet and outlet domains of the IRT mesh. A block was then created, enclosed by the inlet, outlet, walls, and hybrid model surfaces. Finally, the T-Rex solver was used on this block to generate anisotropic tetrahedra of sufficient resolution to resolve the boundary layers that form on the IRT walls and model surface. The initial thickness of the boundary layer mesh was set to achieve a y^+ value near unity based on the IRT test conditions. The option to recombine tetrahedra was toggled on during mesh export, resulting in conversion

of the tetrahedra in the T-Rex mesh into prism layers. The resulting baseline IRT mesh shown in Figure 2.14 contained approximately 17 million gridpoints for the MS model. The test section inlet is on the left with flow up and to the right (in the direction of the positive x-axis).
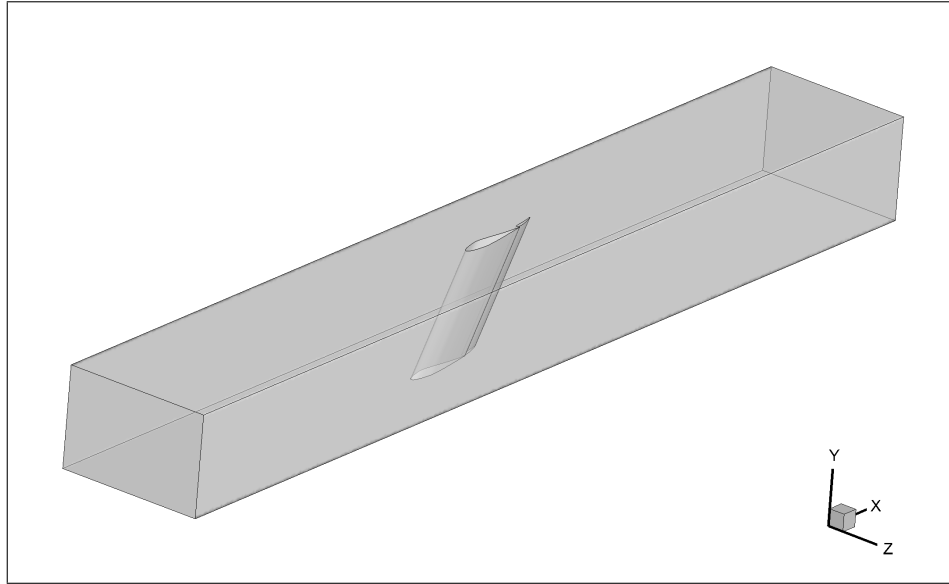
Figure 2.14: Baseline IRT Mesh Layout

2.3.3   Mesh Validation

The general mesh topology that would eventually be used for the 3D IRT flowfield calculations was validated extensively in 2D first. Because the hybrids were designed with an external flap, the author searched for an experiment with pressure data where a simple airfoil section was used in a two-element configuration. Such a test was performed by Wenzinger in the NACA 7 ft. by 10 ft. (2.13 m by 3.05 m) tunnel [40]. A flapped-model geometry consisting of a NACA 23012 main element with 20% scale NACA 23012 flap was simulated using a 20 in. (50.8 cm) chord straight wing with end plates. This model was run in the tunnel with a test section velocity of 80 mph (35.8 m/s), dynamic pressure of 16.37 $lb_f/ft.^2$ (784 Pa), and an average test Reynolds number of 1.46 million. Pressure data was taken at the tunnel centerline on both elements for an array of angles of attack and flap deflections. The author simulated two of these cases in the tunnel section using 2D CFD to validate the meshing topology described in Sections 2.3.1 and 2.3.2. The main element and flap were positioned based on the turntable and flap pivot positions described in the report. Inlet k and ω values were estimated using the specified tunnel turbulence intensity and an approximate turbulence length scale.

The first case simulated was for $\alpha = 2.32$ deg. and $\delta = 0$ deg. Because Fluent performs flow solutions dimensionally, inlet density and pressure were set such that the dynamic pressure and Reynolds number matched those given in the report. A comparison of the resulting pressure distribution is given in Figure 2.15. The pressure coefficient on the main element agreed well with the experimental data reported by Wenzinger [40], with a slight difference near the suction peak. A second case at an angle of attack and flap deflection closer to what was expected for the flapped-hybrid model was simulated for $\alpha = 2.82$ deg. and $\delta = 20$ deg. Figure 2.16 shows the resulting pressure distribution. Again, the C_p distribution on the main element is well matched with an improved match on the flap as well.

(a) Main Element   (b) Flap
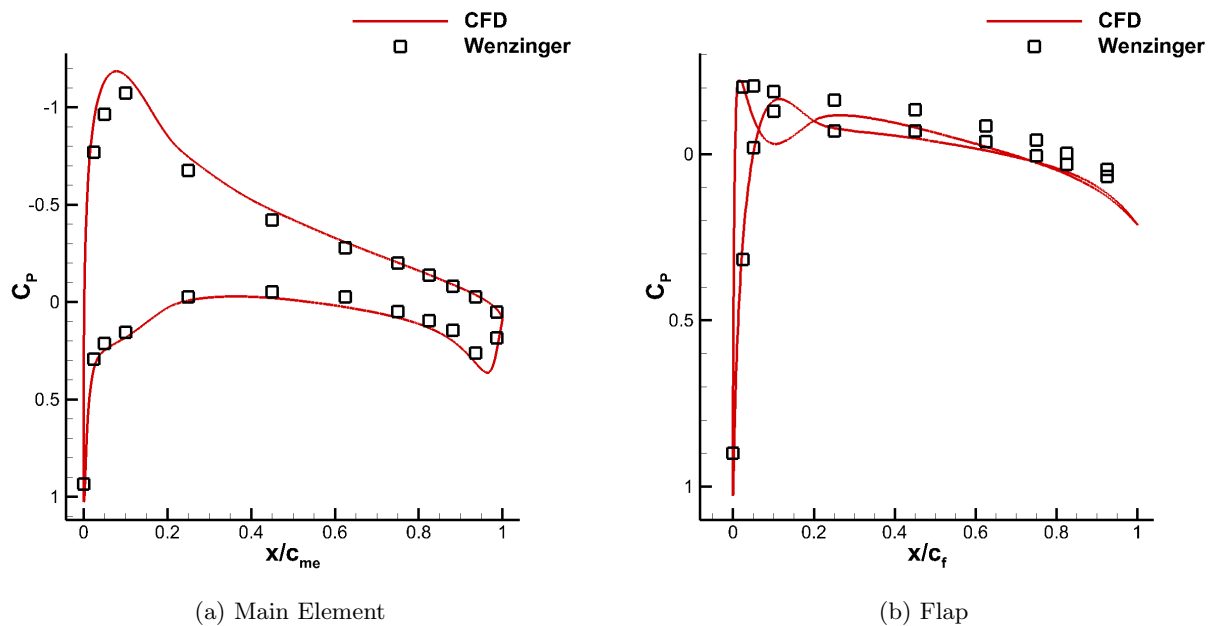
Figure 2.15: C_p Distribution for $\alpha = 2.32$ deg. and $\delta = 0$ deg. on the NACA 0012 Two-Element Model

After the use of fully-unstructured meshes with T-Rex boundary layer grids was validated on the two-element NACA 23012 configuration, a 2D grid resolution study was performed on the MS station flapped-hybrid design to estimate what mesh node count would be necessary for the 3D IRT meshes. The node count was approximately doubled until a sufficiently small change in the solution resulted. The lowest node count which gave satisfactory agreement with that of twice its size was adopted as the baseline. Simple sweep theory was used to scale the geometry and run conditions to the normal flow direction to make these 2D simulations representative of the 3D runs that would follow. The offset distance for surface mesh nodes was set to achieve a $y^+ \approx 1$ for all critical icing scenario conditions.

(a) Main Element   (b) Flap
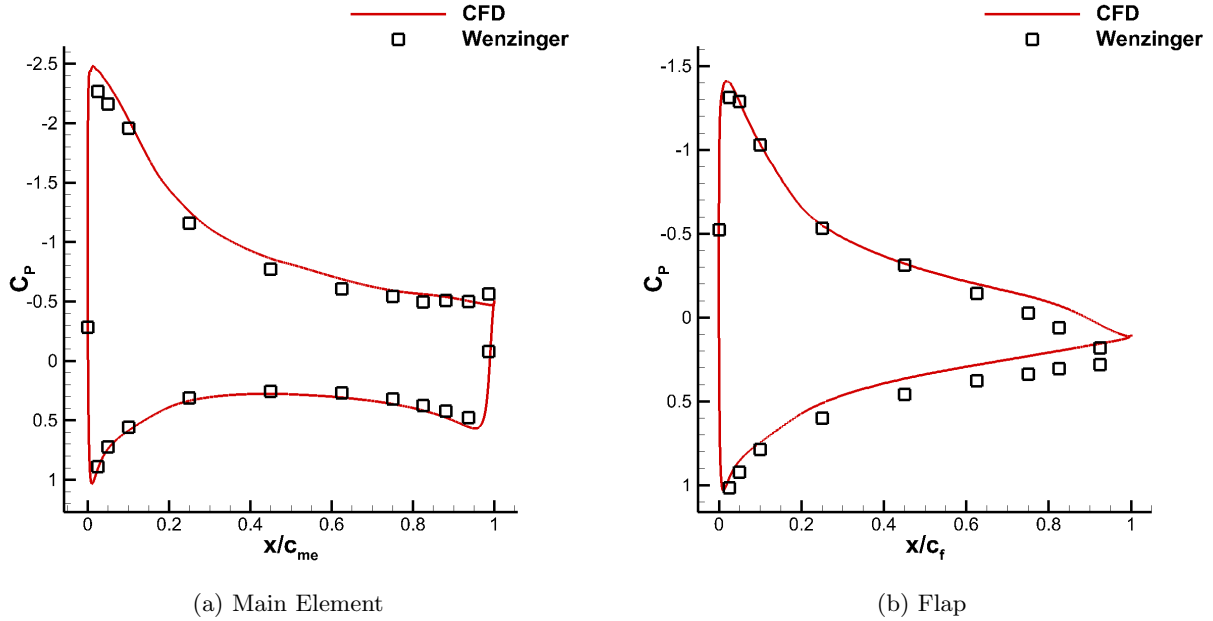
Figure 2.16: C_p Distribution for $\alpha = 2.82$ deg. and $\delta = 20$ deg. on the NACA 0012 Two-Element Model

2.3.4 Flow Solutions

The flow simulations performed in Fluent were done using the Menter Shear Stress Transport (SST) k-ω turbulence model. The upstream boundary condition of the test section mesh was set to a uniform flow velocity inlet. The velocity used at the inlet was the desired test section velocity for the respective test condition. Inlet values for the turbulence parameters k and ω were determined using the results of an empty IRT flow simulation performed by Clark et al. [41] in which a 3D RANS analysis was used to estimate the flow in the new 2012 configuration of the IRT. Clark et al. simulated the IRT from the exit of the heat exchanger to the turntable including the turning vanes, spray bars, contraction nozzle, and test section. These results were produced using Fluent configured in a similar manner to the current work.

In order to perform flow approximations at velocities other than what were used by Clark et al. [41], k and ω were scaled using the relations

$$k = k_0 \frac{V^2}{V_0^2} \tag{2.7}$$

$$\omega = \omega_0 \frac{V}{V_0} \tag{2.8}$$

where V_0, k_0, and ω_0 are the tunnel velocity, turbulent kinetic energy, and specific turbulence dissipation rate produced by Clark et al. [41], respectively.

The pressure outlet boundary condition was used at the test section downstream boundary. The wall and surface boundary conditions were set to solid, viscous surfaces with the no-slip condition enforced for viscous simulations. A summary of the test section flow conditions is presented in Table 2.3 where Re_c is based on the total MS streamwise model chord, $c_{sw,h+f} = c_{\perp,fs}/(SF\cos\Lambda_{le}) = 76.98$ in. (1.96 m). The energy equation was toggled on in order to determine the static temperature in the flowfield.

Table 2.3: IRT Simulation Conditions

	WB33 T-4	WB47 T-6	WB71 T-6
V (m/s)	119.41	128.61	104.51
P (Pa)	90,011	88,658	91,882
T (K)	269.15	267.15	267.15
ρ (kg/m^3)	1.1653	1.15632	1.1984
μ (Pa·s)	1.6998E-05	1.6914E-05	1.6914E-05
k (m^2/s^2)	2.58	3.00	1.98
ω (s^{-1})	73.22	78.87	64.09
M	0.363	0.393	0.319
Re_c	16.0E+06	17.2E+06	14.5E+06

In order to produce flow solutions in the IRT similar to those of the CFB and for use in icing simulations, the 3D IRT flow solutions were performed with angle of attack equal to that of the case to be matched at various flap deflections. Initial flap deflections were chosen based on the 2D aerocal. As discussed in Section 2.2, it was assumed that the ice shapes would best match when the attachment line location of the model matched that of the full-scale wing. Therefore, the attachment line location at the tunnel centerline was compared to that of the baseline wing. The flap setting was then adjusted and the flow solution repeated until a satisfactory match in attachment line location at IRT centerline was achieved. This process was repeated for Cases WB33 T-4, WB47 T-6, and WB71 T-6 to produce the flow solutions that were later used for the LEWICE3D icing simulations. Table 2.4 shows the α and δ values which resulted in the closest agreement in attachment line position at IRT centerline along with the associated values of wrap distance.

The resolution of the structured mesh near the hilite and attachment line locations on the CRM65 grid used to generate the CFB is approximately 0.15 in. (3.81 mm). The wrapwise grid spacing on the surface mesh for the IRT models was set to 0.05 in. (1.27 mm) in the region near the leading edge containing the attachment line. Thus, the error in attachment line location at tunnel centerline in the last column of Table 2.4 is to within the limits of the meshes used and is considered an acceptable deviation. Because even

Table 2.4: Angle of Attack and Flap Deflection Required for Cases of Interest

Case	α (deg.)	δ (deg.)	s_{IRT} (in.)	s_{CFB} (in.)	diff. (in.)
WB33 T-4	3.67	15	1.486	1.517	-0.031
WB33 T-4	5.50	5	1.536	1.517	$+0.018$
WB47 T-6	4.36	16	1.732	1.727	$+0.005$
WB71 T-6	4.40	15	1.732	1.727	$+0.005$

the actual test articles will have a pressure port spacing of approximately 1/4 in. (6.35 mm), it is unlikely the true attachment line location during testing will ever be known to this level of fidelity.

For Case WB33, a second set of α and δ is shown. After it was known that a flap deflection of $\delta = 15$ deg. was needed to match attachment line locations for Case WB33, a flap deflection of $\delta = 5$ deg. was set and the angle of attack was adjusted until the attachment line location matched at the IRT centerline. This simulates a scenario in which the flap has lost effectiveness due to separation. By lowering the flap deflection the loading on the flap can be reduced and then the angle of attack of the model can be increased so that the main element carries a larger load. Such a need could also arise if a model without a flap is to be used at an off-design condition. Running a model at an angle of attack other than that of the wing it represents is generally viewed as a less representative way to reach the attachment line location because it changes the global angle of incidence at which droplets approach the model from far upstream. It is also not well established whether this difference in angle of attack between the model in the tunnel and the wing in flight causes other differences in the 3D flowfield that adversely affect ice shape similarity. This flow solution was produced so that it could be determined if this is an acceptable method for controlling ice shape. The attachment line positions for this case are included in Table 2.4. Inviscid solutions were performed at the flight angle of attack and flap deflections which matched attachment lines for these test cases to investigate what flow features could be attributed to viscous effects.

2.4   3D Icing Simulations

Several computational tools were used for calculating droplet trajectories, estimating the corresponding impingement efficiency, and predicting ice shapes on the hybrid airfoils and wing models for this project. Several of these tools were introduced in Section 2.2.1 where they were discussed in the context of 2D hybrid airfoil design. The 2D ice accretion program LEWICE was among these as it was used in the design and validation of initial hybrid airfoils. The 3D IRT flowfield solutions generated by Fluent were used to calculate water droplet trajectories and ice accretions on the 3D IRT models using a 3D grid based ice accretion

program similar to LEWICE called LEWICE3D. A parallel version of LEWICE3D, called TRAJMC3D, was used on the UIUC supercomputer, Taub, to allow more computationally intensive exercises. An overview of these codes follows including a description of their use in this thesis.

2.4.1 LEWICE Overview

LEWICE is a 2D ice accretion program that is used to predict ice shapes on airfoils and other planar bodies. The user supplies atmospheric conditions such as velocity, pressure, and temperature and meteorological parameters such as *LWC*, *MVD*, droplet distribution, and relative humidity. LEWICE then predicts the growth of ice on a body over time using a four-step process.

1. An inviscid panel method solver is used to determine a flowfield on the initial geometry. For the first time step this geometry is the user input body profile know as the clean geometry. For subsequent time steps, it is the clean geometry plus ice that has been grown to that point in time.

2. Particle trajectories are calculated to establish impingement of droplets on the body, resulting in an impingement efficiency distribution on the body.

3. The surface roughness and heat transfer coefficient are estimated and used to perform a thermodynamic and ice growth calculation.

4. The geometry profile is modified to represent the growth of ice on the body. These updated body coordinates are then used as the input for the next flow solution and the process is repeated for the duration of the user-specified icing time.

The user has the option of supplying a flowfield solution if desired in which case the ice accretion process is limited to one time step.

Because LEWICE uses a computationally inexpensive panel method to update the flowfield, it is a very efficient tool in exploring a wide range of conditions and model designs very quickly. It is also well validated against experimental ice shapes produced both in flight and in the IRT [25, 42]. LEWICE 3.2.2 was used extensively in the early design of the hybrid airfoils. Though it is capable of calculating ice shapes for multi-element configurations, the program is not currently validated for these cases and the manual warns that nonphysical α and δ may be required to match ice shapes. Other limitations such as the added complexity of using user-specified viscous flow solutions restrict the use of LEWICE to the initial design phase. For the design of a 3D model it is more effective to begin 3D design and evaluation sooner rather than trying to improve the fidelity of 2D LEWICE simulations.

2.4.2 LEWICE3D Overview

As its name suggests, LEWICE3D [24] is an ice accretion program similar to LEWICE but for 3D bodies. It is used to numerically accrete ice on any 3D body for which a flow solution can be produced. Though not limited to aircraft, it is commonly used to analyze ice shapes on wings and other lifting surfaces, inlets and nacelles, nose cones, and other surfaces on aircraft bodies.

LEWICE3D simulates ice shapes on surfaces at user specified planar cuts known as sections. Though the process is considerably more complex, generating ice shapes on 3D bodies requires the same general steps as are required in 2D described in Section 2.4.1 with several major differences that will be pointed out. Whereas all four tasks in Section 2.4.1 are performed by LEWICE, the user must complete the first task below before running LEWICE3D.

1. A flowfield about the body of interest is needed to integrate the droplet trajectory paths from the initial icing cloud onto the model surfaces. Though LEWICE has the option of a user-specified flow solution, its internal panel method solver is most often used as it allows the flow solution to be updated at each time step, reflecting changes in the flow due to ice growth. LEWICE3D does not currently include an internal flow solver. The user must generate a high-quality 3D flow solution before the code can be used to generate ice shapes. LEWICE3D supports grid based flow solutions from any commercial package via the use of converter routines that are distributed with the code. The conversion codes transform flow solution outputs of various formats into a standard input format recognized by the LEWICE3D executable. In this sense the first step is actually comprised of two parts; i) generating a flow solution and ii) converting the flow solution into LEWICE3D input files.

2. LEWICE3D begins by integrating droplet trajectories through the flow solution to characterize impingement on the sections of interest. The user can control release points and other trajectory integration parameters by setting flags and variables in the fort.2 input file. The user has the option of determining droplet trajectories only passing near the sections of interest, in which case impingement efficiency is only determined in a thin region near these planar sections. Alternatively, the trajectories can be determined using the Monte Carlo method. This method will result in impingement efficiency being calculated continuously on a larger region specified by the user. The Monte Carlo method is recommended for flows with large circulation or highly 3D impingement limits. This method of calculating droplet trajectories requires considerably more computation time but requires less judgment and expertise on the part of the user.

3. The convective heat transfer coefficient is determined. While the option to determine the heat transfer coefficient directly from the temperature gradients in the flow solution exists, it is generally calculated using an integral boundary-layer method which uses the edge velocity to find the displacement thickness and momentum thickness. The heat transfer coefficient is affected by the roughness parameter. In LEWICE the roughness parameter is set using a correlation based on experimental data. Because the amount of data for 3D ice shapes is so limited, the user has generally been required to specify a roughness parameter in LEWICE3D, though the most current version does not require this. The Reynolds analogy is used to determine the heat transfer coefficient and a thermodynamic and ice accretion analysis is performed.

4. Ice is accreted on the surface at the section planes. Because it is impractical to update the flow solution after short time steps, LEWICE3D accretes the ice for the full exposure time instantaneously. This is significantly different from LEWICE where the flow solution is modified as ice accretes on the body.

The Monte Carlo droplet trajectory calculation method was used for this project because the thick, swept hybrid models cause considerable spanwise flow. This spanwise flow component drives highly 3D dispersion of impinging droplets because smaller droplets are carried along the span while larger droplets, due to their higher inertia, are not. The Monte Carlo method also allowed the impingement efficiency to be defined across the entire model span for comparison with the IFB, which used the same type of trajectory calculation. Because the Monte Carlo droplet trajectory calculation is computationally intensive, a parallel version of LEWICE3D called TRAJMC3D is available for use on cluster computers. TRAJMC3D v2.47 was used to perform the ice accretion analyses in this work and is thus implied anywhere LEWICE3D is mentioned. More details about LEWICE3D can be found in the user's manual [24].

2.4.3 Comparing LEWICE and LEWICE3D Simulations

It is clear from Sections 2.4.1 and 2.4.2 that several important differences exist between LEWICE and LEWICE3D. Some of these differences have a significant impact on the icing physics models in the codes. Noting such differences, one might expect the ice shapes that result from the two programs to be very different. However, comparing ice shapes on 2D hybrid airfoils which are intended to represent 3D full-scale wing sections allows design and validation work to be conducted in the relatively inexpensive 2D domain. Thus, it is helpful to consider the applications and limitations of such comparisons.

A study was performed to investigate how well 2D ice shapes generated by LEWICE for the early hybrid airfoil designs compared to the 3D IFB ice shapes generated in LEWICE3D. Simple sweep theory was applied

to transform 3D results into the common 2D reference frame. The MS model hybrid airfoil design without flap was run in LEWICE to produce ice shapes over a range of α. The conditions for the 2D simulations were consistent with those of the CFB and IFB except that the normal component of velocity was used. Automatic time stepping was used in LEWICE. The stagnation point location calculated by LEWICE was compared to the attachment line location at the midspan station of the CRM65 CFB to determine the α that resulted in the best agreement. The ice shapes were then compared at this location. As the 2D hybrid design matured and a flap was added, flap sweeps were also conducted to show that using flap deflections to alter the stagnation point location was an effective method for matching ice shapes, though the specific flap angle at which the stagnation point was matched cannot be determined using LEWICE as it has not been validated for geometries with multiple bodies. The effects of tunnel walls were not simulated using LEWICE. Angle of attack and flap angle sweeps were performed in batch using an interface to LEWICE written by the author in MATLAB® which ensured consistency between runs.

The IFB ice shapes produced by LEWICE3D did not need to be altered for comparison with the 2D shapes from LEWICE because the sections of interest defined by Boeing were contained by planes normal to the leading edge. The CFB pressure coefficient distribution was scaled to 2D using Equation (2.3). The IFB impingement efficiency distribution was scaled to 2D using Equation (2.6). A comparison of the ice shape, β distribution, C_p distribution, and h_c distribution for the main element of the MS hybrid airfoil over a range of α for the conditions of case WB33 T-4 are shown in Figure 2.17.

From the ice shape comparison of Figure 2.17a, it can be seen that the ice shape changes considerably with angle of attack and that a good ice agreement is reached at $\alpha_\perp = 12.5$ deg. Despite the assumptions made by sweep theory and the differences between LEWICE and LEWICE3D, the major features of the ice shape are captured. The $\alpha_\perp$ for which ice shape is best matched also shows the best agreement in β_{max}, as seen in Figure 2.17b. Note that the sign convention for the wrap distance is opposite what is used elsewhere in this thesis so that positive values correspond to the upper surface of the airfoil. At $\alpha_\perp = 12.5$ deg. the 2D β distribution matches that of the 3D IFB well except for the tail of the lower surface, which results in a thin layer of ice in the LEWICE ice shapes. Figure 2.17c highlights an important difference between LEWICE and LEWICE3D. Observe that the LEWICE3D h_c is at all points along the surface much larger than that of LEWICE, and yet the ice shapes agree well. This shows that the icing physics models employed by the two codes are different so that despite the large difference in h_c, both codes produce results which compare well to validation data and, it appears, with each other. Finally, the 2D C_p distribution corresponding to $\alpha_\perp = 12.5$ deg. matches best with that of the 3D CFB, shown in Figure 2.17d. This is illustrated more clearly by Figures 2.18a and 2.18b which show the suction peak and stagnation point, respectively.

(a) Ice Shapes

(b) β Distributions

(c) h_c Distributions

(d) C_p Distributions
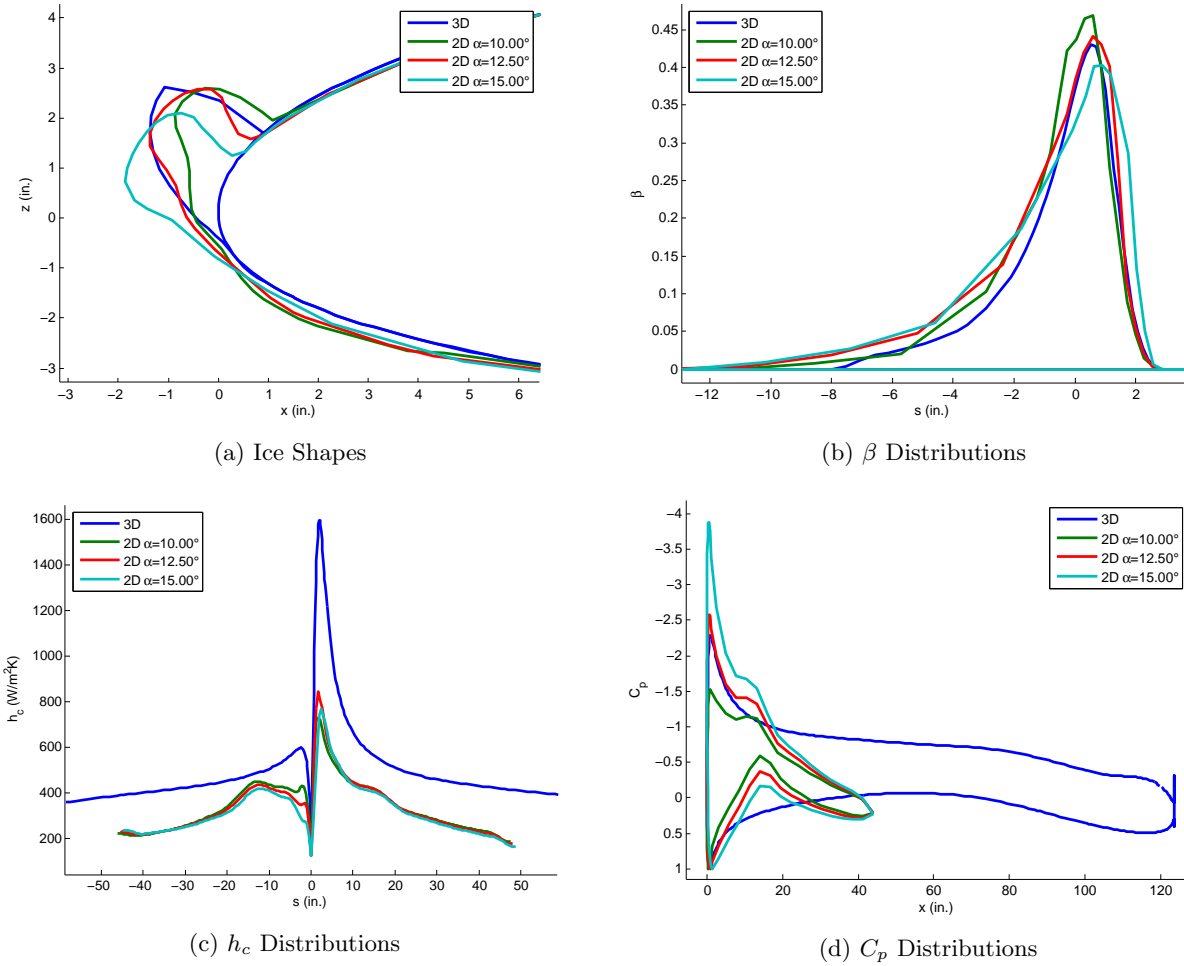
Figure 2.17: Comparison of LEWICE Results at Several Angles of Attack to Baseline LEWICE3D Results for Case WB33 T-4

At the level of zoom shown in Figure 2.18, the C_p values at the individual control points on the panels of the model surface are seen. LEWICE does not allow a substantial increase in resolution. To improve the resolution of the flow solution, include viscous effects, and give accurate results with a flap present, a RANS solution from an external solver could be used. However, this would decrease the economy of exploring designs in 2D and would still suffer from the limitations of using sweep theory to approximate 3D flow with 2D tools. Furthermore, because the stagnation point was shown by Gustavo et al. [13] to be the primary indicator of ice shape agreement on an airfoil, 2D RANS simulations can be conducted with tunnel walls and flaps present to show that the position of the stagnation point can be adjusted to cover the range desired without stalling. That the ice shapes will match when stagnation points are matched can be assumed, and the use of LEWICE avoided. Thus, once the 2D aerocal discussed in Section 2.2.3 was performed, further verification and design work for the MS model was done in 3D.

(a) Suction Peak

(b) Stagnation Point
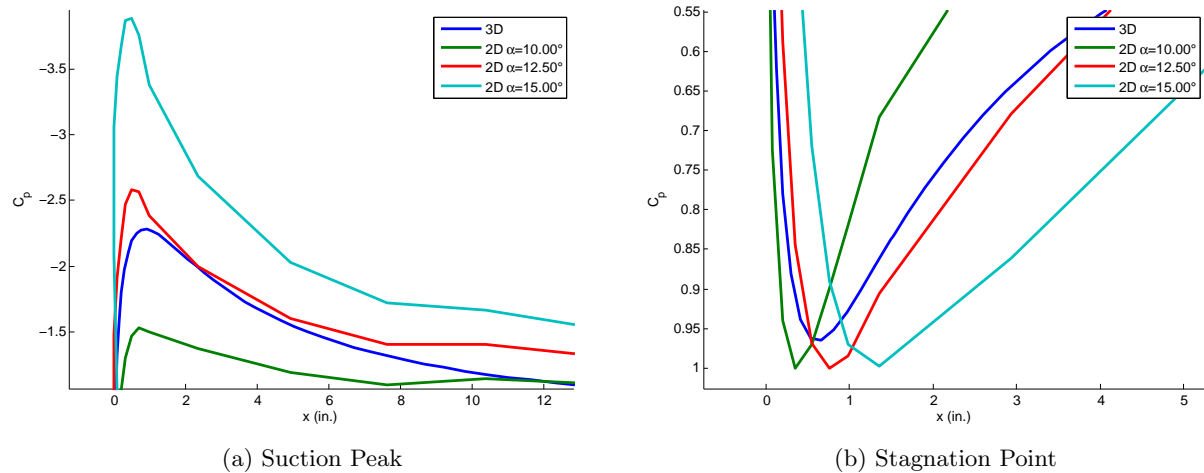
Figure 2.18: Comparison of LEWICE C_p Extrema at Several Angles of Attack to Baseline LEWICE3D Results for Case WB33 T-4

Comparing LEWICE and LEWICE3D ice shapes proved valuable throughout the 2D hybrid design process as it informed early decisions and allowed a more thorough exploration of model tradeoffs. Table 2.5 summarizes some of the differences between LEWICE and LEWICE3D that should be considered when comparing the resulting ice shapes.

Table 2.5: Differences Between LEWICE and LEWICE3D

	LEWICE	LEWICE3D
Time Steps	Automatic	1
Flow Solution	Internal	External
Flow Solver	Panel Method	Any
Viscosity Treatment	Inviscid	Either
Flow Update	Each Step	None
Roughness Parameter	Automatic	User Defined
$C_{p,max}$	1	$\cos^2 \Lambda$

2.4.4 Test Conditions

The test conditions used for the flowfield and icing simulations were taken from the Boeing test case conditions except for instances where the actual IRT conditions will not be able to match the CFB and IFB conditions. It was assumed that the IRT will be able to operate with test section velocity equal to the flight velocity for cases with $V < 250$ knots (128.6 m/s) which was assumed to be the maximum operational

velocity of the IRT due to the blockage of the large model. Because the test cases represent flight at a range of altitudes far greater than the elevation of the IRT which is not pressure controlled, the actual pressure and density differ considerably from the flight conditions. The static pressure in the IRT test section was determined from the stagnation pressure at the IRT facility which is known to be approximately $P_t = 14.3 \text{ lb}_f/\text{in.}^2$ (98.6 kPa) using the following isentropic relationship:

$$P = P_t \left[1 + \frac{\gamma_{air} - 1}{2} M^2 \right]^{\frac{\gamma_{air}}{1 - \gamma_{air}}} \tag{2.9}$$

where $\gamma_{air} = 1.4$ is the specific heat ratio of air and the Mach number is that of the flight case when tunnel velocity and temperature match flight. Otherwise, it is given by the usual $M = V/\sqrt{\gamma_{air} R T}$ with R being the ideal gas constant for air, about 287 J/kgK. The density was determined using the Ideal Gas Law.

Cases WB33 and WB71 at temperatures of $-4°C$ and $-6°C$, respectively, were selected as cases for the current work. Case WB33 has attachment line location, air speed, and angle of attack near the average of all the cases, making it a good candidate for general testing. Case WB71 has the largest flight angle of attack and an attachment line location which is farthest down the leading edge, requiring the most aggressive α and δ settings in the tunnel. The warmer temperatures for both cases produce glaze ice shapes with large upper horns that are sensitive to the local heat transfer coefficient, making it easier to determine when a good ice shape match is achieved. Case WB47 at $T = -6°C$ was also used in this research because the flight speed for this case exceeds the assumed IRT test section velocity limit of 250 knots (128.6 m/s). This provides an opportunity to investigate icing scaling methods where wind tunnel conditions are unable to match flight velocity.

The flow and icing conditions for the Case WB47 T-6 IRT simulations were adjusted to match several dimensionless parameters according to the method summarized by Tsao and Lee [43]. The method involves matching the modified inertia parameter, K_0, the accumulation parameter, A_c, and the stagnation plane freezing fraction, n_0. Tsao and Lee also recommend matching the Weber number, We_L, with characteristic length being the leading-edge diameter, d. This was not attempted because the leading edge of the model is fixed at full scale and the test section velocity is dictated by tunnel capability. The equations defining these parameters in terms of air and water properties and the test conditions are summarized in Appendix D. The interested reader can refer to Anderson's [7] work for a complete description of these formulations. Using the method outlined in Appendix D, MVD, LWC, and τ were adjusted until K_0, n_0, and A_c in the IRT matched the baseline values. Table 2.6 compares the conditions for the IRT simulations with those from the baseline analyses for the cases described above.

Table 2.6: Flowfield and Icing Condition Comparison for Several Cases

| | WB33 T-4 | | WB47 T-6 | | WB71 T-6 | |
	CFB/IFB	IRT	CFB/IFB	IRT	CFB/IFB	IRT
P (Pa)	69,702	90,011	57,209	88,658	95,956	91,882
ρ (kg/m^3)	0.9027	1.1653	0.7464	1.1563	1.2519	1.1984
Re_c	28.9M	16.0M	28.1M	17.2M	35.2M	14.5M
V (m/s)	119.41	119.41	139.60	128.61	104.51	104.51
T (K)	269.15	269.15	267.15	267.15	267.15	267.15
M	0.363	0.363	0.426	0.393	0.319	0.319
LWC (g/m^3)	0.551	0.551	0.509	0.467	0.509	0.509
MVD (μm)	20	20	20	22.88	20	20
Distribution	Lang. D	IRT*	Lang. D	IRT*	Lang. D	IRT*
τ (min.)	45	45	45	53.3	15	15
α (deg.)	3.67	3.67	4.36	4.36	4.40	4.40
δ (deg.)	NA	15	NA	16	NA	15

*The 10-bin measured IRT droplet distribution is given in Table 2.7.

The IFB icing simulations used a Langmuir D droplet distribution which has 7 bins and is considered representative of real droplet clouds [44]. The actual icing cloud created by the IRT spraybars differs slightly from the Langmuir D with somewhat longer tails and has changed with time. For IRT icing simulations, a 10-bin droplet distribution based on measurements taken by Papadakis et al. [45] in 2003 was used. These measurements were taken during impingement tests at the IRT using the Forward Scattering Spectrometer Probe and Optical Array Probe for $MVD = 20$ μm. Table 2.7 compares several droplet distributions normalized by MVD including the Langmuir D and the 10-bin measured IRT distributions. The Portion Liquid Water Content, $PLWC$, represents the portion of the total LWC belonging to each bin's droplet size.

Table 2.7: Nondimensional Langmuir D and Measured IRT Droplet Distributions

| | Langmuir D | | IRT 1989 | | IRT 2003 | |
Bin	$PLWC$	Diam.	$PLWC$	Diam.	$PLWC$	Diam.
1	0.05	0.31	0.05	0.3161	0.050	0.1925
2	0.10	0.52	0.10	0.4981	0.100	0.4695
3	0.20	0.71	0.20	0.6872	0.200	0.6901
4	0.30	1.00	0.30	1.0000	0.300	0.9804
5	0.20	1.37	0.20	1.3737	0.200	1.2741
6	0.10	1.74	0.10	1.9614	0.100	1.5367
7	0.05	2.22	0.05	2.8288	0.030	1.7599
8	-	-	-	-	0.010	1.9163
9	-	-	-	-	0.005	2.0334
10	-	-	-	-	0.005	2.2183

2.4.5 Description of Studies Performed

The flow solutions of the 3D flapped-hybrid model in the IRT discussed in Section 2.3 were generated with and without viscosity included. The inviscid solutions were used to establish the general trends of the flow over the MS model in the IRT test section. Viscous solutions were used as input flowfields along with the icing conditions of Table 2.6 to produce impingement and icing simulations using LEWICE3D. An overview of the studies which produced the results that will be discussed in Chapter 3 is given below:

Tunnel Sidewall Effects on a Swept-Wing Model

Inviscid simulations of the MS flapped-hybrid model in the IRT were investigated to consider how the presence of tunnel walls at the root and tip of a swept model affects the flow as compared to that of the reference station on a baseline, finite wing. Lifting-line theory was applied to the general case of a swept model bounded by sidewalls in an attempt to explain the observed results. Additional calculations were performed on finite, swept wings as well as a swept model with sidewalls using the vortex lattice method. The findings are discussed in Section 3.1.

Spanwise Load Control Techniques

Two methods for controlling the spanwise load distribution on a swept-wing model between sidewalls are considered using inviscid analysis. The effectiveness of the methods is discussed. These results are presented in Section 3.2.

Attachment Line Position

The importance of the attachment line position to ice shape on a swept-hybrid model is investigated using viscous flow analysis in Fluent and droplet trajectory and icing analysis in LEWICE3D in Section 3.3. The effect of attachment line is first considered in Section 3.3.1 using the flap angle to set several attachment line positions on the MS model with the conditions of Case WB33 T-4. For the same conditions, a change in angle of attack at a fixed flap angle is used to change the attachment line position with results presented in Section 3.3.2. Finally, the importance of the attachment line is demonstrated in Section 3.3.3 with a discussion of how LEWICE3D determines the attachment line using Case WB71 T-6.

Altitude Effects

LEWICE3D is again used on viscous flow solutions to investigate the effects of altitude on the ice shapes in the IRT using the conditions of Case WB33 T-4. Icing solutions produced at IRT pressure, density, and droplet distribution are compared to icing results which used the same IRT flow solution but with LEWICE3D conditions based on the pressure, density, and droplet distribution used for the

flight baseline. With the effects of altitude thus isolated, the impact on ice shape is discussed in Section 3.4.

Icing Scaling

An icing scaling method is used for Case WB47 T-6 to produce droplet trajectory, water catch, and freezing fraction similitude in the IRT, with geometric similitude assumed due to the full-scale leading edge on the hybrid wing model. The resulting IRT ice shapes are compared to the IFB for both the scaled and unscaled conditions in Section 3.5.

Spanwise Variation in Impingement and Ice Shape

Two viscous simulations for Case WB33 T-4 are revisited to consider the spanwise variation of the resulting ice shapes in Section 3.6. The benefits and limitations of using different α-δ pairs to generate the same centerline ice shape are considered.

Chapter 3

Results and Discussion

Understanding how the flow about the geometry of a 3D hybrid model in the tunnel will affect ice shape formation is important for model designers. To improve this understanding, the current research investigates, through computational methods, the major flow features inherent to a swept model in a tunnel and their resulting impact on ice cloud impingement and ice shapes. Inviscid flows are first considered so that general features of the IRT flow solutions can be identified. Then, RANS solutions and the corresponding ice shapes from LEWICE3D are considered.

Inviscid analysis is used in Section 3.1 to investigate the effects of the IRT floor and ceiling on the swept-wing model, generalized to any swept model between sidewalls. Techniques for controlling the effects of the sidewalls are investigated in Section 3.2, again using inviscid analysis. Section 3.3 makes use of viscous flow solutions to investigate how ice shape is affected by flap angle in Section 3.3.1 and angle of attack in Section 3.3.2. The effect on ice shapes due to the difference in altitude between the baseline and the IRT conditions is discussed in Section 3.4. The use of icing scaling to improve IRT ice shapes is considered in Section 3.5. Finally, the spanwise variation of ice shapes is discussed in Section 3.6.

3.1 Tunnel Sidewall Effects on a Swept-Wing Model

The IRT test section is oriented such that the root of the model is mounted to the turntable at the floor of the test section with the tip of the model pinned at the ceiling. The floor and ceiling of the IRT enforce a symmetry boundary condition on the flow about a model in the test section. For straight-wing models, this symmetry condition does not represent a large departure from the flow on a large aspect ratio, finite wing. However, for a swept-wing model it is expected that the flow will be considerably different due to the presence of walls which force 2D flow along the wall where the flow on the reference wing would otherwise be 3D at the corresponding spanwise position. If the boundaries at the floor and ceiling of the IRT are considered sidewalls, their effect can be generalized to any swept-wing model bounded by walls at the root and tip.

Figure 3.1 shows a pressure contour on the surface of the midspan (MS) model (described in Section 2.2.3) for the conditions of Case WB33 at $T = -4°C$ with $\alpha = 3.67$ deg. and $\delta = 15$ deg.

(a) Low Pressure Surface   (b) High Pressure Surface
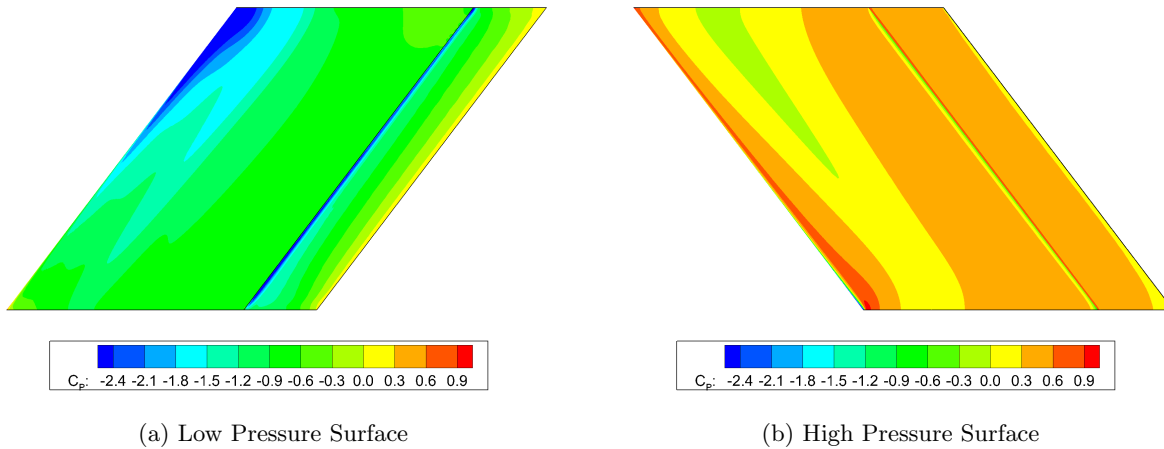
Figure 3.1: Inviscid C_P Contour on the MS Model for Case WB33 T-4 at $\alpha = 3.67$ deg. and $\delta = 15$ deg.

The model surfaces of Figure 3.1 are shown with flow from left to right. The low-pressure surface of the model in Figure 3.1a has pressure coefficient which decreases significantly with span near the leading edge. The C_P on the high-pressure surface, shown in Figure 3.1b, does not change nearly as much with span as it does on the low-pressure surface. Sectional C_P curves across the span are given in Figure 3.2, clearly showing that the suction peak increases drastically from the floor to the ceiling of the IRT. This decrease in pressure on the suction surface with span leads to an increase in the sectional lift coefficient, C_l, with span. For a fixed geometry, an increase in C_l results in a shift of the attachment line lower on the leading edge of the model. Ideally, the model would either have a constant attachment line with span matched to that of the reference wing at the station of interest or the attachment line on the model would have the same position across its span as the reference wing over the same span. Therefore, it is worth considering possible methods for adjusting the spanwise load distribution. In order to propose possible methods of spanwise load control, a fundamental understanding of why the C_P changes so drastically with span is necessary. By applying lifting-line theory to a swept model between sidewalls, the problem can be understood at a more fundamental level.

The application of lifting-line theory to a swept-wing model between sidewalls is illustrated in Figure 3.3. The model is shown in the center between two walls represented by dashed lines. The effects of the sidewalls are illustrated by placing images of the model to either side, mirrored over the wall boundaries. It should be understood that these images continue to infinity in either direction but those beyond which are shown
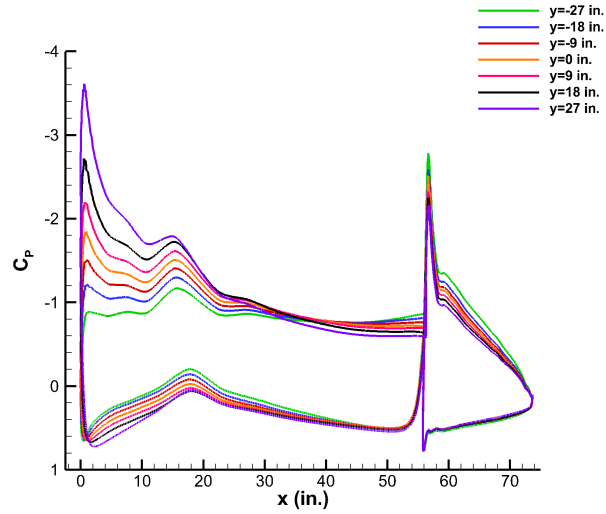
Figure 3.2: C_P Distribution Across the MS Model Span for Case WB33 T-4 at $\alpha = 3.67$ deg. and $\delta = 15$ deg.

have a diminishing effect on the actual model and are omitted for simplicity. Horseshoe vortices are placed along the model span with the bound segment on the lifting line of the model and the semi-infinite trailing segments aligned with the shed vortex sheet. Arrows on each vortex segment indicate the sign of the vorticity according to the right-handed convention. Image vortices are placed on the model reflections in a similar fashion. For simplicity, three stations are shown ordered alphabetically from the inboard to the outboard portion of the model.
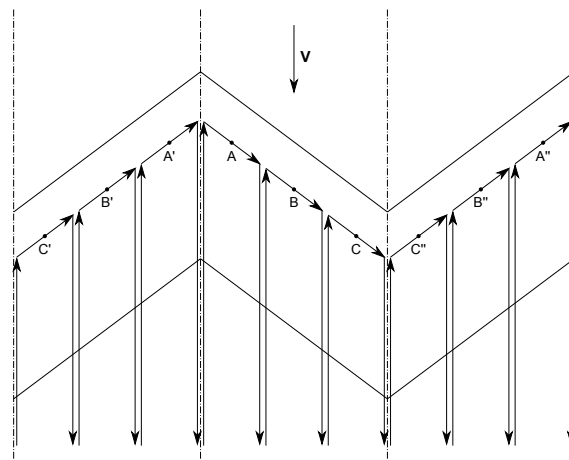
Figure 3.3: Lifting-Line Theory Applied to a Swept Wing Model With Sidewalls

The circulation at any point on the lifting line causes an induced tangential velocity component in the plane normal to the vortex. For a swept wing, this plane is not aligned with the freestream and therefore the circulation at a given station induces an upwash upstream of the leading edge at stations farther outboard. The strength of this induced upwash diminishes with the inverse of the distance from its source point on the lifting line. Considering this effect in the presence of tunnel sidewalls (or floor and ceiling when a wing is mounted vertically, as in the IRT) can illustrate why the inviscid spanwise load increase is so pronounced for the 3D hybrid model. Consider the plan view of the swept model of Figure 3.3. Recall that the walls themselves represent a symmetry boundary normal to which there can be no flow but along which, in the inviscid case, flow is unimpeded. These symmetry boundaries are then readily replaced by an image of the model and its associated vorticity. The inboard, midspan, and outboard stations of the model are labeled A, B, and C, respectively. The image of the model reflected over the inboard boundary has stations denoted by the same letters with a single prime superscript. Likewise, the image of the model reflected over the outboard symmetry boundary is labeled with double prime superscripts. Note the change in the direction of vorticity on the image vortices as compared to those of the actual model.

A vertical (out of the page in Figure 3.3) velocity at points upstream of the leading edge at station B is induced by the circulation about the lifting line at station A. This vertical velocity or upwash causes an effectively higher angle of attack resulting in a higher sectional lift at station B due to the circulation at station A. More generally, each station on a swept wing is exposed to an upwash induced by stations farther inboard and induces an upwash upstream of stations which are farther outboard. On an infinite, swept wing this essentially results in a uniform upwash at all stations because each has neighbors extending to infinity in either spanwise direction. However, for a model between sidewalls, the situation is quite different. Because station A' is oriented such that it induces upwash ahead of station B', station A does not receive the effective increase in angle of attack due to upwash that would be seen on an infinite, swept wing. Nonetheless, station A induces an upwash ahead of station B, increasing the effective angle of attack and thus the circulation at station B. Likewise, the circulation at station B induces an upwash ahead of station C. However, the circulation at station C" also induces an upwash at station C, further increasing the effective angle of attack and circulation at station C. This results in the trend that the sectional lift distribution increases across the span, with an amplification near the downstream wall.

To investigate this effect further, the vortex lattice method was applied using XFLR5. Three cases were run at an angle of attack of $\alpha = 5$ deg. First, a backward-swept wing with constant chord and no twist was simulated. The semispan, normalized by chord, was set to a value of 10 which is approximately the semispan of the CRM measured in MS hybrid-model chord lengths. A sweep of $\Lambda = 37.15$ deg. was used

48

with $V = 120$ m/s, $\rho = 1.225$ kg/m^3, and $\nu = 1.5 \times 10^{-5}$ m^2/s. Figure 3.4 shows the resulting sectional lift coefficient distribution beside a schematic of the wing with symmetry boundary at $y/c = 0$ and tip at $y/c = 10$.
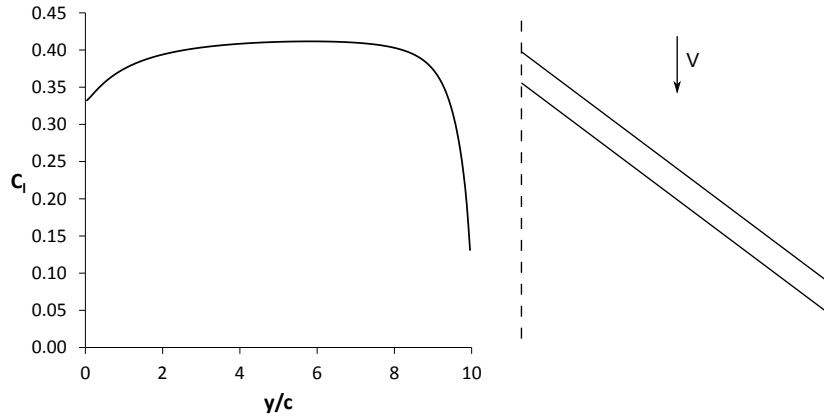
Figure 3.4: Lift Distribution on a Finite, Backward-Swept Wing Predicted by the Vortex Lattice Method

Near the midspan of the wing, the lift distribution is nearly constant, similar to what would be found on an infinite, swept wing. Closer to the symmetry boundary, however, the loading begins to drop off due to the lack of upwash that would be contributed if the wing continued farther inboard. The slope of the lift distribution curve is especially steep in the first chord length of the span where the somewhat accumulative effect of increasing spanwise load is acting to asymptotically bring the lift to a steady level. This is similar to the C_l on a typical swept-wing transport aircraft near the fuselage. The loading near $y/c = 10$ drops off sharply to zero as would be expected at the wing tip.

A second simulation was performed on the forward-swept wing of Figure 3.5. The dimensions of the wing and conditions of the simulation are the same as for the backward-swept wing. The symmetry boundary was simply moved to the other side of the model at $y/c = 10$, and the former symmetry plane became a wing tip at $y/c = 0$. The resulting sectional lift distribution again drops off rapidly near the tip ($y/c = 0$) and approaches a near constant trend at the midspan where the flow is similar to that of an infinite, swept wing. It is worth noting that the C_l in the midspan region is roughly 0.40, similar to the first simulation in the same area. The loading trend in the region near the symmetry boundary is exactly as predicted, rising sharply due to the additional upwash and, therefore, circulation near the image vorticity discussed previously. Notice that the slope of the sectional lift coefficient curve is particularly steep over the last chord length of span from $y/c = 9$ to 10.
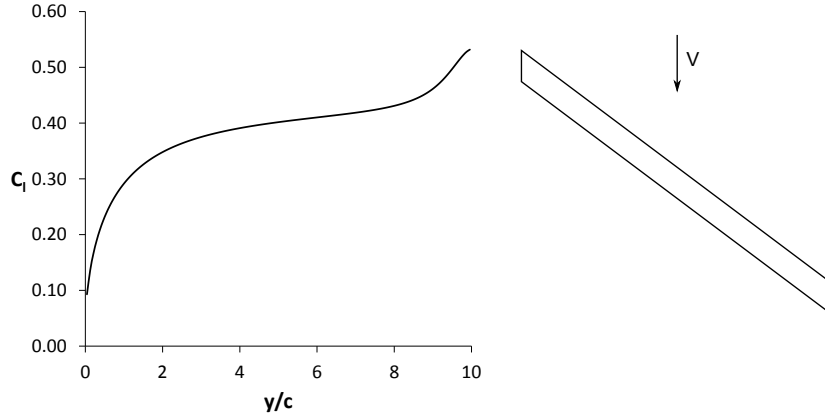
Figure 3.5: Lift Distribution on a Finite, Forward-Swept Wing Predicted by the Vortex Lattice Method

Finally, a swept model was simulated between tunnel sidewalls using two symmetry boundaries. The model has a span of one chord resulting in an aspect ratio of unity which is approximately the AR of the MS model in the IRT. The sweep and run conditions of the first two simulations were again used. Figure 3.6 shows the resulting sectional lift coefficient distribution and the model with symmetry boundaries at $y/c = 0$ and $y/c = 1$.
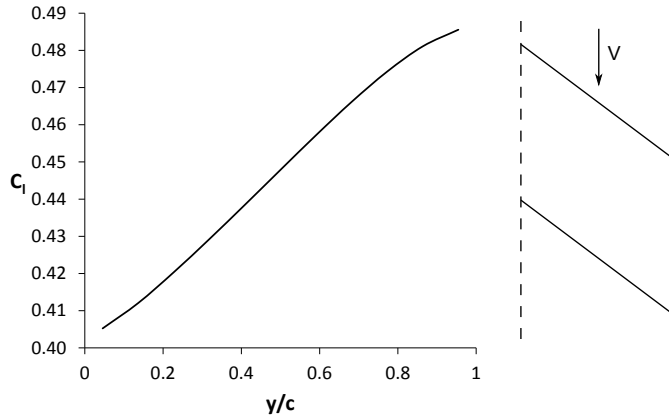
Figure 3.6: Lift Distribution on a Model Between Sidewalls Predicted by the Vortex Lattice Method

Given that C_l increased from about 0.33 to 0.37 over the first chord of span in Figure 3.4 and from about 0.46 to 0.53 over the last chord of span in Figure 3.5, it is not surprising that the C_l increases from about 0.40 to 0.49 over the span of the model in Figure 3.6. The C_l distribution across the $AR = 1$ model with sidewalls can simply be viewed as an average of the C_l distributions of the finite backward and forward-swept wings near the symmetry boundaries. The qualitative features of these results are directly implied by the application of lifting-line theory to the model between sidewalls and are observed in the inviscid solutions

50

that were performed for this research. For instance, Figure 3.7 shows volume streamtraces in the flow about the MS model for the same solution that was shown in Figures 3.1 and 3.2. In the image, the model is oriented such that the flow goes to the right and into the page and the outboard side of the model is on the left with inboard side on the right. The traces were initiated at the IRT inlet boundary at the same z position relative to the leading edge of the model. The increasing z component of the velocity vector with span due to the increased upwash is evident in the path of the streamtraces.
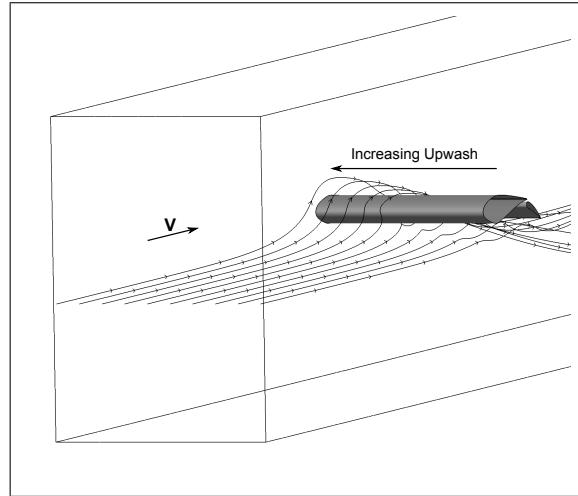
Figure 3.7: Streamtraces Showing the Increase in Upwash with Span for Case WB33 T-4 at $\alpha = 3.67$ deg. and $\delta = 15$ deg.

The application of lifting-line theory to the model with sidewalls not only explains the increase in spanwise loading across the model, but can be used to predict other interesting flowfield features. The difference in circulation between two bound vortices on the lifting line is the shed vorticity and is represented by the overlapping semi-infinite trailing vortex segments of the horseshoe vortices. In Figure 3.3, the outboard trailing segment of one horseshoe vortex is shown adjacent to the inboard trailing segment of the next for clarity. However, these actually overlap and the net vorticity is simply the sum of the two segments. Because circulation increases with spanwise station, the net vorticity shed along the span has a sign pointing upstream. Furthermore, the trailing vortices at either wall are canceled exactly by their image vortex so that even at the outboard end of the model the vorticity is not in the flow direction. This results in a trailing vortex sheet which rolls-up in a manner opposite what is typically seen on a modern transport wing designed for favorable stall characteristics.

Figure 3.8 shows streamtraces released at the trailing edge of the MS model main element for the inviscid flow solution previously presented. An arrow indicates the direction of the flow which is out of the page and

to the left. The net vorticity of the wake clearly points upstream according to the right hand convention, as predicted in the previous discussion.

Figure 3.8: Streamtraces Showing the Wake Vorticity for Case WB33 T-4 at $\alpha = 3.67$ deg. and $\delta = 15$ deg.

By shortening the span of the model, a gap can be added. If a gap is added at the ceiling, the wing tip no longer intersects the ceiling (shown as the right wall in Figure 3.3) and the trailing vortex at the tip is no longer coincident to its image of equal strength. Therefore, the vorticity at the tip is not canceled and the local vorticity in the wake behind the tip will oppose that of the vortex sheet, causing the wake to curl into a "U" shape. This feature is observed in the flow of Figure 3.9a where the MS model was truncated in the spanwise direction by 6 in. (15.2 cm), leaving a gap at the ceiling of the IRT. The inviscid solution was obtained for the conditions of Case WB33 T-4 at $\alpha = 3.67$ deg. and $\delta = 15$ deg. If the gap is moved to the floor, the tip vorticity should then be in the same direction as the wake vorticity, strengthening the vorticity in the upstream direction. This was observed and is shown in Figure 3.9b.

It is clear from these results that the presence of tunnel sidewalls on a swept-wing model causes significantly different flow characteristics than those that exist at the corresponding station of the reference wing in free air. A natural question then becomes whether the 3D model can be altered in some way outside the region of interest so that the flow within the region of interest better matches the flow at the represented station of the reference wing. The idea is to effectively alter the model in such a way as to make it appear as though the actual wing is present. Several ideas for doing this are discussed in the following section.

(a) MS Model with 6 in. Ceiling (Outboard) Gap   (b) MS Model with 6 in. Floor (Inboard) Gap

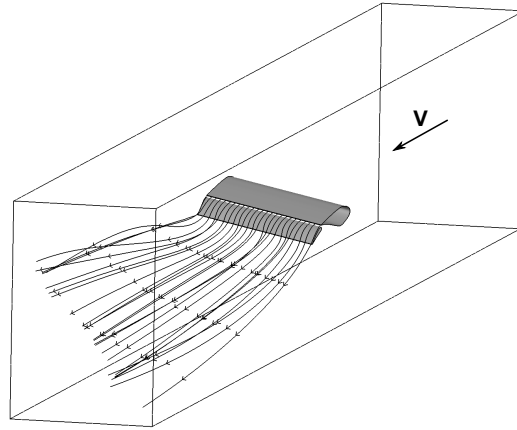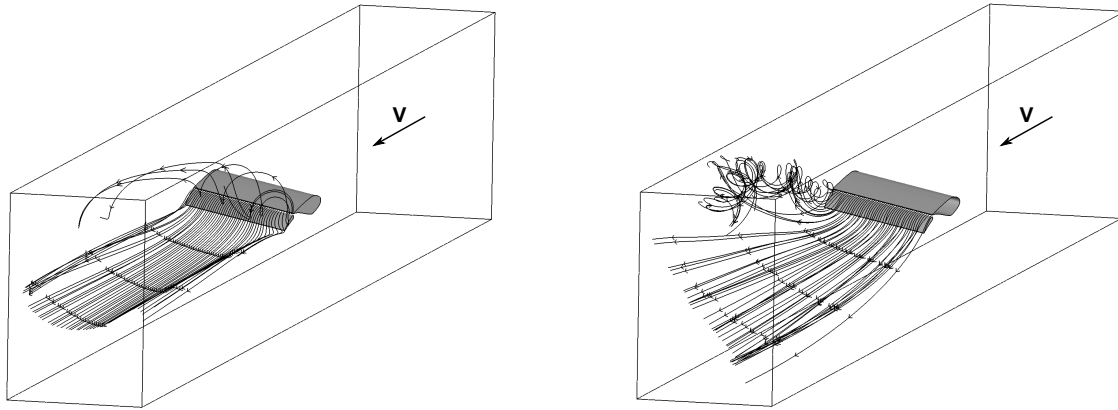Figure 3.9: Streamtraces Showing the Wake Vorticity for Case WB33 T-4 at $\alpha = 3.67$ deg. and $\delta = 15$ deg.

3.2 Spanwise Load Control Techniques

An increase in C_l with span was shown to be a fundamental inviscid effect of a swept model between sidewalls. Because the effect is inviscid, exploration of spanwise load control techniques is computationally affordable and worth further consideration. There are several reasons that a model would potentially benefit from control of the spanwise C_l distribution. The first, to control the attachment line location with span, was mentioned previously in Section 3.1. The second reason is that, left unaltered, the increase in loading with span will cause highly adverse pressure gradients at the ceiling junction which can lead to separation in that region. Distributing the sectional loading more evenly across the span allows the model to operate at a higher overall C_L value before local separation occurs. While there are a myriad of ways in which the model could potentially be modified to change the C_l distribution, two of the simplest and most immediately apparent were attempted; segmented flaps and main element twist.

A segmented flap is simply a flap that is divided into several individual spanwise segments. Dividing the flap into spanwise segments allows local flap deflection angles to vary with span. The concept of segmented flaps was proposed for several reasons. First, it is fairly simple to implement, adding only a small amount of complexity to the design and operation of the test articles. Second, segmented flaps are appealing due to their flexibility during wind tunnel testing. Increasing the deflection of a flap segment increases the local circulation while decreasing the deflection of a flap segment decreases the local circulation. It follows that given a flap system with adequate effectiveness, segment count, and deflection range, the sectional lift distribution of the model can be altered to match that of the reference wing or some other desired distribution

by adjusting the deflection of each segment. The individual deflection angles could be set to achieve even loading, to simulate a spanwise portion of a wing, or to mimic a single segment flap for comparison, to name only a few possibilities.

To explore the effectiveness of segmented flaps, a three segment flap system was simulated on the MS model. The flap which was presented in Section 2.2.3 and shown in Figure 2.7 was divided into three even segments, each having 24 in. (61.0 cm) span, with flap 1 being adjacent to the floor of the IRT, 2 in the center, and 3 adjacent to the ceiling. Flap 2 was set to $\delta_2 = 15$ deg. to match the flap angle of the case previously presented. By deflecting flap 1 at an angle greater than the center flap and flap 3 at an angle less than the center flap, an attempt was made to make the spanwise loading more uniform. An aggressive $\Delta\delta$ of 15 deg. was applied between flap segments such that $\delta_1 = 30$ deg., $\delta_2 = 15$ deg., and $\delta_3 = 0$ deg. To simplify the meshing process, the flap segments were connected with a web in a fashion similar to a seal. This makes the flaps more effective because it prevents flow through the gaps caused by deflecting adjacent segments at different angles. An inviscid solution was then calculated for $\alpha = 3.67$ deg. at the conditions of Case WB33 T-4. The resulting C_P distributions across the span are shown in Figure 3.10a next to the baseline case with a single flap at $\delta = 15$ deg. in Figure 3.10b.

(a) Three Segment Flap

(b) Single Flap
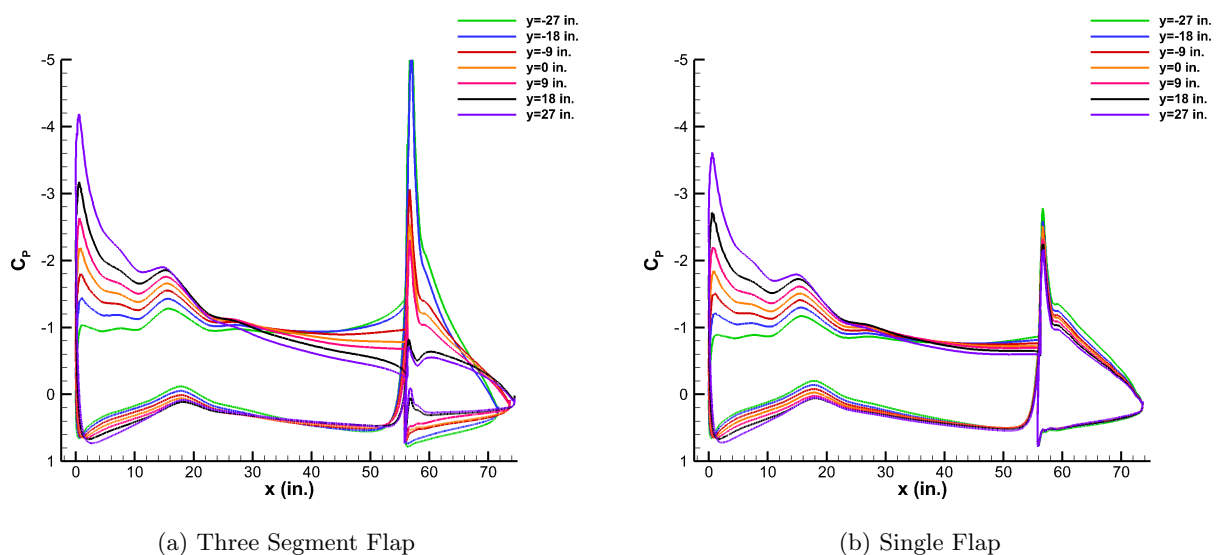
Figure 3.10: C_P Distribution Across Span for Case WB33 T-4 at $\alpha = 3.67$ deg. and Nominal $\delta = 15$ deg.

The local C_P distribution on each *flap segment* is seen to change drastically with the large difference in the deflection of adjacent flap segments. This change in C_P is most notable on the suction surface of the flap where the flap suction peak is changed considerably. The change in the C_P distribution also propagates

onto the main element near the trailing edge with diminishing effects at the midchord and leading edge of the main element. Unfortunately, the majority of the lift is generated near the leading edge of the model. Because each flap segment was unable to significantly impact the C_P distribution near the leading edge at the local station, segmented flaps were not effective in changing the spanwise load distribution in this simulation. It was also observed that for the same nominal flap deflection, the segmented flaps produced a higher overall C_L, suggesting that flap 1 may have a greater overall influence on the model loading than flap 3.

To investigate this further, additional inviscid runs were performed at the same conditions and angle of attack ($\alpha = 3.67$ deg.), but with different flap settings. First, flap 1 was deflected to an angle of $\delta_1 = 30$ deg. with the other two flaps set at $\delta_2 = \delta_3 = 15$ deg. This is effectively the same as the baseline case with a single flap except with flap 1 deflected further in order to isolate its influence on the flow. This was repeated, setting flap 2 at $\delta_2 = 30$ deg. with flaps 1 and 3 at $\delta_1 = \delta_3 = 15$ deg. and again setting flap 3 at $\delta = 30$ deg. with flaps 1 and 2 at $\delta_1 = \delta_2 = 15$ deg. Figure 3.11 shows the C_P distributions that resulted from these runs. As before, increasing the flap angle increases the C_P distribution most noticeably on the upper surface of that flap segment and has a limited influence on the local trailing edge of the main element. What is most clear is that even when only one flap segment is deflected beyond nominal, its effect is not isolated to the local station, but instead increases the loading uniformly across the span. This is clear when the suction peak magnitudes of Figures 3.11a through 3.11c are compared to those of Figure 3.11d. By increasing the deflection of any one of the three flaps, the suction peak at each station from floor to ceiling is increased.

Table 3.1 compares the overall lift coefficient for these four segmented flap cases with that of the single flap case. As was noted previously, even with the deflection of flap 3 reduced by the same value as flap 1 is increased for configuration 1, the C_L value increases, suggesting that flap 1 influences the lift more than flap 3. This is supported by the fact that configuration 2 has a higher C_L than configuration 4. Not surprisingly, Table 3.1 suggests that flap 2 has less influence than flap 1 but more than flap 3.

Table 3.1: C_L on the MS Model with Segmented Flaps for Case WB33 T-4 at $\alpha = 3.67$ deg.

config.	δ_1 (deg.)	δ_2 (deg.)	δ_3 (deg.)	C_L	diff.
1	30	15	0	0.750	+0.053
2	30	15	15	0.836	+0.139
3	15	30	15	0.804	+0.107
4	15	15	30	0.782	+0.086
Single Flap		$\delta = 15$		0.697	-

(a) $(\delta_1, \delta_2, \delta_3) = (30, 15, 15)$ deg.

(b) $(\delta_1, \delta_2, \delta_3) = (15, 30, 15)$ deg.

(c) $(\delta_1, \delta_2, \delta_3) = (15, 15, 30)$ deg.

(d) $\delta = 15$ deg.
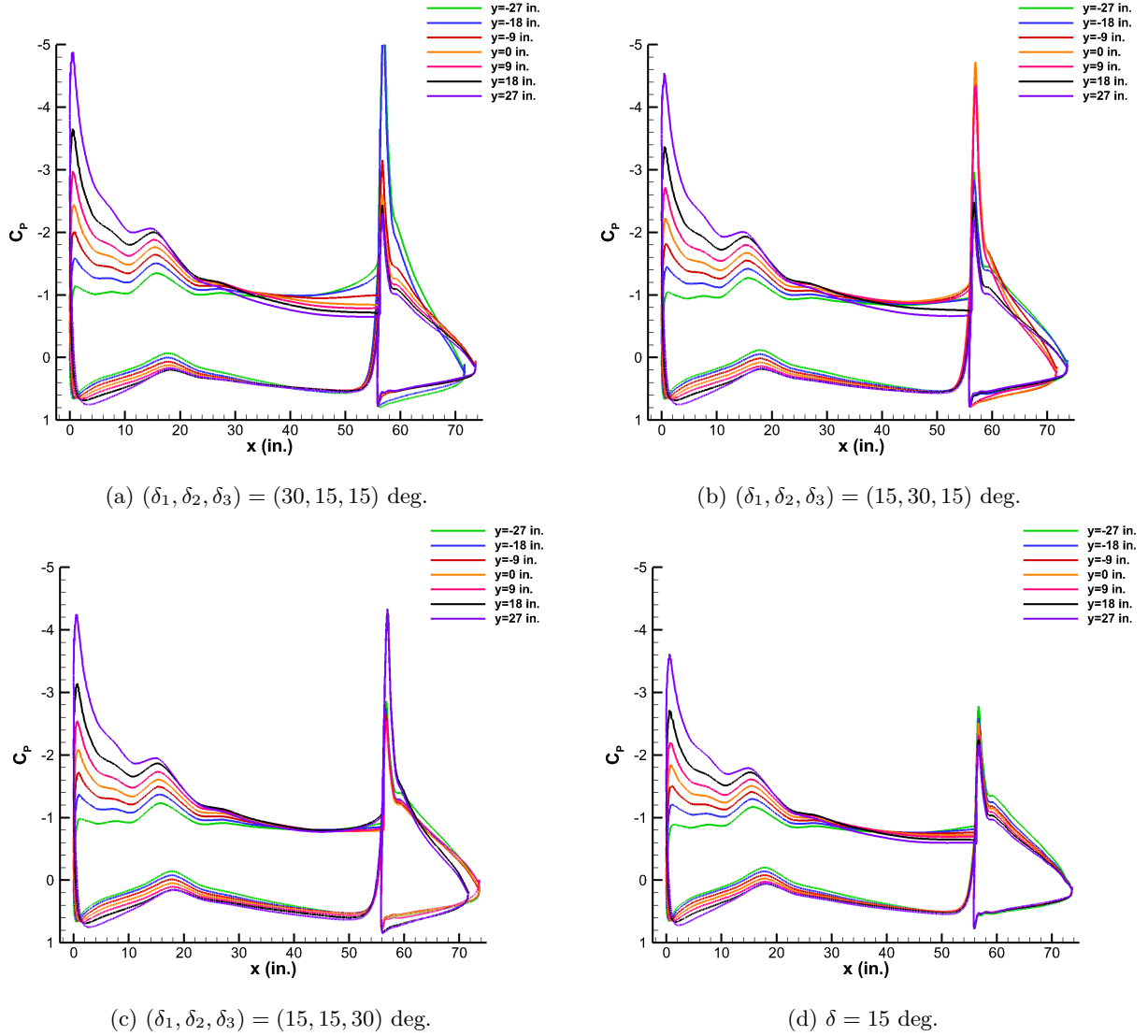
Figure 3.11: C_P Distribution Across Span for Case WB33 T-4 at $\alpha = 3.67$ deg. with Segmented Flaps

The fundamental problem with each of the cases explored thus far is that a given flap segment needs to have a *local* influence on the spanwise C_l distribution whereas the simulations show that each in fact has a largely *global* effect on C_L. It is reasonable to assume that in order to make a flap segment more effective locally, the width of that flap segment relative to the chord should be increased. This can be achieved by changing the aspect ratio of the model. Because the span of the model is fixed due to the size of the IRT test section, the chord of the MS model was changed in order to increase the AR. Because the streamwise chord of the MS model is $c_{sw,h+f} = c_{\perp,fs}/(SF \cos \Lambda_{le}) = 76.98$ in. (1.96 m) and the span is $b = 72$ in. (1.83 m), the aspect ratio of the MS model is near unity, $AR = 0.94$. Models with aspect ratios of $AR = 2$ and 3 were created by scaling the model chord to $c_{sw,h+f} = 36$ and 24 in. (91.4 and 61.0 cm), respectively. The

sweep ($\Lambda_{le} = 37.15$ deg.) and span of the models remained the same. Inviscid flow solutions of the models in the IRT were produced for Case WB33 T-4 at $\alpha = 3.67$ deg. with a single flap at $\delta = 15$ deg. and a three segment flap at $(\delta_1, \delta_2, \delta_3) = (30, 15, 0)$ deg. for each aspect ratio. A spanwise comparison of the resulting C_P distributions is shown in Figure 3.12.

(a) Three Segment Flap & $AR = 2$

(b) Single Flap & $AR = 2$

(c) Three Segment Flap & $AR = 3$
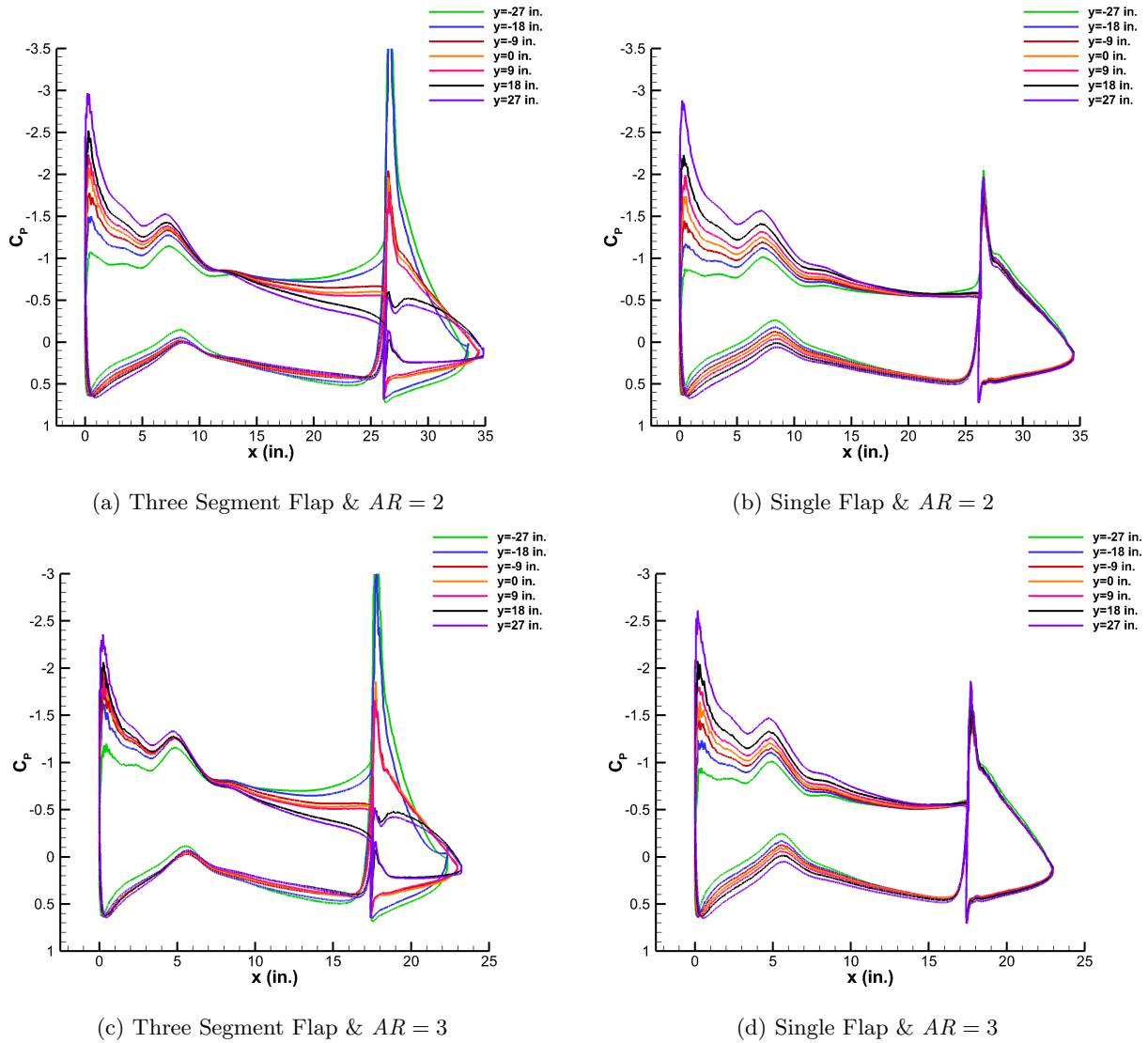
(d) Single Flap & $AR = 3$

Figure 3.12: C_P Distribution Across Span for Case WB33 T-4 at $\alpha = 3.67$ deg. with Segmented Flaps and Varied AR

For the regular MS model with $AR \approx 1$ and a single flap at $\delta = 15$ deg., the difference in the suction peak (minimum C_P) from floor to ceiling was about 2.8, shown in Figure 3.10b. The spanwise increase in suction peak is reduced to about 2.0 for the model with $AR = 2$ of Figure 3.12b. With the $AR = 3$ model

of Figure 3.12d, it is further reduced to about 1.7. This shows that the variation in spanwise loading is reduced by increasing the aspect ratio of the model. The overall C_L is also reduced as shown in Table 3.2. The table also gives the percent by which the C_L is increased using the segmented flap configuration with $(\delta_1, \delta_2, \delta_3) = (30, 15, 0)$ deg. instead of the single flap. The increase in C_L due to segmented flaps decreases as the AR increases to the point that, for $AR = 3$, the increase is so slight that it is not distinguishable at three significant figures of accuracy.

Table 3.2: C_L on the MS Model with Segmented Flaps for Case WB33 T-4 at $\alpha = 3.67$ deg. and Varied AR

AR	Flap	C_L	increase
~ 1	Single	0.697	-
~ 1	Segmented	0.750	7.7%
2	Single	0.546	-
2	Segmented	0.568	4.1%
3	Single	0.524	-
3	Segmented	0.524	0.1%

With both the variation in C_l with span and the overall C_L on the model reduced, it seems clear that increasing AR reduces the effects of sidewalls discussed in Section 3.1. That the effects of the sidewall symmetry boundaries are reduced simply by increase the model AR is not surprising because it results in an increase in nondimensional span, b/c, making the model more like an infinite, swept wing which has uniform spanwise loading.

Comparing the plots on the left in Figure 3.12 to those on the right, it becomes clear that the segmented flaps begin to have an effect on the C_P distributions near the leading edge for $AR = 2$ and become effective in nearly removing the spanwise variation in C_P near the leading edge for $AR = 3$. Contrast this with the $AR \approx 1$ model in Figure 3.10, in which case the segmented flaps had no local effect on the C_P distribution near the leading edge of the main element (where most of the lift is generated). The ability of the three segment flap system to reduce the change in C_P distribution and, therefore, C_l, at the leading edge is improved by increasing the aspect ratio on the MS model. Because the attachment line location is impacted by the flow in this region, one would expect spanwise control of its position to be attainable. Nonetheless, even with the $AR = 3$ model the C_P distribution at the leading edge was not made uniform. Furthermore, the aggressive difference in flap angle of 15 deg. between flap segments is not ideal. In practice, one would like to achieve comparable results at a lower $\Delta\delta$, requiring an even higher AR. Finally, because these simulations are inviscid and no gaps between adjacent flap segments were represented, these results remain optimistic.

It is likely that when viscosity and properly toleranced gaps are introduced, an aspect ratio of 4 or more would be required to give similar results to those shown. To make spanwise control of the C_l distribution on the model practical using segmented flaps, the chord would have to be scaled far beyond what could be considered a large-scale model. Thus, segmented flaps are not a practical solution for this research, which focuses on large-scale models.

Because the increase in C_l with span is fundamentally caused by an increase in effective α due to the increase in upwash with span, physically twisting the model to change the local α promises to be an effective method of changing the spanwise load distribution on the model.

To explore the effectiveness of twist, the MS model was twisted geometrically about the quarter chord by 10 deg. from floor to ceiling. Because the twist causes the trailing edge of the model to trace a helical rather than linear path across the span of the model, the flap was removed. This method of twisting also changes the geometry of the leading edge so that the leading edge of the model only matches that of the CRM65 at the IRT centerline. To maintain a linear trailing edge and unaltered leading edge, the model could instead be twisted aerodynamically; meaning that the sectional design of the model could vary with span such that the leading edge is constant up to the upper and lower leading-edge extents with the aft camber and trailing edge elevation (controlled by C_{m0} and γ, see Section 2.2.1) varied. Due to the complexity of such a design, it was not done for this preliminary investigation of twist. Even if the trailing edge were linearized, the flap angle would become ambiguous because the flap hinge line would no longer be in the normal direction. Whether a single element hybrid model can be used to produce ice shapes for a range of conditions will be discussed in more detail in Section 3.6.

Because a flap was not present, the twisted MS model was rotated to an angle of attack of $\alpha = 10$ deg. to increase the C_L so that the centerline C_P distribution on the leading-edge portion of the model would be similar to that of the standard, untwisted MS model with $\alpha = 3.67$ deg. and $\delta = 15$ deg. An inviscid simulation was performed for the conditions of Case WB33 T-4. The resulting C_P distributions across the span are compared in Figure 3.13. Twisting the main element of the model nearly eliminated the increase in suction peak across the span by physically compensating for the upwash by changing the local angle of attack at each station. With a nearly constant suction peak, the twisted model has a much more uniform sectional C_P distribution across the span. Because the area contained by each sectional C_P distribution is approximately equal, it can be deduced that the C_l is approximately constant with span. While these results are promising, a twist of 10 deg. is very large over a span of only 72 in. (1.83 m). This large twist angle introduces other complexities to the model. For instance, the mounting plate at the floor and pin at the ceiling of the IRT become more distant from the mold lines of the model at the root and tip, making the

physical mounting of the model more challenging. Fabrication costs should also be considered when model complexity is increased.

(a) Twisted Main Element Only, $\alpha = 10$ deg.

(b) Untwisted Model, $\alpha = 3.67$ deg. and $\delta = 15$ deg.
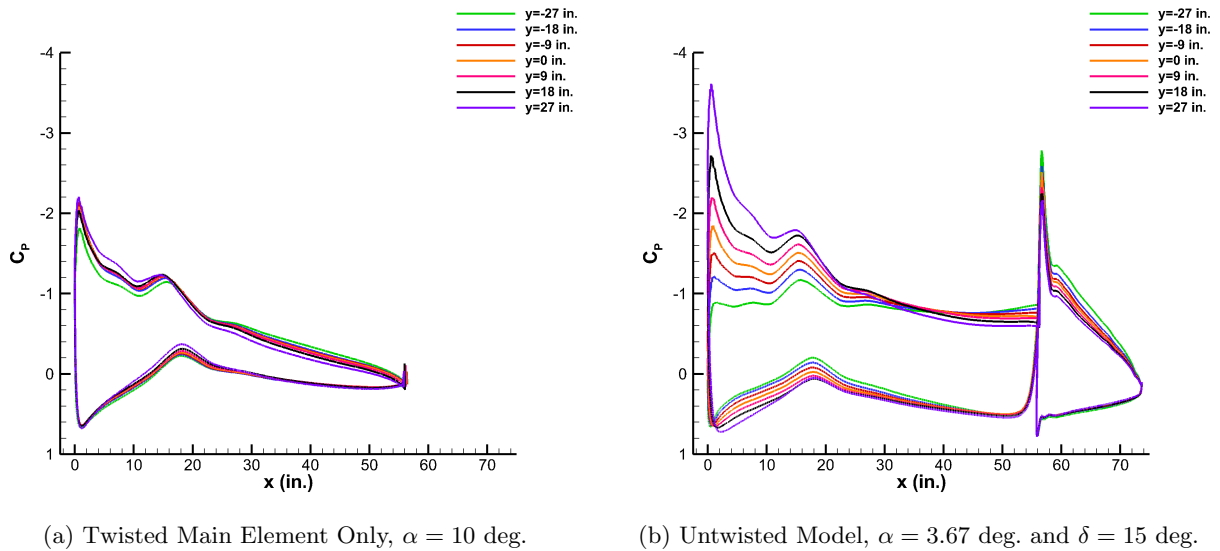
Figure 3.13: C_P Distribution Across Span for Case WB33 T-4

Streamtraces in the wake of the twisted MS model are shown in Figure 3.14. Twisting the model makes the effective angle of attack with span more uniform. Because the vorticity shed into the wake is the change in circulation along the lifting line, the weak vorticity in the wake behind the twisted model is not surprising because the loading (and, therefore, the circulation) is more uniform.

Many methods for altering the spanwise load distribution or attachment line location of a 3D hybrid model exist, but most will increase the complexity of model design, fabrication, and testing. As with all design decisions, the optimal balance between the anticipated increase in experimental fidelity versus the additional time and cost to implement the solution must be found. If the variation in ice shape over the region of interest (defined in Section 2.2.3) is acceptably small, the additional cost and complexity of a model with spanwise C_l control is not justified. The extent to which the attachment line and ice shape are affected by the spanwise variation in loading on the MS model will be discussed in the coming sections. For the purposes of this research, the change in ice shape across the region of interest is reasonable and the ability of the standard, untwisted MS flapped-hybrid model to generate ice shapes representative of the baseline ice shapes is sufficient. This conclusion is based on the results of LEWICE3D simulations, shown and discussed in the sections to follow.
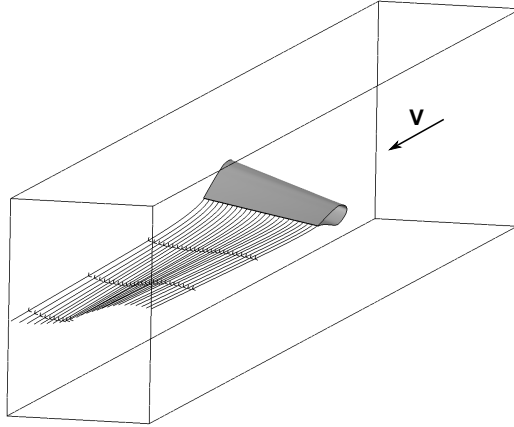
Figure 3.14: Streamtraces Showing the Wake Behind the Twisted MS Main Element at $\alpha = 10$ deg. for Case WB33 T-4

3.3 Attachment Line Position

The increase in C_l with span due to the presence of sidewalls on a swept model results in a significant change in attachment line position relative to the hilite across the span. It was shown by Fujiwara et al. [13] that the stagnation point has a first-order impact on ice shape for 2D hybrid models. It would be expected that on a 3D model, the attachment line would have a comparable effect on ice shape. The attachment line on the MS flapped-hybrid model can be adjusted by setting the angle of flap deflection or by changing the model angle of attack. The effect of flap angle and angle of attack are discussed below.

3.3.1 Flap Angle Effects

Case WB33 T-4, $\alpha = 3.67$ deg., $\delta = 12$, 15, and 18 deg.

Flow calculations with viscous effects at the nominal angle of attack and three flap deflections were performed for the conditions of Case WB33 T-4 in order to demonstrate the effects of flap angle on ice shape. By varying the flap deflection, the attachment line location relative to the hilite was moved at the tunnel centerline. Figure 3.15 shows a C_P contour plot with surface streamtraces for $\delta = 15$ deg. which matched the CFB attachment line location at IRT centerline. Flow is from left to right in both figures. The effects of the spanwise increase in suction peak magnitude (and loading) due to the combined effects of model sweep and tunnel floor and ceiling discussed in Section 3.1 are immediately apparent in the pressure on the upper surface of the model. The pressure near the leading edge on the upper surface decreases with span considerably. A

large separation region at the ceiling junction on the upper surface is caused by the highly adverse pressure gradient that results from the amplified suction peak near the ceiling, as was predicted in Section 3.1.

(a) Low Pressure Surface

(b) High Pressure Surface
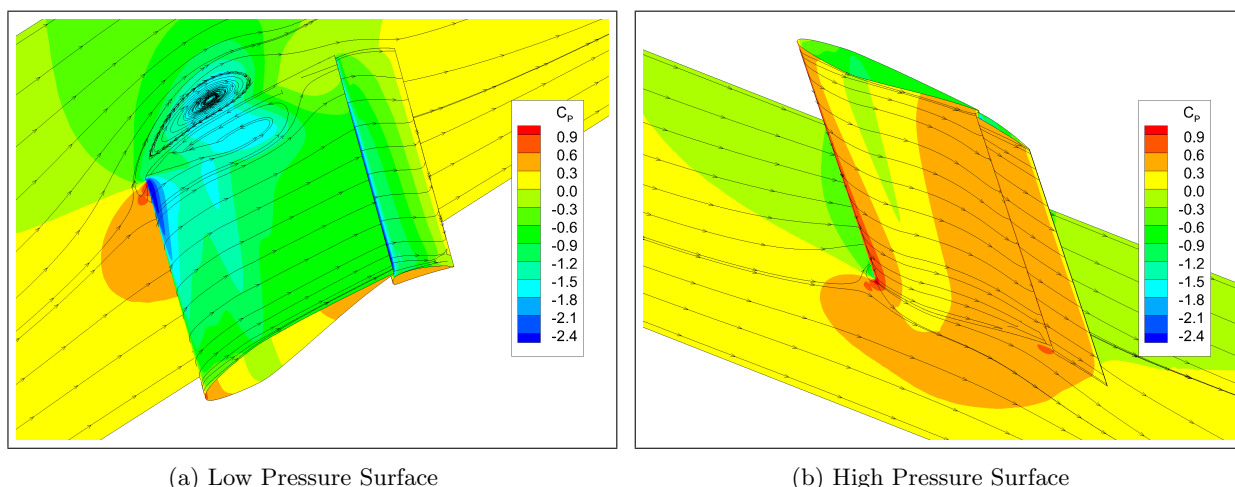
Figure 3.15: C_P Contour for Case WB33 T-4 at $\alpha = 3.67$ deg. and $\delta = 15$ deg.

Due to the high level of separation at the ceiling junction, care was taken to inspect the flow in the region of interest to ensure that there was no separation in that area. The accuracy of the ceiling junction separation region should be treated skeptically. It is often the case with RANS simulations that numerical viscosity resulting from discrete meshes causes separation at lower angles of attack - or the solver exaggerates separation - as compared to experimental results. For instance, Mani et al. [17] found that separation at the wing-body junction of the CRM was unrealistically large in their full Navier-Stokes (NS) solutions for the fourth drag prediction workshop. Using the thin-layer NS equations, they were able to better predict the levels of separation seen experimentally [37]. The use of the thin-layer NS equations was not attempted in this research because the levels of separation, whether realistic or exaggerated, have little affect on the icing in the region of interest and the true level of separation can not be ascertained for comparison until the model design is already finalized and used to fabricate and test an article in the IRT. Flow solutions for $\delta = 12$ and 18 deg. are qualitatively similar to that of Figure 3.15 with slightly different surface pressures and are thus not shown.

The attachment line position relative to the hilite for these three cases is shown in Figure 3.16 where the horizontal line represents the CFB target attachment line position from the MS station on the CRM65. Recall that the sign convention used in this research makes wrap distance, s, positive for attachment line positions below the hilite. The attachment line position on the hybrid model moves farther from the hilite on the lower surface of the leading edge as the flap deflection, and therefore circulation, is increased. The

slope of the attachment line curve does not change appreciably for these small changes in flap angle. A flap deflection of $\delta = 15$ deg. provides the correct position of attachment line at the IRT centerline ($y = 0$). A comparison of the centerline C_P distributions of these three solutions overlaid on that of the CRM65 at the MS station is given in Figure 3.17.
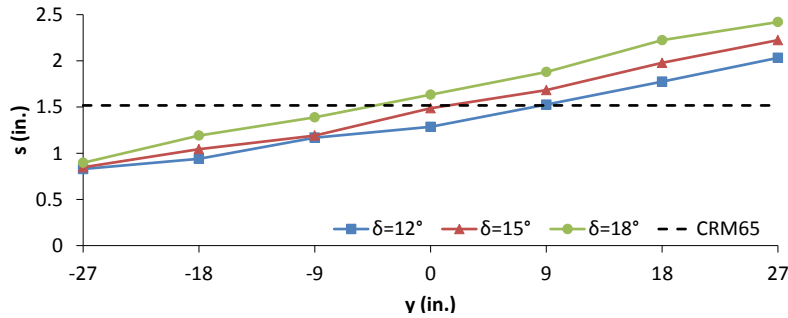
Figure 3.16: Spanwise Attachment Line Location for Case WB33 T-4 at $\alpha = 3.67$ deg.
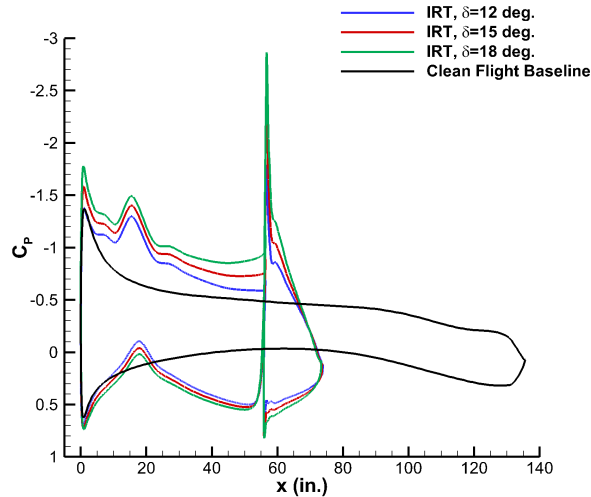
Figure 3.17: IRT Centerline C_P Distribution Comparison for Case WB33 T-4 Between CRM65 MS Station and IRT Model at $\alpha = 3.67$ deg. and $\delta = 12$, 15, & 18 deg.

The baseline C_P is well matched by the hybrid model in the leading-edge region where the full-scale geometry is used. The suction peak is best matched for $\delta = 12$ deg. while, as shown in Figure 3.16, the attachment line location is best matched at $\delta = 15$ deg. Figure 3.18 compares the ice shapes at the IRT centerline that result from LEWICE3D icing simulations on the three flow solutions presented above. That matching the stagnation point location rather than suction peak magnitude is more important in matching

ice shapes for hybrid airfoils was shown by Fujiwara et al. [13], the former having a first-order impact and the latter a second. When comparing the shapes of the IRT simulation to that of the IFB in Figure 3.18, the analog appears to be true for 3D hybrid models as well. Though the $\delta = 12$ deg. case better matches the suction peak magnitude of the baseline, it is case $\delta = 15$ deg. with the closer agreement in attachment line location that best matches the ice shape. Due to the upper extent on a hybrid where the full-scale leading edge of the reference wing transitions into the redesigned aft section, the suction peak on a hybrid is often higher for the same attachment line location. This results from the flow accelerating around a sharper corner than it would on the reference geometry. Possible reasons for the difference in ice thickness will be given in Section 3.5.

As the flap angle increases, the circulation on the model does also, driving the attachment line farther down the leading edge. This results in ice shapes with smaller horn angles as flap angle is increased. It is also interesting to note that the width of the ice shapes in the wrapwise sense decreases as the wrap distance to the attachment line location, s, increases. The surface distance from the hilite to the attachment line location at IRT centerline for the three cases is presented in Table 3.3 which, given Figure 3.18, gives some measure of the sensitivity of attachment line position and ice shape to flap angle. The attachment line position on the CRM65 wing at the MS station is $s = 1.517$ in. (3.85 cm) and the difference between this value and that of each flap angle is given in Table 3.3.
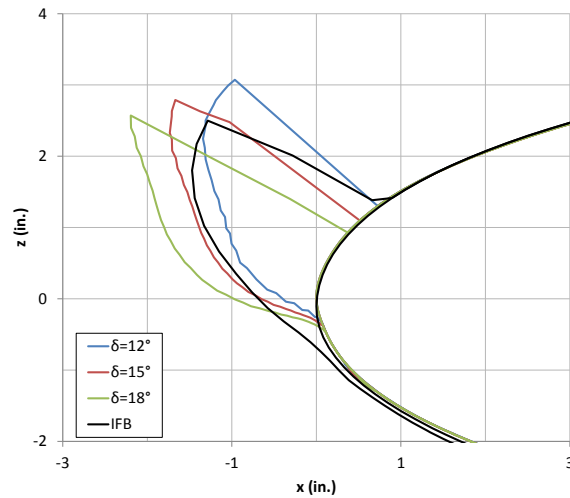
Figure 3.18: Comparison of Ice Shapes for Case WB33 T-4 in IRT at $\alpha = 3.67$ deg. and Several Flap Angles

The impingement efficiency and heat transfer coefficient distributions for the three cases are given in Figure 3.19. While the overall profile of the β distributions are nearly identical, a small shift due to the

64

difference in attachment line location for each δ can just be made out at this scale, moving β toward the lower surface as δ increases. The h_c changes more substantially with different flap angles due to the increase in the suction peak at higher δ which manifests itself in a higher value of h_c on the upper surface of the model. A shift in s is seen in the h_c curves as it was in the β distributions.

Table 3.3: IRT Centerline Attachment Line Positions for Case WB33 T-4 at $\alpha = 3.67$ deg. and Several Flap Angles

	α (deg.)	δ (deg.)	s (in.)	diff. (in.)
IRT	3.67	12	1.286	-0.232
IRT	3.67	15	1.486	-0.031
IRT	3.67	18	1.634	$+0.116$
CFB	3.67	-	1.517	-
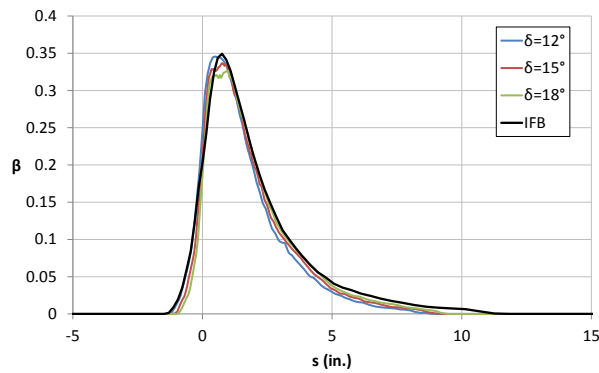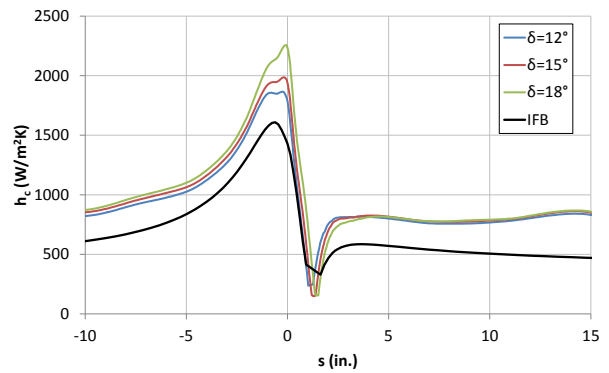
(a) Impingement Efficiency (b) Heat Transfer Coefficient

Figure 3.19: Comparison of β and h_c for Case WB33 T-4 in IRT at $\alpha = 3.67$ deg. and Several Flap Deflections

3.3.2   Angle of Attack Effects

Case WB33 T-4, $\alpha = 5.25$, 5.50, and 5.75 deg., $\delta = 5$ deg.

Flow simulations were run for the conditions of Case WB33 T-4 over several angles of attack at a fixed flap angle of $\delta = 5$ deg. in order to match the attachment line position of the MS station of the CRM65 wing at an α other than the baseline value. Three calculations at $\alpha = 5.25$, 5.50, and 5.75 deg. were performed before a satisfactory match was achieved. While this was primarily done to study the ice shapes that result

when the attachment line position is matched at off-case angles of attack (see Section 3.6), it is instructive to compare the ice shapes resulting from LEWICE3D simulations of all three of these solutions, rather than just the one that best matches attachment line position.

Figure 3.20 shows the low and high pressure surfaces of the MS model for $\alpha = 5.50$ deg. and $\delta = 5$ deg. The resulting flow is clearly similar to that shown in Figure 3.15 with $\alpha = 3.67$ deg. and $\delta = 15$ deg. The solutions obtained at $\alpha = 5.25$ and 5.75 deg. were qualitatively similar and are thus not shown for brevity.

(a) Low Pressure Surface   (b) High Pressure Surface
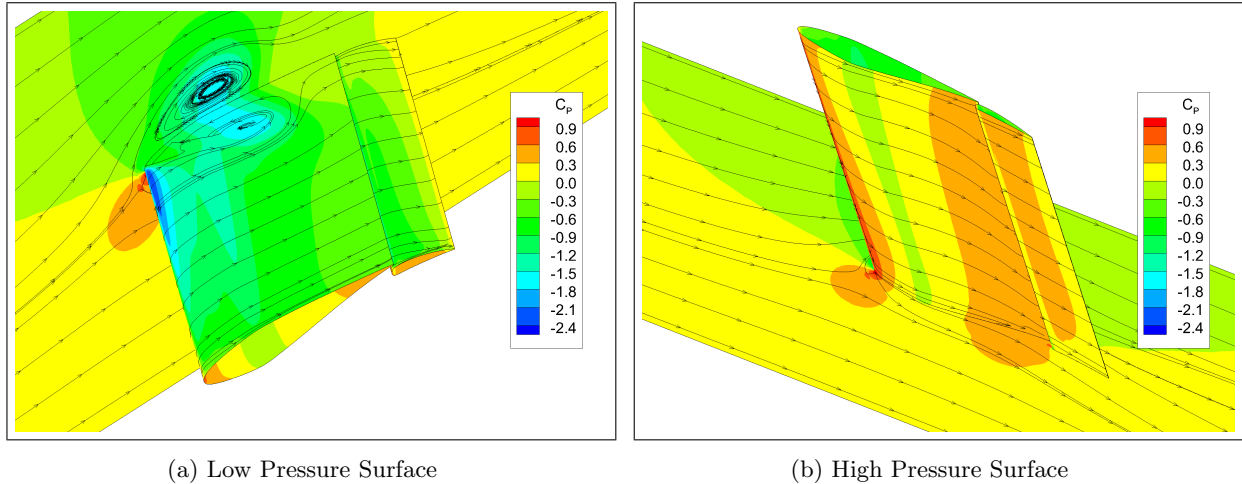
Figure 3.20: C_P Contour for Case WB33 T-4 at $\alpha = 5.50$ deg. and $\delta = 5$ deg.

The attachment line position with span for these three simulations is shown in Figure 3.21. The horizontal dashed line again indicates the location of the attachment line at the MS station on the CRM65 for Case WB33 T-4. It is clear that for $\delta = 5$ deg., the run with $\alpha = 5.50$ deg. best matches the attachment line position at IRT centerline ($y = 0$). The shift in attachment line location is very small for the small differences in angle of attack. The wrap distance to the attachment line for each α is given in Table 3.4. The position of the attachment line from the CFB is also given along with the difference between it and each IRT run.

Table 3.4: IRT Centerline Attachment Line Positions for Case WB33 T-4 at Several Angles of Attack and $\delta = 5$ deg.

	α (deg.)	δ (deg.)	s (in.)	diff. (in.)
IRT	5.25	5	1.339	-0.178
IRT	5.50	5	1.536	$+0.018$
IRT	5.75	5	1.585	$+0.067$
CFB	3.67	-	1.517	-
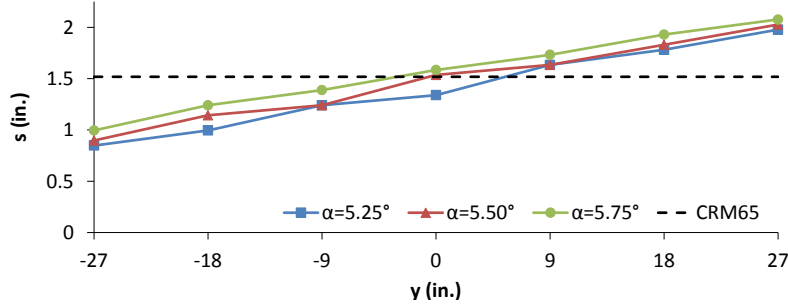
Figure 3.21: Spanwise Attachment Line Location for Case WB33 T-4 at $\delta = 5$ deg.

Ice shapes produced by LEWICE3D for these three runs are shown in Figure 3.22. For reference, the ice shape from the IFB is also shown. Though the difference in ice thickness for the IRT simulations makes it difficult to choose a best match, $\alpha = 5.50$ deg. results in an ice shape with a good match in horn angle. Furthermore, matching the attachment line position in the IRT flow simulation to that of the CFB does not guarantee that the attachment line locations determined by LEWICE3D will match; a point which will be discussed in more detail in Section 3.3.
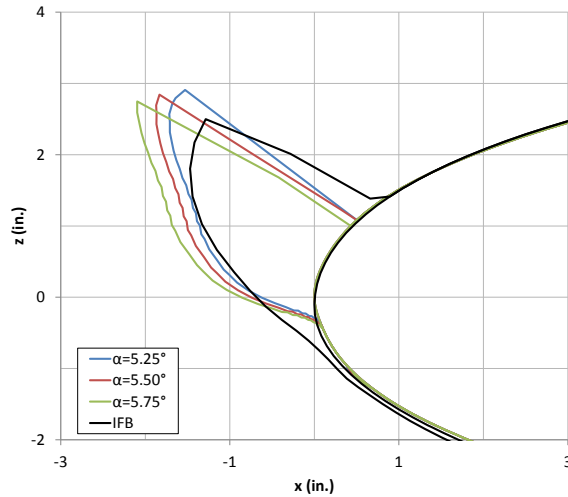
Figure 3.22: Comparison of Ice Shapes for Case WB33 T-4 in IRT at Several Angles of Attack

The β and h_c distributions corresponding to these ice shapes are shown in Figure 3.23. Only very slight differences between the β and h_c distributions can be distinguished. Yet, even for this small difference in α, β, and h_c, a measurable difference in ice shape results. This highlights the sensitivity of ice shape to attachment line location and suggests that the first-order significance of stagnation point to ice shape discussed by Fujiwara et al. [13] for 2D hybrids holds for attachment line and 3D hybrid models as well.

67
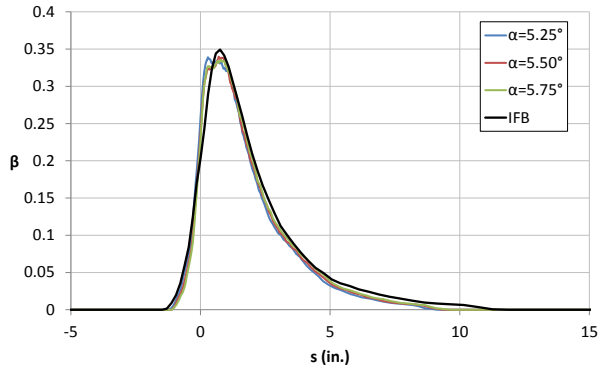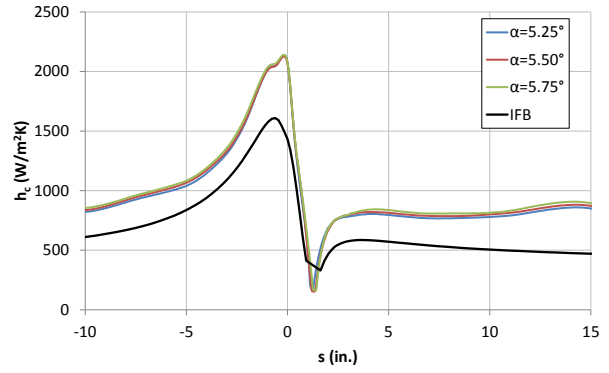
(a) Impingement Efficiency (b) Heat Transfer Coefficient

Figure 3.23: Comparison of β and h_c for Case WB33 T-4 in IRT at Several Angles of Attack

The angle of attack of a hybrid model for an icing experiment is generally set to match the reference case so that the global angle of incidence at which far-field droplets impinge on the leading edge is matched. However, because a change in α can be used to adjust the attachment line position in a fashion similar to a change in δ, there are times when it is beneficial to do so. For instance, the flap may have stalled at a lower deflection than was expected, requiring a higher angle of attack to match the attachment line location. Another example is a model which requires manual adjustment of the flap setting so that during icing runs, *in situ* tuning of the attachment line location can only be accomplished by rotating the turntable. However, using α rather than δ to match attachment line positions is done under the assumption that the ice shapes that result will be representative of the baseline despite the fact that droplets from the icing cloud approach the full-scale leading edge on the model at a different angle than they approach the true leading edge on the baseline wing. This assumption will be discussed in Section 3.6 where the ice shapes for the cases shown in this and the previous section will be compared in this context.

It has been shown in this section that increasing the angle of attack can be used to move the attachment line lower on the leading edge of the model and in Section 3.3.1 that the same is true for increasing the flap angle. This implies that for any desired attachment line position within the capabilities of the model, there are many combinations of α and δ that can be used to reach it. In order to present these combinations in a meaningful way, an aerocal can be constructed as described in Section 2.2.3. Such an aerocal is shown in Figure A.1. The aerocal has as its horizontal axis the angle of attack of the CFD simulations. The vertical axis represents the attachment line position relative to the hilite. Curves representing fixed flap angles are plotted so that the wrap distance associated with any pair of α and δ is easily obtained.

A broad array of 2D RANS solutions with the IRT walls form the foundation of the aerocal. Because 2D CFD tools are computationally much less expensive than 3D, a larger number of simulations can be performed at high resolution to establish basic trends in attachment line position. These trends are used to predict the flap deflections needed to match the attachment line positions from the CFB, which are also plotted on the aerocal. Individual 3D RANS simulations are added to the chart to establish correlation between 2D and 3D simulations. Each 3D point on the aerocal represents the attachment line position at the IRT centerline ($y = 0$).

As mentioned, α is generally set to be that of the reference case. This results in a specific δ required to obtain the correct attachment line position. However, if a specific flap angle is needed or desired, a corresponding angle of attack could also be taken from the aerocal. The value of having an aerocal plot is obvious for both the design phase, during which the CFD aerocal is used, and for the wind tunnel testing campaign, during which an actual aerodynamic calibration can be experimentally obtained and used to set the test angles in subsequent icing tests.

3.3.3   LEWICE3D Attachment Line Determination

Case WB71 T-6, $\alpha = 4.40$ deg., $\delta = 15$ deg.

A flow solution for the conditions of Case WB71 T-6 at $\alpha = 4.40$ deg. and $\delta = 15$ deg. was generated to produce ice shapes for this case on the 3D MS model. Contour plots of the C_P on the surface of the model are shown in Figure 3.24 along with surface streamtraces.

(a) Low Pressure Surface   (b) High Pressure Surface
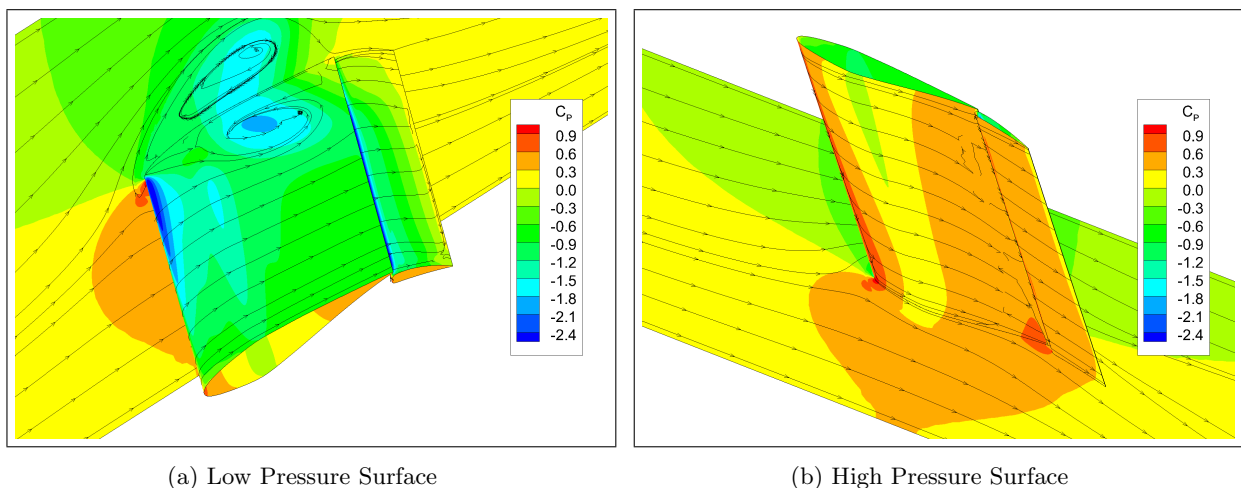
Figure 3.24: C_P Contour for Case WB71 T-6 at $\alpha = 4.40$ deg. and $\delta = 15$ deg.

A large separation bubble similar to previous results is present at the ceiling junction. This region is slightly larger due to the higher model loading that results from the higher α corresponding to Case WB71 compared to Case WB33. The flow was inspected in detail to ensure that no separation occurred in the region of interest for icing simulations. Figure 3.25 shows the attachment line position with the span of the model.
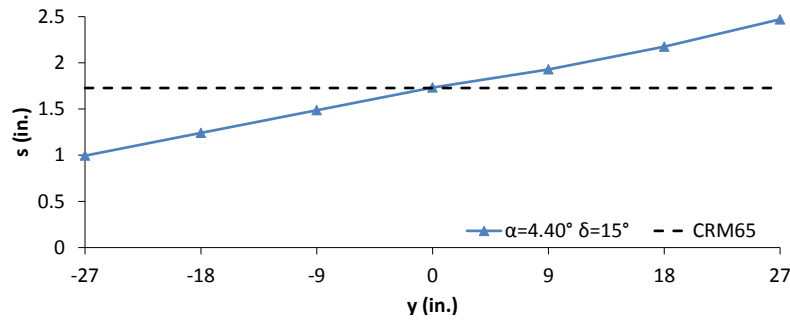
Figure 3.25: Spanwise Attachment Line Location for Case WB71 T-6 at $\alpha = 4.40$ deg. and $\delta = 15$ deg.

The attachment line location from the CRM65 is very well matched at the IRT centerline ($y = 0$), differing from that of the CFB by only 0.005 in. (0.13 mm). The attachment line position is determined by finding the point on the model or wing surface with the maximum C_P value at each y position. This criteria is used because it is very simple and unambiguous. However, it does not allow an attachment line position to fall between two nodes of the mesh unless some type of curve fit is used. Due to the resolution of the mesh used in OVERFLOW to produce the CFB results, the position of the attachment line at the MS station of the CRM65 wing is known with an uncertainty in s of about ± 0.15 in. (3.8 mm). The uncertainty of the attachment line position for the Fluent meshes used in the IRT simulations is about ± 0.025 in. (0.64 mm). Therefore, the attachment line position on the IRT model may differ by as much as 0.18 in. (4.6 mm), with the bulk of the uncertainty inherent to the flight baseline flow solution.

Further differences in attachment line location can result from the fact that LEWICE3D does not use the same criteria for determining its position. At each section of interest in a LEWICE3D simulation, the attachment line position is determined to be the point on the surface of the wing where the component of the velocity contained in the cut plane and tangential to the surface is zero. Said differently, it is the point where the edge velocity reverses direction. This method results in attachment line positions that do not necessarily agree with those found using $C_{P,max}$ and, because interpolation is used, do not have to fall on mesh nodes.

The attachment line position determined by LEWICE3D, called the stagnation plane, is included with the simulated ice shapes in the code's output files. Figure 3.26 shows the ice shapes (blue) and stagnation planes (red) on the MS model at three spanwise positions, $y = -6$, 0, and $+6$ in. When these attachment line locations determined by LEWICE3D for the IRT simulation were compared to that of the IFB, it was found that the difference in s at the $y = 0$ position was 0.158 in. (4.0 mm). However, at the $y = +6$ in. (15.2 cm) position, the IRT and IFB attachment line positions differed by only 0.010 in. (0.25 mm).
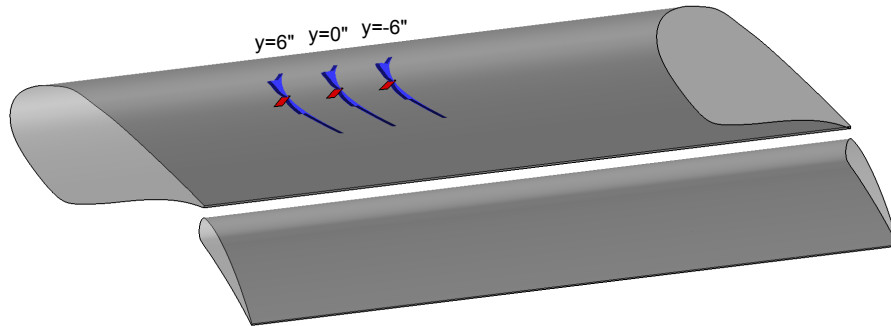
Figure 3.26: LEWICE3D Ice Shapes (Blue) and Stagnation Planes (Red) at $y = -6$, 0, & $+6$ in. for Case WB71 T-6

Figure 3.27 shows the IRT ice shapes at $y = 0$ and $+6$ in. compared to that of the IFB. While both IRT ice shapes have thicker ice through the horn region, it is clear that the ice at $y = +6$ in. compares better with the IFB shape, matching the lower icing extent and the general features of the shape.
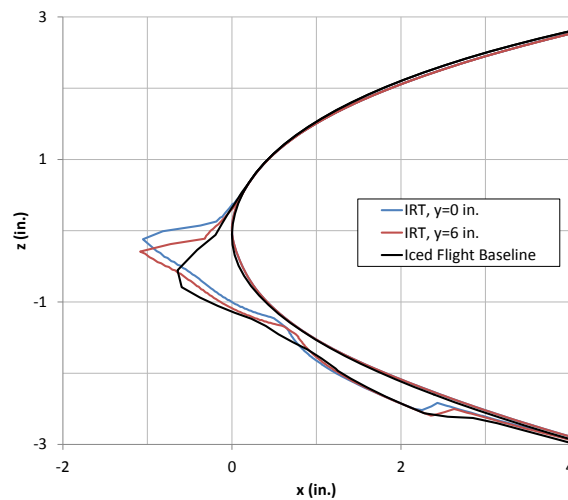
Figure 3.27: Comparison of Ice Shapes for Case WB71 T-6 in IRT at the $y = 0$ and 6 in. Stations

Figure 3.28 compares the β and h_c distributions at these two spanwise positions to those of the IFB. The β distributions for both IRT runs are very similar and match well with the IFB except for a slightly higher region near β_{max} from about $s = 0$ to 1 in. The h_c from the IRT solutions, while slightly lower, match fairly well with the IFB. The difference in h_c between the IRT runs is due to the difference in attachment line position, $y = +6$ in. having a larger s and higher suction peak, causing higher heat transfer on the upper surface.

(a) Impingement Efficiency

(b) Heat Transfer Coefficient
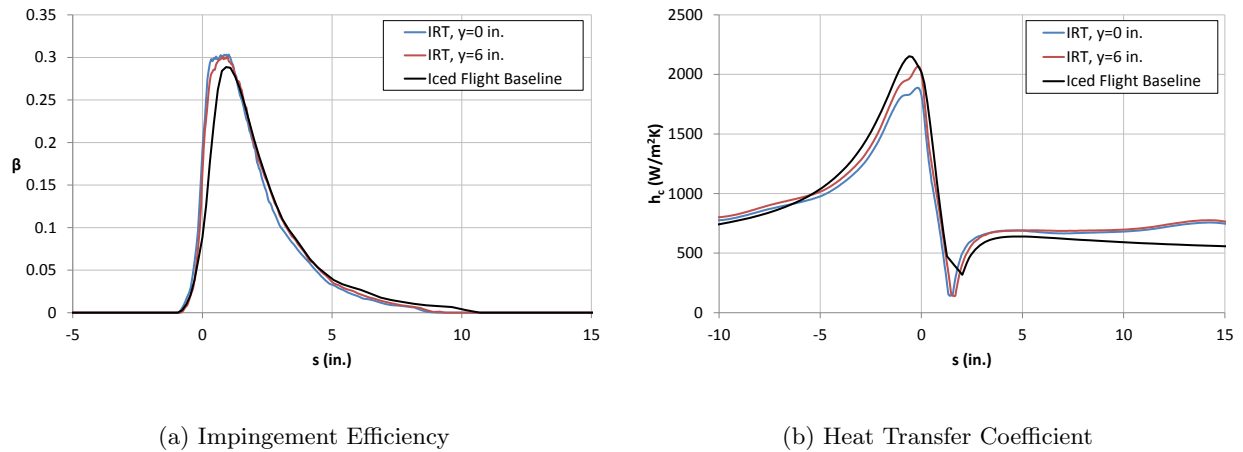
Figure 3.28: Comparison of β and h_c for Case WB71 T-6 in IRT at Several Attachment Line Locations

Because the attachment line position determined by LEWICE3D can differ from that which is calculated using $C_{P,max}$, a good agreement in attachment line position cannot be guaranteed prior to running LEWICE3D. This means that though a flow solution may appear to have an attachment line position matching that of the reference case, LEWICE3D may determine a different attachment line location resulting in reduced ice shape agreement. For this reason it is recommended that attachment line locations as determined by LEWICE3D be compared after the icing simulations are performed. It is not always the case that they will differ from those calculated using other methods, but clearly they can. The attachment lines calculated by LEWICE3D compared well to those presented in the results for the other simulations to follow.

3.4 Altitude Effects

The IFB icing simulations were run at conditions representing those from flight at altitude. Because the IRT is at an elevation of approximately 800 ft. (244 m) above sea level and is not pressure controlled, the pressure and density are higher than would be seen in flight. Altitude effects can be considered by running

LEWICE3D using the IRT flow solution produced in Fluent at both IRT and flight baseline conditions. A Langmuir D droplet distribution was used when icing simulations were performed at the flight baseline conditions so that any differences in droplet distribution did not contribute to the resulting ice shapes. Comparing the IRT flow solution at flight baseline conditions with the actual baseline results also serves the purpose of removing the effects of pressure, density, and droplet distribution on ice shape to isolate contributions of the flow solution itself. Care must be taken when running a flow solution in LEWICE3D at conditions other than those at which the flow solution was generated. This can result in a mismatch in Mach number effects that can in turn impact the accuracy of the results. The flow solutions of this research were produced at IRT conditions, making the LEWICE3D results at baseline conditions only approximations. Nevertheless, these results are accurate enough to serve the purpose of investigating altitude effects.

The ice shapes at the IRT centerline resulting from running icing simulations at IRT pressure and baseline pressure for Case WB33 T-4 are shown in Figure 3.29. The Fluent solution used for these icing simulations has $\alpha = 3.67$ deg., $\delta = 15$ deg., and was described in Section 3.3.1. The IFB ice shape on the CRM65 wing at the MS position is overlaid for comparison. The ice shapes are shown in the plane whose normal is tangent to the hybrid model leading edge. Both IRT ice shapes have horn angles which compare well with the IFB ice shape, but with larger horn lengths.
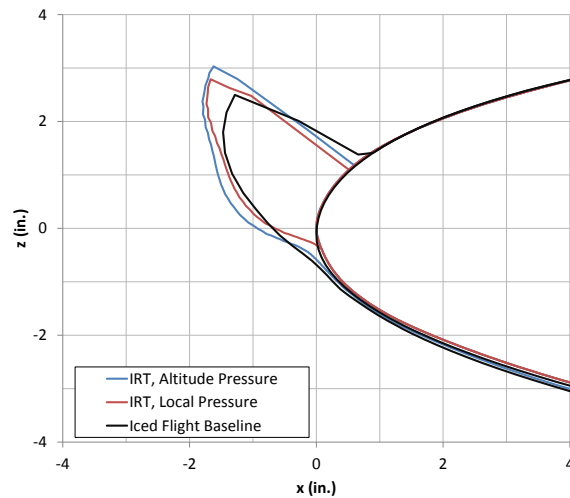
Figure 3.29: Comparison of Ice Shapes for Case WB33 T-4 in IRT at Local and Altitude Pressures

The impingement efficiency and heat transfer coefficient distributions corresponding to these ice shapes are shown in Figure 3.30. At altitude pressure, the peak impingement efficiency, β_{max}, on the IRT model is somewhat higher than that of the IFB while the heat transfer coefficient, h_c, is well matched. This results

in a larger horn due to the extra impinging water mass in the horn area of the upper surface of the model. The β_{max} value is likely larger due to the lower maximum thickness of the hybrid model as compared to the baseline airfoil, an effect proposed by Malone [46] that is discussed in Section 3.5 and isolated by running LEWICE3D at altitude pressure. For the IRT model at local pressure, the effects are reversed with a well matched β distribution but considerably higher h_c. This also leads to a larger horn on the IRT model than the IFB because more of the water that impinges on or runs past the horn is able to freeze due to the higher heat transfer. The increase in magnitude of the heat transfer is caused by the higher density of the air at the elevation of the IRT and is the most apparent effect of altitude. With the altitude pressure case matching IFB β better, but having larger h_c, and the local pressure case matching IFB h_c better, but having larger β, the ice shapes resulting from both IRT simulations are similar to one another and longer than the IFB.

(a) Impingement Efficiency   (b) Heat Transfer Coefficient
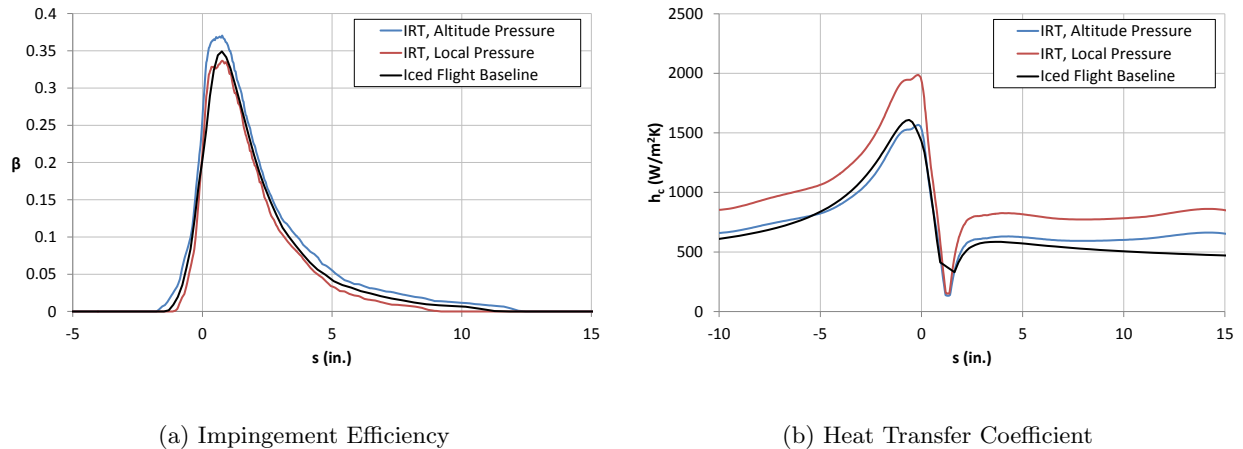
Figure 3.30: Comparison of β and h_c for Case WB33 T-4 in IRT at Local and Altitude Pressures

3.5   Icing Scaling

Case WB47 T-6, $\alpha = 4.36$ deg., $\delta = 16$ deg.

A flow simulation including viscous effects was run for the conditions of Case WB47 T-6 at the associated baseline angle of attack of $\alpha = 4.36$ deg. and a flap angle of $\delta = 16$ deg. in order to match the attachment line location of the CFB at the IRT centerline. It was assumed that the IRT test section velocity is limited to 250 knots (128.6 m/s) for this run so the baseline air speed was not matched. This results in an air speed of $V = 139.60$ m/s for the flight baseline and $V = 128.61$ m/s in the IRT test section. Figure 3.31 shows C_P contours with streamtraces on the model surface.

(a) Low Pressure Surface   (b) High Pressure Surface
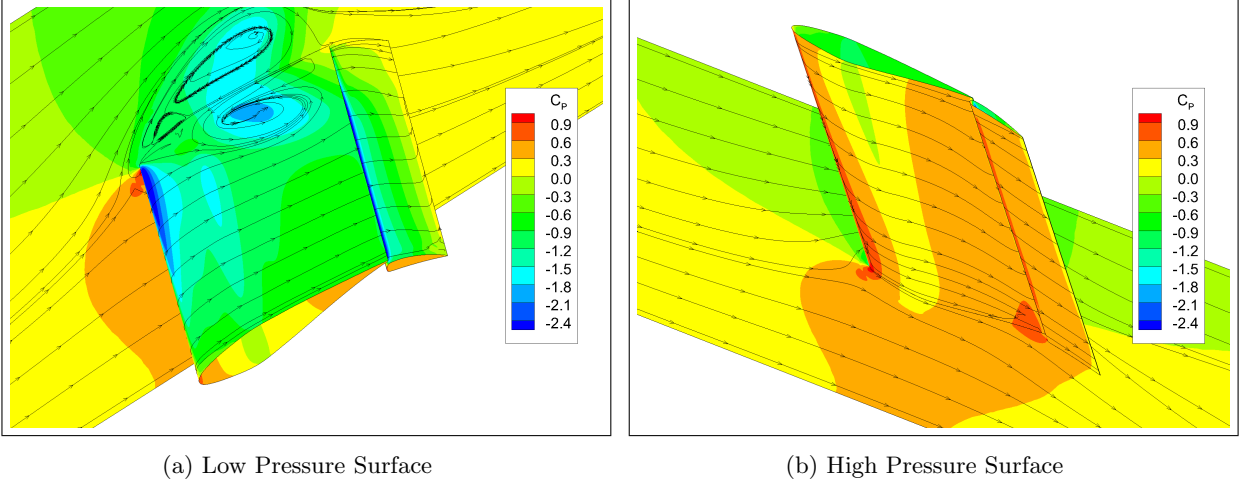
Figure 3.31: C_P Contour for Case WB47 T-6 at $\alpha = 4.36$ deg. and $\delta = 16$ deg.

A large separation bubble similar to previous results is present at the ceiling junction. This region is slightly larger due to the higher model loading that results from the higher α corresponding to Case WB47 compared to Case WB33. The flow was inspected in detail to ensure that no separation occurred in the region of interest for icing simulations. Figure 3.32 shows the attachment line position with the span of the model. The attachment line location from the CRM65 is well matched at the IRT centerline ($y = 0$).
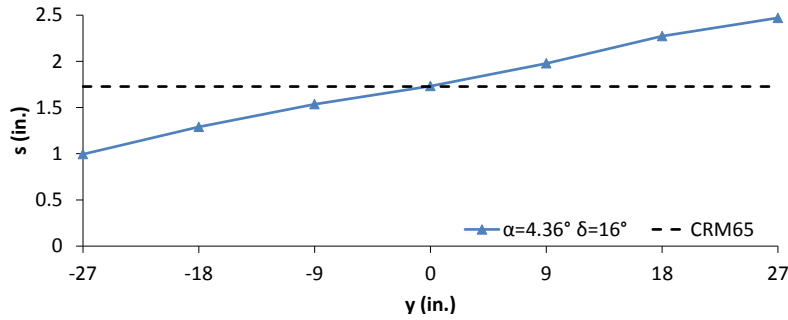
Figure 3.32: Spanwise Attachment Line Location for Case WB47 T-6 at $\alpha = 4.36$ deg. and $\delta = 16$ deg.

The method described in Section 2.4.4 and outlined in Appendix D was used to determine a set of icing conditions to investigate icing scaling. LEWICE3D was then used to generate ice accretions using both the unscaled baseline conditions and the scaled conditions. These conditions are given in Table 2.6 and corresponding ice shapes are compared to the IFB ice shape for Case WB47 T-6 in Figure 3.33.

Surprisingly, the IRT ice shape with the unscaled conditions matches the IFB ice shape better than with scaled conditions. To understand why this may be, consider the β and h_c distributions shown in Figure 3.34.
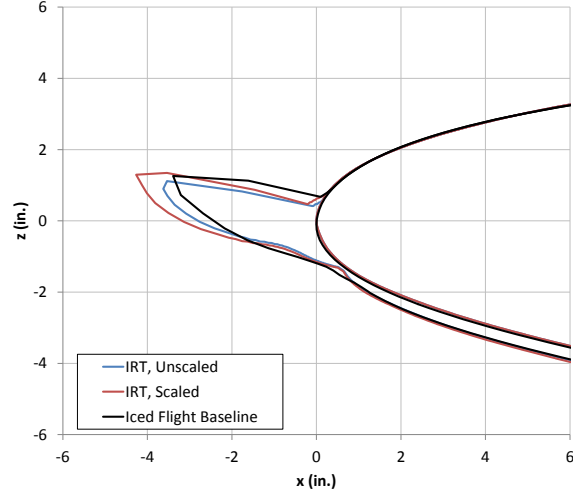
Figure 3.33: Comparison of Scaled and Unscaled Ice Shapes for Case WB47 T-6 in IRT (see Table 2.6)

(a) Impingement Efficiency

(b) Heat Transfer Coefficient
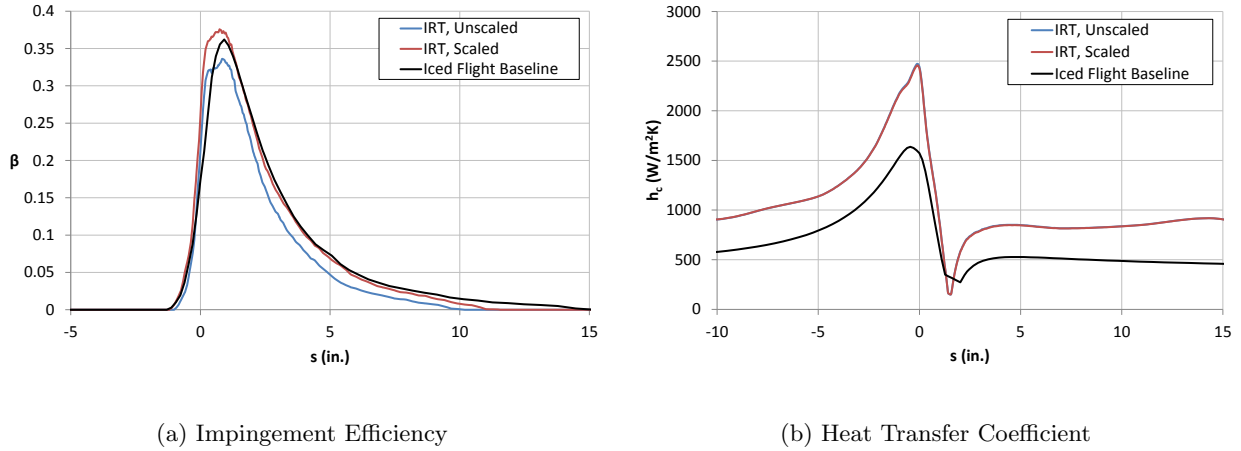
Figure 3.34: Comparison of β and h_c for Case WB47 T-6 in IRT for Scaled and Unscaled Icing Conditions

Comparing the impingement efficiency distributions in Figure 3.34a reveals that the droplet trajectory similitude, attempted by matching K_0, was largely successful. The β distribution from the scaled conditions matches well except for a slightly higher β from about $s = 0$ to 1 in. whereas the unscaled impingement efficiency is low throughout most of the leading-edge region. Careful examination of Figure 3.34b reveals that the scaled and unscaled case h_c distributions are exactly the same, the respective curves being coincident. Though equal, the h_c for the scaled and unscaled cases are significantly higher than that of the IFB. With a combined low β and high h_c distribution, the ice thickness of the unscaled shape approximately matches that of the IFB. The β of the scaled case matches that of the IFB well except for the overshoot from about $s = 0$ to 1 in. Nevertheless, the high h_c of the scaled case compared to that of the IFB results in ice that is thicker than the IFB, though the horn angle is perhaps matched better. This brings into question whether

76

an effort should be made to directly match h_c - as Bidwell [31] has done for simulations of a swept NACA 0012 in the IRT - rather than the more general matching of n_0 (see Equation (D.8)).

The heat transfer coefficient is higher in the IRT than in the IFB due to the higher air density at the lower altitude. While h_c is not matched directly in the scaling method used, it is taken into account in the matching of the freezing fraction at the stagnation plane, n_0, which is a function of h_c through the air energy transfer parameter and the relative heat factor (see Equations (D.8) through (D.11)). To match h_c directly would require that the test section velocity be scaled by the factor by which air densities are mismatched due to the dependence of Nu_a on Re_a (see Equations (D.13) and (D.14)). In the context of a large-scale, swept-wing model this is actually a favorable constraint because, given the higher density of air at the elevation of the IRT, the test section velocity would need to be lowered in order to match h_c. Due to blockage effects, it is often the case that the true air speed of the reference case can not be matched in the tunnel, requiring the tests to be performed at lower velocities anyway. Lowering the IRT test section velocity simultaneously reduces loading while allowing h_c to be matched directly, perhaps improving ice shape agreement. However, this precludes surface water dynamics similitude because, with reduced velocity and a full-scale leading edge, the Weber number of the scaled conditions will not match that of the reference case (see Equation (D.18)). This highlights the classic challenge of icing similitude; the scaling of icing conditions is limited to a small set of parameters over which the operator has control, namely MVD, LWC, τ, T, and perhaps V. Furthermore, there are often additional constraints on these parameters due to tunnel capabilities such as a limit on test section velocity due to blockage. This short list of variables over which the icing test designer has control limits the allowable number of dimensionless parameters that can practically be adjusted in the tunnel in order to scale the conditions for similitude with the reference case.

Despite the droplet trajectory similarity enforced by matching K_0, the β distribution for the scaled conditions is somewhat mismatched in the region from about $s = 0$ to 1 in. A similar trend was found in the ice shapes for Case WB33 T-4 shown in Figure 3.30a and WB47 T-6 shown in 3.28a, though in these cases no scaling was attempted. However, the higher impingement efficiency near β_{max} is likely due to the reduced thickness of the hybrid model as compared to the full-scale reference wing.

For a hybrid model, geometry similitude is achieved by retaining the full-scale geometry at the leading edge. However, for obvious reasons, the full-scale geometry can only be maintained over a small portion of the airfoil, up to the leading-edge extents. The leading-edge extents are generally selected based on the expected impingement limits. Beyond these points the leading-edge is blended with the redesigned aft section of the model. This results in the thickness of the reference airfoil not being maintained beyond the leading-edge

extents. This is clear in Figure 3.35 which shows the MS flapped-hybrid model and the full-scale, reference airfoil from which it was designed.
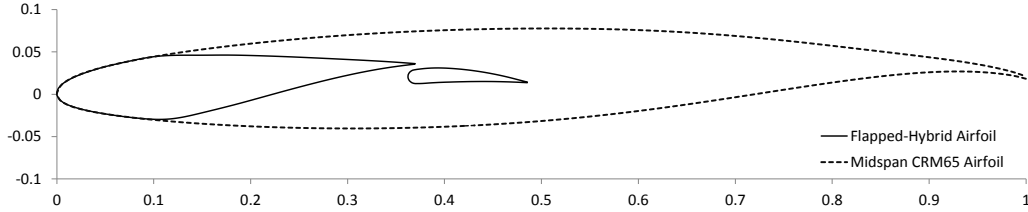
Figure 3.35: Comparison of the Midspan Station Flapped-Hybrid Airfoil to the Full-Scale CRM65 Airfoil, Shown in the Normal Direction

The maximum thickness of an airfoil has an important effect on icing, a topic discussed by Malone [46]. At subsonic velocities, flow upstream of an airfoil or wing is affected by its presence. Streamlines and droplet trajectories upstream of a thick geometry are influenced more than for a thinner body. Icing cloud droplets are consequently spread more thinly on the leading edge of the airfoil. For this reason, hybrid models often result in higher β_{max} than the reference geometry for the same conditions because the hybrid is substantially thinner than the reference geometry it represents. Such a trend was seen in the icing simulation results for Cases WB33 T-4, WB47 T-6, and WB71 T-6 (see Figures 3.30a, 3.34a, and 3.28a).

3.6   Spanwise Variation in Impingement and Ice Shape

Two flow simulations for Case WB33 T-4 have been shown which have attachment line locations at tunnel centerline matching that of the CFB at the same conditions. The first, discussed in Section 3.3.1, is at the CFB angle of attack, $\alpha = 3.67$ deg. and $\delta = 15$ deg. The second is at $\alpha = 5.50$ deg. and $\delta = 5$ deg. and was presented in Section 3.3.2. Figure 3.36 shows the attachment line position across the model span for these two simulations.

Matching the attachment line position at IRT centerline with a higher α and lower δ results in a lower attachment line slope or less variation in attachment line position across the span. This results from the fact that the main element of the hybrid model carries a larger portion of the load than the flap when a higher α and lower δ is used. When more of the circulation on the model is generated closer to the leading edge, its influence on the leading-edge flow characteristics increases and the same attachment line position is achieved at a lower lift coefficient. This was shown to be the case for hybrid airfoils by Fujiwara et al. [13]
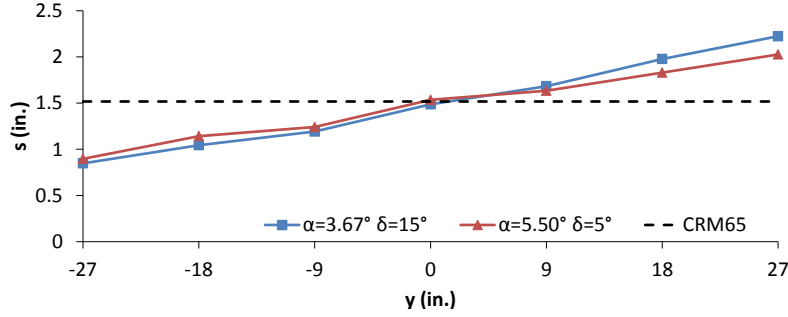
Figure 3.36: Spanwise Attachment Line Location for Case WB33 T-4

and seems to hold true for 3D hybrid models as well. The overall lift coefficient at $\alpha = 3.67$ deg. and $\delta = 15$ deg. is $C_L = 0.666$ whereas for $\alpha = 5.50$ deg. and $\delta = 5$ deg. it is reduced to $C_L = 0.549$. Because the circulation on the model is lower across the entire span, the effects of the tunnel floor and ceiling discussed in Section 3.1 are reduced, a fact that is apparent in the reduced slope of the attachment line position in Figure 3.36. Achieving the same attachment line position at a lower C_L reduces the model loading and may reduce ceiling junction separation because the local C_l value at the ceiling is reduced, though the change in C_L in the current comparison was not large enough to see this effect in the flowfields shown in Sections 3.3.1 and 3.3.2.

By looking at the ice shapes, β distributions, and h_c distributions across the span of the model, one can consider what effect the change in attachment line location due to the floor and ceiling of the IRT has on impingement and ice accretion. If the attachment line position has the first-order impact on these parameters that was assumed, a side-by-side comparison should show differences in them near the floor and ceiling because the attachment lines in Figure 3.36 are most different in these regions. Figure 3.37 shows the ice shapes across the entire span for each of the two IRT simulations. Recall that in the IRT reference frame described in Section 2.3.1, the root of the model and floor of the IRT correspond to $y = -36$ in. with the model tip and IRT ceiling at $y = +36$ in.

For both cases, the change in ice shape across the span is very pronounced. Just as the attachment line moves farther down the leading edge due to the increase in loading across the span, the horn angle of the ice shapes decreases across the span. The ice shapes also transition from short and wide at the floor of the IRT to long and thin at the ceiling. While the overall trend is the same for both simulations, the case with higher α and lower δ which resulted in a lower C_L and less spanwise variation in attachment line has less change in ice shape across the span, especially near the floor and ceiling where the difference in attachment lines in Figure 3.36 was more pronounced.

79
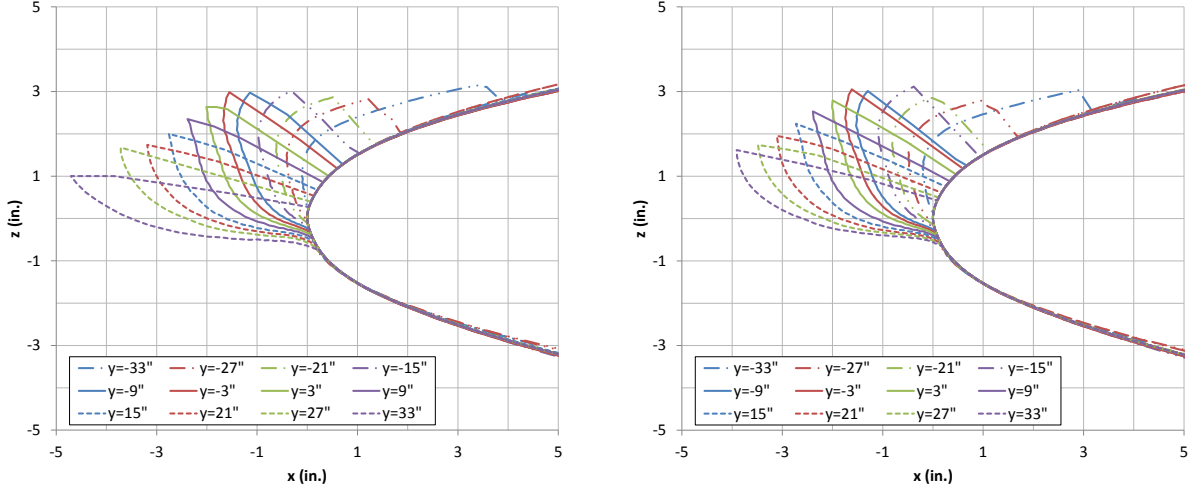
(a) $\alpha = 3.67$ deg. $\delta = 15$ deg.

(b) $\alpha = 5.50$ deg. $\delta = 5$ deg.

Figure 3.37: Comparison of Spanwise Ice Shape Variation for Case WB33 T-4

The β distributions across the span of the model are compared in Figure 3.38. The shift in β distribution to the right (farther down the leading edge) with span (toward tunnel ceiling) tracks the change in attachment line location. The β_{max} is greatest at the floor and decreases with span. Very little difference can be distinguished between the impingement efficiency distribution for the two simulations.
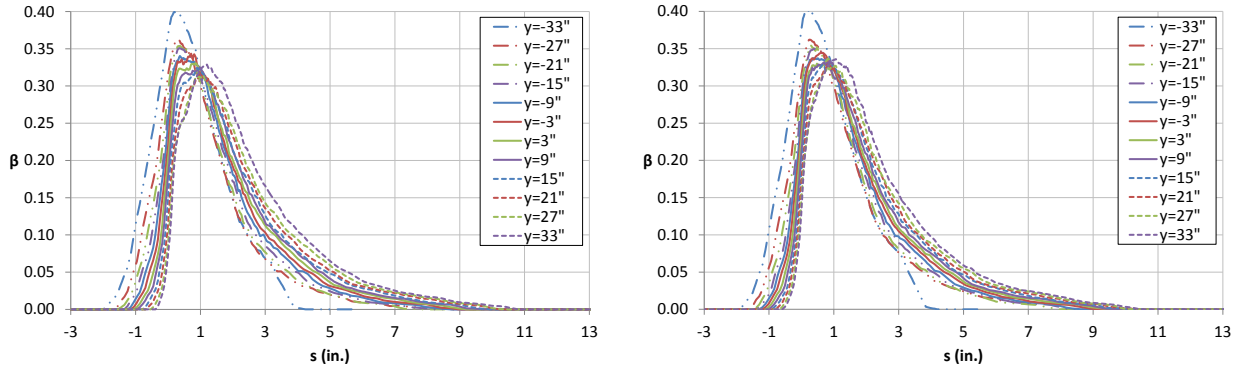
(a) $\alpha = 3.67$ deg. $\delta = 15$ deg.

(b) $\alpha = 5.50$ deg. $\delta = 5$ deg.

Figure 3.38: Comparison of Spanwise β Distribution Variation for Case WB33 T-4

The h_c distributions across the span of the model are compared in Figure 3.39. Again, the shift in the curves caused by the change in attachment line location with span is evident. The heat transfer tends to increase on the upper surface of the model with span, following the trend in suction peak observed in Section 3.1. Near the floor the h_c is considerably lower, allowing the water film layer to flow farther onto the

upper surface of the leading edge before freezing. This results in thinner ice shapes with larger bases near the floor. As h_c increases with span near the hilite, longer and more distinct horns begin to form until, near the ceiling, very long and thin ice shapes point upstream. Some differences in the peak h_c values can be seen between the two simulations which contributes to the differences in ice shape near the floor and ceiling.

(a) $\alpha = 3.67$ deg. $\delta = 15$ deg.

(b) $\alpha = 5.50$ deg. $\delta = 5$ deg.
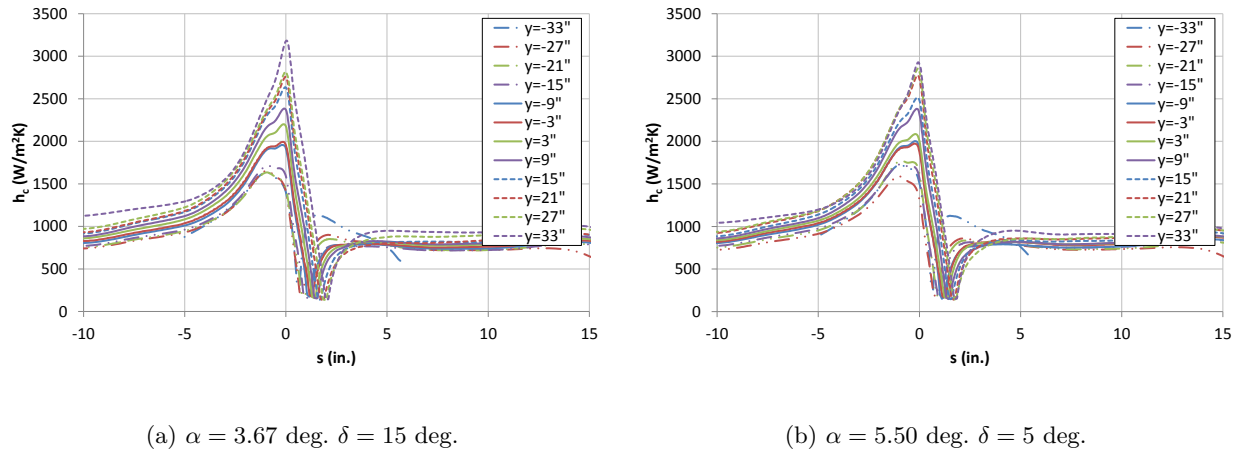
Figure 3.39: Comparison of Spanwise h_c Distribution Variation for Case WB33 T-4

Now that the trends of the ice shapes with span have been compared, it is instructive to isolate the results at the IRT centerline for a more direct comparison to answer the question of whether attachment line matching is sufficient for ice shape matching or if the angle of attack of the model leading edge must also match that of the reference wing. It was shown in Figure 3.36 that the attachment line positions for the two simulations, though different, each matched that of the MS station on the CFB quite closely at the IRT centerline ($y = 0$). The centerline C_P distributions for the two simulations are overlaid on that of the MS station of the CRM65 wing from the CFB in Figure 3.40.

Figure 3.40a shows that the C_P distributions on both IRT simulations are very similar near the leading edge with almost the same attachment line location and suction peak magnitude. The centerline C_P distributions from the IRT simulations also match that of the full-scale CRM65 from the CFB well in the leading-edge region except for a suction peak magnitude that is higher. The farther aft on the model, the more the C_P distributions from the IRT simulations begin to differ from each other. It is clear that at the higher α and lower δ, there is less area between the upper and lower C_P curves, suggesting a lower C_l value locally. The suction peak of the IRT simulations, though similar to one another, are about 0.22 higher than the suction peak on the CFB at the MS station, as seen in Figure 3.40b. The ice shapes at the IRT centerline resulting from these two simulations are shown in Figure 3.41.

(a) Full Distribution

(b) Suction Peak Region
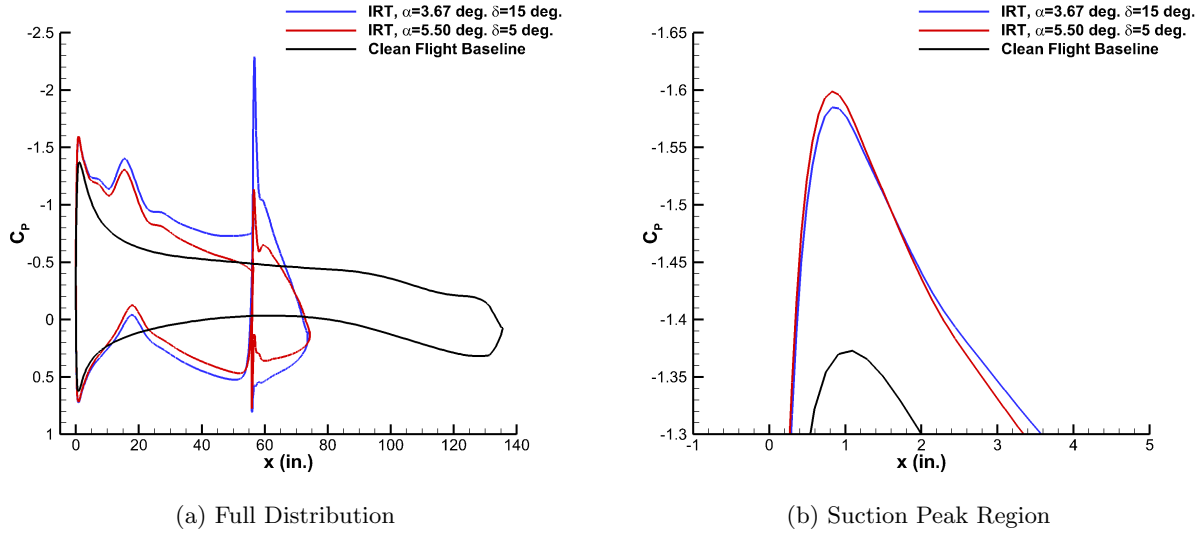
Figure 3.40: IRT Centerline C_P Distribution Comparison for Case WB33 T-4 Between IRT Model at $\alpha = 3.67$ deg., $\delta = 15$ deg. and $\alpha = 5.50$ deg., $\delta = 5$ deg.

Despite the model being at two different angles of attack, the ice shapes are very similar. Comparing the centerline attachment line locations in Tables 3.3 and 3.4 reveals that there is a difference of 0.05 in. (1.3 mm), which, though small, may account for the small difference in ice shape. The fact that the ice shapes agree so well suggests that, despite the difference in the global angle of incidence at which the impinging droplets approach the model, local flow characteristics dominate and that matching the attachment line location is sufficient for matching ice shapes, even at an α not equal to the baseline value. The difference between the two IRT ice shapes is far less significant than the difference of either as compared to the IFB.
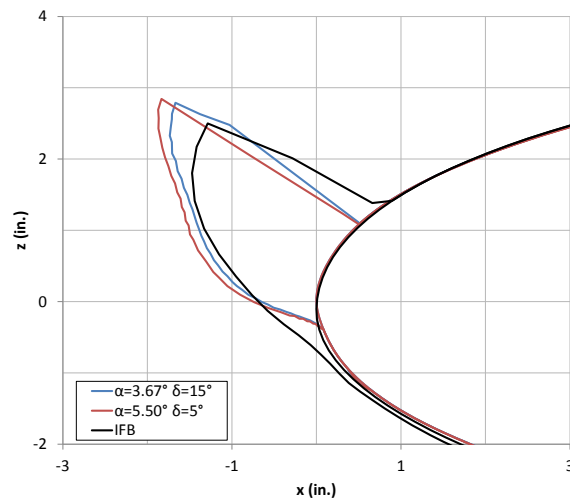
Figure 3.41: Comparison of Centerline Ice Shapes for Case WB33 T-4 in IRT at Two α-δ Settings

Thus, if there is a difference caused by operating the model at an α not matching the baseline, it seems to introduce much less error than trying to replicate full-scale ice shapes in the IRT.

The centerline β and h_c distributions for these two simulations are shown in Figure 3.42. The IRT β distributions are virtually indistinguishable and also match that of the IFB well. As was discussed in Section 3.4, the h_c in the IRT simulations is somewhat higher than the baseline due to the higher density at IRT elevation. The h_c distributions from the two IRT simulations match well with a small difference in the peak value just above the hilite which can be attributed to the slightly higher suction peak of the $\alpha = 5.50$ deg. case shown in Figure 3.40. Again, the small difference in the suction peak value results from the attachment line being 0.05 in. (1.3 mm) lower on the leading edge for the $\alpha = 5.50$ deg. case (see Tables 3.3 and 3.4).

(a) Impingement Efficiency

(b) Heat Transfer Coefficient
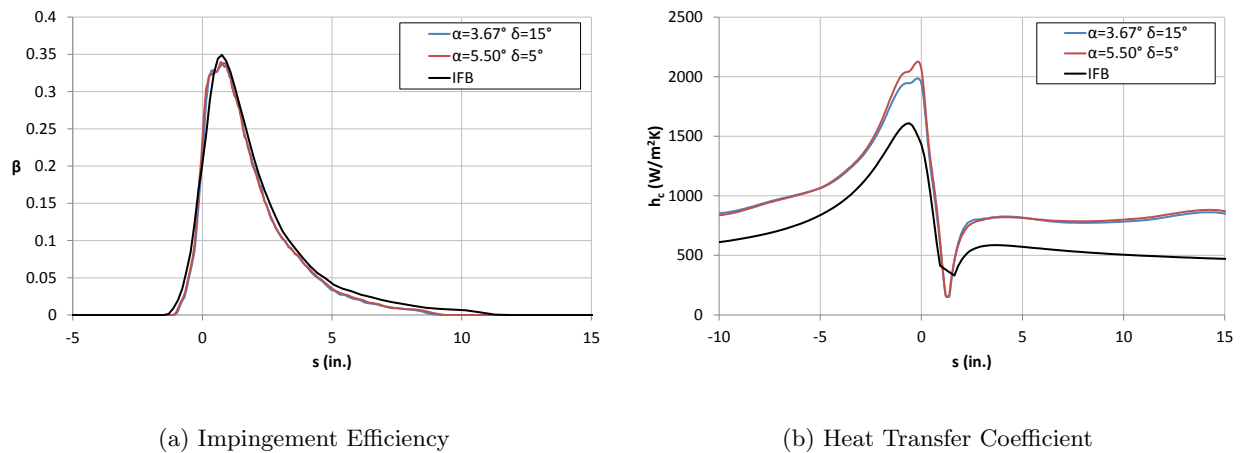
Figure 3.42: Comparison of Centerline β and h_c for Case WB33 T-4 in IRT at Two α-δ Settings

That ice shapes can be matched simply by matching attachment line locations and not requiring that the full-scale leading edge of the model be at the same geometric angle of attack as the baseline case has important implications for model designers. Removing the constraint on the α at which a model must be tested makes it possible to design a model without a flap that can still be used over a range of test conditions with attachment line position being set by the angle of attack. A model without a flap is simpler and less expensive to fabricate. It also requires a less aggressive main element design for the same SF, reducing the risk of flow separation due to adverse pressure gradients on the aft section. For a flapped-hybrid design, it is possible to lower the overall C_L when tunnel test section velocities are limited by loading on turntables or balances. This is done by using an α-δ setting that loads the model more toward the leading edge, increasing the circulation's influence in the leading-edge region and reducing the total circulation required to reach the

same attachment line position. This has the added benefit of reducing the variation in attachment line position with span and lowering the C_l near the ceiling which may reduce separation.

It should be noted that the difference in the angles of attack used in the two cases discussed in this section was only moderate. There may be second-order effects that become significant if the α at which a test is conducted varies from the baseline α by a larger amount. Further simulations would be of great value in establishing the level of fidelity with which ice shapes can be matched at off-case angles of attack. Furthermore, one would expect that for sufficiently large MVD (in the limit as $K_0 \rightarrow \infty$), the ability to match ice shape at off-case α would diminish. Matching ice shapes at an α other than the baseline requires that the local flow in the vicinity of the leading edge is able to dominate the flowfield effects on droplet trajectories. Because larger droplets have greater inertia, the local flow at the leading edge will be less able to redirect the droplets in the icing cloud as MVD is increased. Again, more research is needed to understand how large MVD can become before the global angle of incidence must be matched in order to obtain ice shapes representative of the baseline wing for swept-wing models. For this reason, these results should not be generalized to large droplet sizes until further research is conducted. Furthermore, computational simulations alone are not sufficient for fully understanding this limit because LEWICE3D does not currently have the capability to model the icing physics which are fundamental to scalloped ice formation, requiring icing tunnel tests to show that 3D effects are sufficiently matched when attachment line is matched.

Chapter 4

Summary, Conclusions, and Recommendations

Summary

The research in this thesis was conducted at the University of Illinois at Urbana-Champaign as part of Phase III of the Large-Scale, Swept-Wing Ice Accretion Project [14]. Swept-wing models were created using 2D flapped-hybrid design methods [13] and simple sweep theory [37] to represent three stations on the 65% scaled Common Research Model (CRM65) [15]. The flapped-hybrid model at the $\eta = 64\%$ station, called the midspan (MS) station, was used in this thesis to perform 3D CFD calculations in Fluent with and without viscosity considered. Inviscid solutions were used to better understand the fundamental characteristics of flow over a swept-wing model spanning the IRT from floor to ceiling. These investigations included the use of the Euler equations in Fluent to simulate the MS model in the IRT and the vortex lattice method in XFLR5 to consider load distributions on finite, swept wings and swept models between sidewalls in Section 3.1. Several methods of compensating for the effects of sidewalls were explored using inviscid IRT simulations with results in Section 3.2. Viscous solutions were then produced using the Reynolds Averaged Navier-Stokes (RANS) equations in Fluent. These solutions were used as input flowfields to the grid based ice accretion code LEWICE3D [24]. Droplet trajectory and ice accretion simulations were performed in LEWICE3D and compared to the Iced Flight Baseline (IFB) ice shapes which were produced on the CRM65 wing in free air simulations by Boeing using OVERFLOW and LEWICE3D [26] and revised by the author using the latest version of LEWICE3D, described in Section 2.1.3. The critical icing scenarios identified by Boeing provided the set of flight and icing conditions set forth in Table A.1. The resulting icing simulations were used to explore the effect of attachment line position in Section 3.3, altitude in Section 3.4, icing scaling in Section 3.5, and the spanwise variation of ice shapes in Section 3.6.

Conclusions

- The attachment line location on the leading edge of a swept-wing, flapped-hybrid model has a first-order impact on ice shape, analogous to the first-order impact of stagnation point location on the ice shape on a hybrid airfoil shown by Fujiwara et al. [13]. The suction peak has a second-order effect, impacting the heat transfer coefficient. Because the attachment line has a first-order impact on ice shape, when the attachment line position is matched for a given case, a good ice shape match can be expected. This makes it the most important metric in early model design. When the attachment line location is matched, the suction peak will generally also be comparable, depending on the geometry.

- The loading on a swept model between sidewalls increases considerably with span due to the increase in effective angle of attack that results from the induced upwash caused by stations farther inboard and amplified by the wall symmetry conditions. This spanwise increase in loading causes the attachment line to move farther down the leading edge at stations farther outboard.

- Changing the angle of attack or flap angle are equivalent methods of adjusting attachment line location uniformly over the span.

- Using segmented flaps, local flap angles can be varied in order to change the attachment line position at local stations. Segmented flaps are not effective in significantly changing the spanwise distribution of load and attachment line position for models with aspect ratio near unity. Increasing the AR of a model simultaneously reduces the spanwise variation in C_l and attachment line position caused by sidewalls while increasing the effectiveness of segmented flaps. Because the purpose of this research is to look at large-scale wing models, increasing the aspect ratio of the model is not a practical solution.

- Using model twist, the local angle of attack of the model can be varied in order to change the attachment line location at local stations. Twist is effective in changing the spanwise load distribution by reducing the effective angle of attack across the span of the model, compensating for the increasing upwash across the model. Whether the additional complexity of the model is justified depends on the requirements of the icing tests to be conducted.

- Because LEWICE3D uses edge velocity to determine the attachment line position, *a posteriori* confirmation of attachment line agreement is required by the user if $C_{P,max}$ was used to determine the flow solution's attachment line location.

- Within the limits of the α and MVD ranges of this research, reaching the same attachment line location using different α-δ pairs will result in very similar ice shapes, implying that icing tunnel tests do not

necessarily have to be conducted at the angle of attack of the reference case. A flap can be removed and angle of attack used to adjust attachment line location, reducing the required SF of the main element of the hybrid for a given chord length.

- Increasing α while decreasing δ allows the same attachment line location to be achieved at a lower C_L because the circulation on the model is generated closer to the leading edge, influencing the flow in the region of interest more. In addition to reducing loads on tunnel turntables and balances, the spanwise variation in attachment line position is reduced at lower C_L values, reducing the spanwise variation in ice shape and potentially reducing ceiling junction separation in the IRT.

- The most significant effect of altitude on ice shape is that the higher density at the low elevations of icing wind tunnels results in higher heat transfer coefficients compared to icing conditions at departure, cruise, or approach altitudes. If the impingement efficiency is well matched, this can result in thicker ice in glaze ice tunnel tests.

- Droplet trajectory similitude resulted in improved impingement efficiency distribution matching while the overall ice shape did not improve using the scaling method of Appendix D. The results suggest that directly matching h_c may improve ice shape agreement for the conditions of this research.

- Though hybrid models with full-scale leading edges are generally considered to maintain geometric similitude, they do not maintain the same thickness as the reference geometry. The lower maximum thickness of hybrid models results in an increase in β_{max} because streamlines and droplet trajectories upstream of the model are influenced less, reducing the spread of the droplets that impinge on the leading edge.

- The MS flapped-hybrid model is effective in generating ice shapes representative of the IFB when the attachment line location at IRT centerline is matched to that of the CFB. Simulations indicate horn ice shapes in the IRT tend to be longer than those generated on the CRM65 in free air, attributed to a higher β_{max} due to reduced maximum thickness, a higher h_c due to altitude effects, or both.

Recommendations

- A parametric study of ice shapes generated by matching attachment line positions over a range of α for different MVD is recommended. Comparing these ice shapes will identify the α range for a given drop size over which comparable ice shapes are generated. Such an understanding will remove the constraint on angle of attack from model designers and icing tunnel operators, potentially reducing model cost and complexity and enabling more freedom during test campaigns. After any limitations on α and MVD are determined computationally, the applicability should be investigated experimentally to show that 3D ice shape features such as scallops are also properly matched at off-case angles of attack.

- LEWICE3D does not currently have the capability to model the highly 3D physics of ice accretions which are present on scalloped ice shapes. The current research assumes that a 1 ft. portion of span at the IRT centerline is sufficient for capturing 3D features of ice shapes with complete scallops. Under this assumption, the spanwise variation in horn angle and ice shape caused by the changing attachment line position over the region of interest may be considered acceptable, eliminating the need for a twisted model. However, if it is found that a larger spanwise width is required to properly represent the 3D features of glaze ice shapes on a swept wing, spanwise load control techniques may need to be employed. Therefore, it is recommended that actual IRT tests are conducted so that the characteristic spanwise length over which quality ice accretions must be documented to properly capture these ice shape features can be identified. Such experiments will also improve the understanding of scalloped ice shape formations, making it possible to expand the capabilities of LEWICE3D and other icing codes to better simulate 3D ice shapes.

- Further similitude studies are recommended. The question of which similitude parameters should be matched to best replicate flight baseline ice shapes using the swept-hybrid model is yet to be answered. This is further complicated by the fact that current numerical icing tools cannot fully capture the 3D icing physics inherent to the problem, implying that similitude validation will of necessity be delayed until icing experiments have been conducted.

Appendix A

Additional Tables and Figures

Table A.1: Boeing Case Identifiers and Associated Flight and Icing Conditions [26]

Cond.	Phase	Weight	Flaps	HP (ft.)	P_{amb} (kPa)	T_{amb} (K)	M	TAS (m/s)	α (deg.)	LWC (g/m^3)	MVD (μm)	τ (min.)	TWE (g/m^2)
25	Climb	Nominal	Up	30,000	30.124	233.15	0.81	249.26	1.68	0.2000	20	0.32	963
33	Hold	LGW	Up	10,000	69.702	269.15	0.36	119.41	3.67	0.5510	20	45.0	177,641
33	Hold	LGW	Up	10,000	69.702	267.15	0.36	118.96	3.67	0.5090	20	45.0	163,490
33	Hold	LGW	Up	10,000	69.702	260.15	0.36	117.39	3.67	0.3605	20	45.0	114,265
33	Hold	LGW	Up	10,000	69.702	248.15	0.36	114.65	3.67	0.1750	20	45.0	54,174
39	Hold	LGW	Up	22,000	42.824	253.15	0.46	146.36	3.64	0.2100	20	45.0	82,984
39	Hold	LGW	Up	22,000	42.824	248.15	0.46	144.90	3.64	0.1750	20	45.0	68,467
39	Hold	LGW	Up	22,000	42.824	243.15	0.46	143.44	3.64	0.1400	20	45.0	54,219
41	Hold	HGW	Up	5,000	84.319	267.15	0.35	115.78	4.38	0.5090	20	45.0	159,122
41	Hold	HGW	Up	5,000	84.319	260.15	0.35	114.26	4.38	0.3605	20	45.0	111,212
41	Hold	HGW	Up	5,000	84.319	248.15	0.35	111.59	4.38	0.1750	20	45.0	52,727
47	Hold	HGW	Up	15,000	57.209	267.15	0.43	139.60	4.36	0.5090	20	45.0	191,856
47	Hold	HGW	Up	15,000	57.209	260.15	0.43	137.76	4.36	0.3605	20	45.0	134,090
47	Hold	HGW	Up	15,000	57.209	248.15	0.43	134.55	4.36	0.1750	20	45.0	63,573
71	ETOPS Hold	Nominal	-	1,500	95.956	267.15	0.32	104.51	4.40	0.5090	20	15.0	47,878
71	ETOPS Hold	Nominal	-	1,500	95.956	260.15	0.32	103.14	4.40	0.3605	20	15.0	33,462
71	ETOPS Hold	Nominal	-	1,500	95.956	248.15	0.32	100.73	4.40	0.1750	20	15.0	15,865

Note: Case 25 values of LWC, MVD, τ, and TWE are intermittent maximum atmospheric icing conditions. The remaining cases are continuous maximum atmospheric icing conditions.
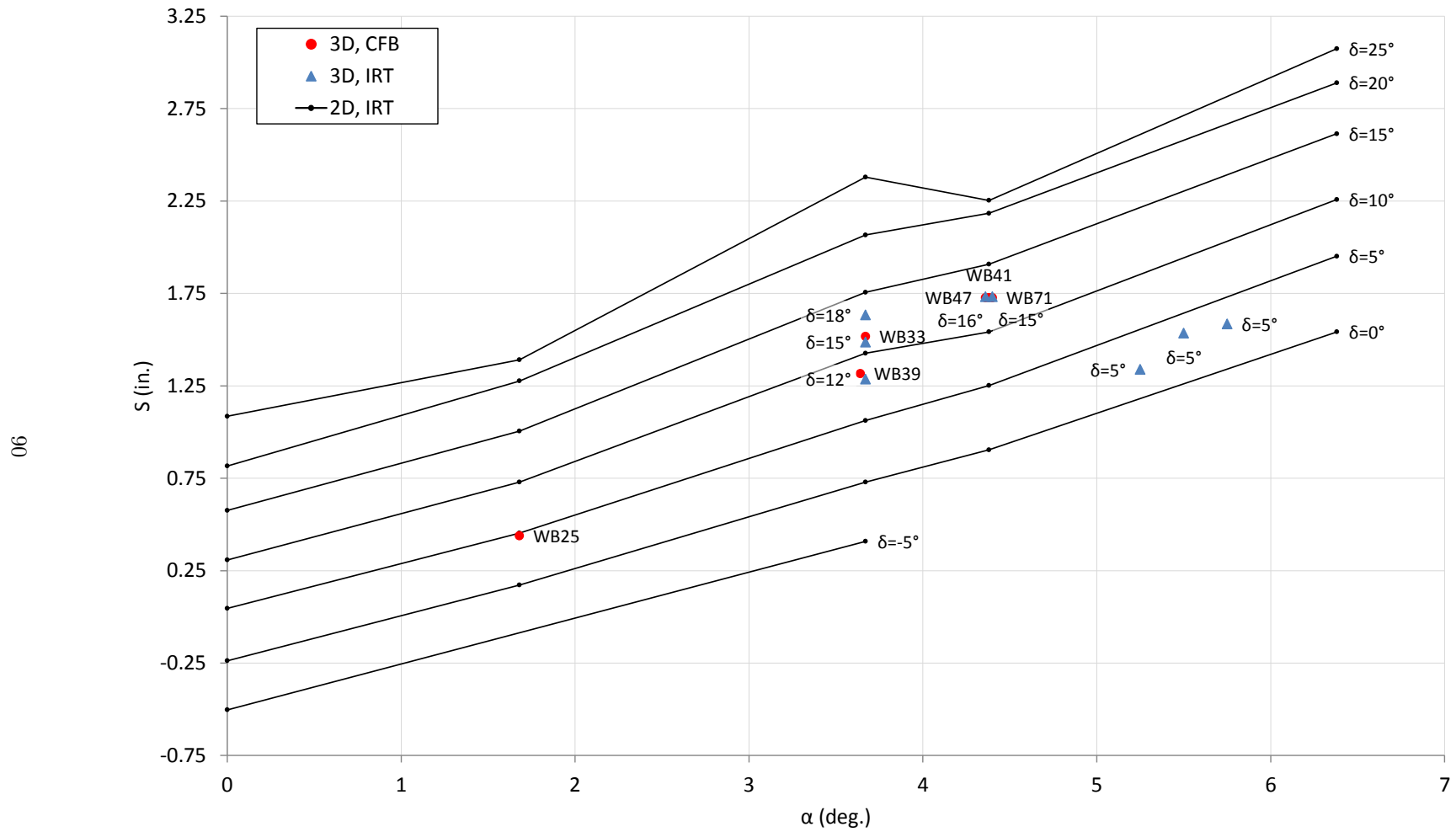
Figure A.1: Midspan Station 3D Aerodynamic Calibration Plot

Appendix B

Impingement Efficiency and Sweep Theory

Two-dimensional impingement efficiency, β_{2D}, is defined as the ratio of the vertical distance over which a given set of droplets are dispersed in the freestream, Δz_0, to the arc length over which the same droplets impinge on the airfoil surface, Δs. The three-dimensional impingement efficiency for an unswept wing has a similar definition except that it becomes a ratio of areas where Δy_o is the horizontal dispersion width of the freestream and Δb is the dispersion width at the surface. These definitions yield the following expressions:

$$\beta_{2D} = \frac{\Delta z_0}{\Delta s} \tag{B.1}$$

$$\beta_{3D} = \frac{\Delta z_0 \Delta y_0}{\Delta s \Delta b} \tag{B.2}$$

For the infinite swept wing of Figure B.1, the width of area of the impingement of the droplets on the surface of the wing is now $\Delta y'$ due to the sweep, Λ, which is measured in the manner consistent with simple sweep theory [37]. Expressing this in terms of the original coordinate axes with $\Delta y' = \Delta y / \cos \Lambda$ gives the following relationship for the 3D impingement efficiency of a swept wing:

$$\beta_{3D} = \frac{\Delta z_0 \Delta y_0}{\Delta s \Delta y'} = \frac{\Delta z_0 \Delta y_0 \cos \Lambda}{\Delta s \Delta y} \tag{B.3}$$

Substituting Equation (B.1) into Equation (B.3) gives a relationship between the impingement efficiency of a 3D swept wing and a 2D normal cut.

$$\beta_{3D} = \beta_{2D} \frac{\Delta y_0}{\Delta y} \cos \Lambda \tag{B.4}$$
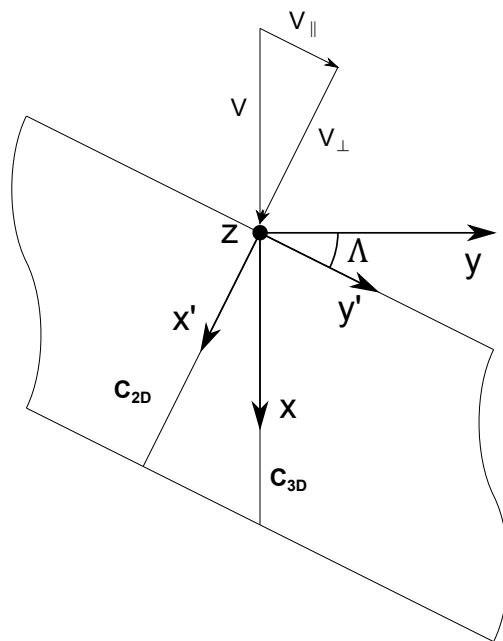
Figure B.1: Important Parameters on an Infinite Swept Wing, Adapted From McLean [37]

Appendix C

Midspan Station Airfoil and Flap Coordinates

The following coordinates are for the 2D flapped-hybrid airfoil design used as the basis for the 3D model. Coordinates are given in the plane normal to the leading edge, nondimensionalized by the full-scale CRM65 chord, $c_{\perp,fs} = 122.72$ in. (3.12 m), at $\alpha_\perp = 0$ deg. and $\delta = 0$ deg.

Midspan Hybrid Main Element	
x	y
0.369647	0.036164
0.365794	0.036519
0.361940	0.036865
0.358086	0.037198
0.354230	0.037518
0.350373	0.037827
0.346515	0.038125
0.342657	0.038412
0.338798	0.038689
0.334938	0.038958
0.331078	0.039218
0.327216	0.039470
0.323355	0.039715
0.319493	0.039955
0.315630	0.040188
0.311767	0.040417
0.307904	0.040641
0.304041	0.040862
0.300177	0.041080
0.296313	0.041296
0.292450	0.041510
0.288586	0.041724
0.284722	0.041937
0.280858	0.042149
0.276995	0.042360
0.273131	0.042569
0.269267	0.042777
0.265403	0.042982
0.261539	0.043185
0.257674	0.043384
0.253810	0.043581
0.249945	0.043773
0.246081	0.043962
0.242215	0.044146
0.238350	0.044326
0.234484	0.044500
0.230618	0.044669
0.226752	0.044833
0.222886	0.044991
0.219019	0.045143
0.215152	0.045290
0.211285	0.045431
0.207417	0.045566
0.203550	0.045696
$\vdots$	$\vdots$

x	y
0.199682	0.045818
0.195814	0.045932
0.191946	0.046035
0.188079	0.046124
0.184212	0.046197
0.180345	0.046251
0.176478	0.046285
0.172612	0.046296
0.168746	0.046288
0.164880	0.046265
0.161012	0.046233
0.157143	0.046199
0.153272	0.046168
0.149397	0.046144
0.145519	0.046135
0.141637	0.046140
0.137754	0.046149
0.133870	0.046152
0.129986	0.046140
0.126105	0.046102
0.122228	0.046027
0.118356	0.045906
0.114490	0.045729
0.110633	0.045484
0.106786	0.045163
0.102949	0.044754
0.099125	0.044248
0.095314	0.043639
0.091515	0.042939
0.087727	0.042163
0.083948	0.041324
0.080176	0.040437
0.076409	0.039516
0.072647	0.038576
0.068886	0.037631
0.065128	0.036688
0.061375	0.035735
0.057631	0.034759
0.053897	0.033748
0.050179	0.032686
0.046479	0.031563
0.042799	0.030376
0.039138	0.029123
0.035499	0.027804
0.031880	0.026420
0.028284	0.024970
0.024714	0.023451
$\vdots$	$\vdots$

x	y
0.021184	0.021843
0.017715	0.020123
0.014328	0.018265
0.011045	0.016240
0.007897	0.013977
0.004990	0.011388
0.002543	0.008395
0.000769	0.004952
0.000000	0.000000
0.000803	-0.002596
0.002712	-0.005974
0.005402	-0.008775
0.008577	-0.011029
0.012000	-0.012841
0.015575	-0.014342
0.019222	-0.015666
0.022904	-0.016876
0.026615	-0.017983
0.030351	-0.019000
0.034109	-0.019936
0.037884	-0.020803
0.041672	-0.021611
0.045469	-0.022372
0.049272	-0.023096
0.053077	-0.023791
0.056885	-0.024457
0.060697	-0.025094
0.064514	-0.025700
0.068337	-0.026277
0.072168	-0.026822
0.076006	-0.027335
0.079853	-0.027817
0.083709	-0.028266
0.087576	-0.028679
0.091449	-0.029043
0.095327	-0.029342
0.099205	-0.029563
0.103081	-0.029691
0.106951	-0.029710
0.110812	-0.029607
0.114662	-0.029366
0.118497	-0.028976
0.122317	-0.028444
0.126123	-0.027786
0.129916	-0.027022
0.133698	-0.026169
0.137470	-0.025244
$\vdots$	$\vdots$

x	y
0.141232	-0.024265
0.144986	-0.023250
0.148733	-0.022217
0.152474	-0.021181
0.156209	-0.020142
0.159939	-0.019100
0.163664	-0.018052
0.167384	-0.016998
0.171100	-0.015936
0.174812	-0.014863
0.178520	-0.013779
0.182225	-0.012682
0.185926	-0.011570
0.189625	-0.010443
0.193321	-0.009303
0.197015	-0.008151
0.200707	-0.006991
0.204398	-0.005824
0.208088	-0.004652
0.211778	-0.003479
0.215468	-0.002306
0.219158	-0.001134
0.222848	0.000034
0.226540	0.001199
0.230232	0.002360
0.233925	0.003517
0.237620	0.004667
0.241317	0.005812
0.245016	0.006949
0.248716	0.008079
0.252419	0.009200
0.256125	0.010313
0.259833	0.011415
0.263545	0.012507
0.267260	0.013587
0.270978	0.014656
0.274700	0.015712
0.278426	0.016754
0.282155	0.017782
0.285889	0.018795
0.289628	0.019793
0.293371	0.020774
0.297118	0.021738
0.300871	0.022684
0.304629	0.023611
0.308392	0.024518
0.312160	0.025404
$\vdots$	$\vdots$

x	y
0.315933	0.026267
0.319712	0.027107
0.323495	0.027921
0.327284	0.028710
0.331078	0.029470
0.334877	0.030202
0.338682	0.030904
0.342491	0.031574
0.346306	0.032216
0.350125	0.032831
0.353949	0.033422
0.357776	0.033992
0.361608	0.034542
0.365443	0.035066
0.369285	0.035538

Midspan Hybrid Flap Element

x	y
0.485500	0.014389
0.485000	0.014509
0.483800	0.014821
0.481900	0.015380
0.479300	0.016169
0.475900	0.017158
0.471800	0.018396
0.467100	0.019760
0.461800	0.021204
0.455900	0.022687
0.449500	0.024162
0.442800	0.025590
0.435600	0.026925
0.428200	0.028130
0.420600	0.029171
0.412900	0.030016
0.405200	0.030641
0.397500	0.031023
0.389900	0.031058
0.382400	0.030683
0.375400	0.029923
0.368800	0.028821
0.365800	0.027612
0.363300	0.024877
0.362300	0.021340
0.362900	0.017701
0.365000	0.014680
0.368200	0.012877
⋮	⋮

x	y
0.371900	0.012647
0.377300	0.012759
0.383800	0.013288
0.390600	0.013754
0.397600	0.014111
0.405000	0.014384
0.412400	0.014634
0.419900	0.014841
0.427300	0.014989
0.434600	0.015072
0.441700	0.015086
0.448500	0.015037
0.454900	0.014932
0.460800	0.014781
0.466300	0.014602
0.471100	0.014408
0.475400	0.014213
0.478900	0.014034
0.481700	0.013882
0.483700	0.013764
0.484900	0.013691
0.485400	0.013666

Flap Pivot

x	y
0.371000	0.020700

Appendix D

Similarity Parameters for Icing Scaling

The parameters which are matched for icing similarity studies are summarized below. Not all of the nomenclature used in these expressions is consistent with that used throughout the body of the thesis. Therefore, the meaning of any variables which depart from the definitions found in the nomenclature section are clearly stated. Equations of this appendix are adapted from Tsao and Lee [43] and Anderson [7] according to the basic scaling method set forth by Ruff [47].

Matching the modified inertia parameter maintains droplet trajectory similarity. The modified inertia parameter is given by

$$K_0 = \frac{1}{8} + \frac{\lambda}{\lambda_{\text{Stokes}}} \left(K - \frac{1}{8} \right) \tag{D.1}$$

where $K > 1/8$ is the inertia parameter given by

$$K = \frac{\rho_w \delta^2 V}{18 d \mu_a} \tag{D.2}$$

with ρ_w, μ_a, and d being the density of water, dynamic viscosity of air, and the leading-edge diameter, respectively. The leading-edge diameter is simply twice the radius of curvature of the airfoil at the leading edge. Here, δ is short for the MVD of the water droplets. Note the alternative form of Equation (D.1) used by Bragg et al. [48], $K_0 = K(\lambda/\lambda_{\text{Stokes}})$. The ratio $\lambda/\lambda_{\text{Stokes}}$ here and in Equation (D.1) is the droplet range parameter given by

$$\frac{\lambda}{\lambda_{\text{Stokes}}} = \frac{1}{(0.8388 + 0.001483 Re_\delta + 0.1847\sqrt{Re_\delta})} \tag{D.3}$$

where Re_δ is the Reynolds number based on MVD expressed as

$$Re_\delta = \frac{V \delta \rho_a}{\mu_a} \tag{D.4}$$

These equations apply to airfoils so their use on a swept wing requires care. The impingement efficiency at the stagnation point, β_0, is used to correlate 2D and 3D K_0 using the sweep angle, Λ. K_0 and β_0 have a one-to-one correspondence according to the relation

$$\beta_0 = \frac{1.40 \left(K_0 - \frac{1}{8}\right)^{0.84}}{1 + 1.40 \left(K_0 - \frac{1}{8}\right)^{0.84}} \tag{D.5}$$

The attachment line impingement efficiency on a swept wing, $\beta_{0,3D}$, relates to the stagnation point impingement efficiency on an airfoil or straight wing, $\beta_{0,2D}$, according to the equation given by Tsao and Lee [43] as

$$\beta_{0,3D} = \beta_{0,2D} \cos(\Lambda) \tag{D.6}$$

Therefore, matching K_0 is sufficient for droplet trajectory similarity on a swept-wing model when the model sweep angle matches that of the reference wing. The MS hybrid model has a sweep angle equal to the leading-edge sweep of the CRM65 wing so that only K_0 needs to be matched. However, an accurate value of β_0 will be needed for use in Equation (D.11) later.

The accumulation parameter, first defined by Bragg et al. [48], is matched in order to account for water catch. It is defined as

$$A_c = \frac{LWC \cdot V \cdot \tau}{d \cdot \rho_i} \tag{D.7}$$

where τ is the icing exposure time and ρ_i is the density of ice. Matching A_c alone is only sufficient when the water that impinges on the surface freezes on impact. In this case, the freezing fraction, which measures the portion of impinging water which freezes, is 100%. In the case of glaze icing conditions, the freezing fraction at the stagnation point is also matched to ensure surface energy similarity. The stagnation point freezing fraction is defined as

$$n_0 = \frac{c_{p,ws}}{\Lambda_f} \left(\phi + \frac{\theta}{b}\right) \tag{D.8}$$

where $c_{p,ws}$ is the constant pressure specific heat of water on the model surface, Λ_f is the latent heat of fusion, ϕ is the droplet energy transfer parameter, θ is the air energy transfer parameter, and b is the relative heat factor. The variables ϕ and θ have units of temperature.

The droplet energy transfer parameter is defined as

$$\phi = t_f - t_{st} - \frac{V^2}{2c_{p,ws}} \tag{D.9}$$

where t_f is the temperature of water at its freezing point and t_{st} is the static temperature.

The air energy transfer parameter is defined in its incompressible form as

$$\theta = \left(t_s - t_{st} - \frac{V^2}{2c_{p,a}} \right) + \frac{h_G}{h_c} \left(\frac{p_{ww} - p_w}{p_{st}} \right) \Lambda_v \tag{D.10}$$

where t_s is temperature at the surface of the model, h_G is the gas phase mass transfer coefficient, h_c is the familiar convective heat transfer coefficient, p_{ww} is the vapor pressure of water over liquid water, p_w is the vapor pressure of water in the atmosphere, p_{st} is static pressure, and Λ_v is the latent heat of vaporization.

The relative heat factor is defined as

$$b = \frac{LWC \cdot V \cdot \beta_0 \cdot c_{p,ws}}{h_c} \tag{D.11}$$

As was the case with β_0, h_c must be treated carefully when used for 3D applications. Given the 2D heat transfer coefficient, $h_{c,2D}$, Reshotko and Beckwith [49] showed that for incompressible flow over a wing with NACA 0012 section the 3D heat transfer coefficient is

$$h_{c,3D} = h_{c,2D} \sqrt{\cos(\Lambda)} \tag{D.12}$$

Because no correlation exists for the MS hybrid model from which to approximate the heat transfer coefficient, a correlation for a NACA 0012 airfoil with the same leading-edge diameter was used as a first order approximation.

Anderson [7] presents a method for estimating h_c based on the definition of the Nusselt number of air, Nu_a, which can be estimated at the stagnation line of a cylinder by the correlation given by Kreith [50] as

$$Nu_a = 0.992 Re_a^{0.5} \tag{D.13}$$

for glaze icing conditions and where Re_a is the Reynolds number of air using d for the reference length. This approximation for Nu_a on a cylinder was shown to also be a good approximation of Nu_a on a NACA 0012 airfoil in the IRT by Poinsatte [51] and was recommended for general use by Anderson [7].

The 2D h_c can then be found by the definition of Nu_a using the relationship

$$Nu_a = \frac{h_c d}{k_a} \tag{D.14}$$

where k_a is the thermal conductivity of air. Finally, for the MS hybrid model the 3D heat transfer coefficient is approximated using Equation (D.12) to correct the NACA 0012 of the same leading-edge diameter for the effect of sweep.

The gas phase mass transfer coefficient is then approximated by heat transfer analogy according to the method detailed by Anderson [7]. The relationship is given as

$$h_G = \frac{h_c}{c_{p,a}} \left(\frac{Pr_a}{Sc_a} \right)^{0.67} \tag{D.15}$$

where Pr_a and Sc_a are the Prandtl and Schmidt numbers, respectively, evaluated for air at the film temperature, $t_{\text{film}} = (t_s + t_{st})/2$. They are given by

$$Pr_a = \left(\frac{c_p \mu}{k} \right)_a \tag{D.16}$$

$$Sc_a = \left(\frac{\mu}{\rho D_v} \right)_a \tag{D.17}$$

where D_v is the diffusivity of water vapor in air. Because all the cases used in this thesis are for glaze icing conditions, the ratio $h_G/h_c = 4.81$ lb$_m$R/Btu (1.15 kgK/kJ) given by Anderson [7] for 0°C was used.

Tsao and Lee [43] recommend matching the Weber number based on leading-edge diameter in order to maintain surface water dynamic effects for glaze ice accretions. It is defined as

$$We_d = \frac{V^2 d \rho_w}{\sigma} \tag{D.18}$$

where σ is the surface tension of water against air. Matching the Weber number can be used to determine the tunnel test section speed when a scaled wing model is used. The models in the current research maintain a full-scale leading edge so that when the baseline velocity is able to be reached in the IRT test section, We_d is already matched. However, when the IRT velocity is limited either by tunnel capabilities or by model loads, the Weber number cannot be matched. When We_d cannot be matched due to velocity differences, the factor by which the scale and reference Weber numbers differ is simply the square of the ratio of the velocities.

References

[1] Leary, W., "We Freeze to Please: A History of NASA's Icing Research Tunnel and the Quest for Flight Safety," *The NASA History Series*, National Aeronautics and Space Administration, 2002.

[2] Bragg, M., Broeren, A., and Blumenthal, L., "Iced-airfoil aerodynamics," *Progress in Aerospace Sciences*, Vol. 41, No. 5, July 2005, pp. 323–362.

[3] Jeck, R. K., "Icing Design Envelopes (14 CFR Parts 25 & 29, Appendix C) Converted to a Distance-Based Format," *National Technical Information Services*, U.S. Department of Transportation Federal Aviation Administration, 2002.

[4] Bahrami, A., "Advisory Circular 25-25," *Code of Federal Regulations*, U.S. Department of Transportation Federal Aviation Administration, 2007.

[5] Lynch, F. T. and Khodadoust, A., "Effects of ice accretions on aircraft aerodynamics," *Progress in Aerospace Sciences*, Vol. 37, No. 8, Nov. 2001, pp. 669–767.

[6] Diebold, J., Broeren, A., and Bragg, M., "Aerodynamic Classification of Swept-Wing Ice Accretion," *Atmospheric and Space Environments Conference: Aircraft Icing*, American Institute of Aeronautics and Astronautics, 2013.

[7] Anderson, D. N., "Manual of Scaling Methods," *NASA/CR*, National Aeronautics and Space Administration, 2004.

[8] von Glahn, U. H., "Use of Truncated Flapped Airfoils for Impingement and Icing Tests of Full-Scale Leading-Edge Sections," *Research Memoranda*, National Advisory Committee for Aeronautics, 1956.

[9] Saeed, F., Selig, M. S., and Bragg, M. B., "Design of Subscale Airfoils with Full-Scale Leading Edges for Ice Accretion Testing," *Journal of Aircraft*, Vol. 34, No. 1, Jan. 1997, pp. 94–100.

[10] Saeed, F., Selig, M., Bragg, M., Saeed, F., Selig, M., and Bragg, M., "A hybrid airfoil design method to simulate full-scale ice accretion throughout a given C_l range," *Aerospace Sciences Meetings*, American Institute of Aeronautics and Astronautics, Jan. 1997.

[11] Saeed, F., Selig, M. S., and Bragg, M. B., "Hybrid Airfoil Design Method to Simulate Full-Scale Ice Accretion Throughout a Given α Range," *Journal of Aircraft*, Vol. 35, No. 2, March 1998, pp. 233–239.

[12] Saeed, F., Selig, M., Bragg, M., and Harold Addy, J., "Experimental validation of the hybrid airfoil design procedure for full-scale ice accretion simulation," *Aerospace Sciences Meetings*, American Institute of Aeronautics and Astronautics, Jan. 1998.

[13] Fujiwara, G. E., Woodard, B., Wiberg, B., Mortonson, A. J., and Bragg, M., "A Hybrid Airfoil Design Method for Icing Wind Tunnel Tests," *Fluid Dynamics and Co-located Conferences*, American Institute of Aeronautics and Astronautics, June 2013.

[14] Broeren, A. P., Potapczuk, M., Riley, J., Villedieu, P., Moens, F., and Bragg, M., "Swept-Wing Ice Accretion Characterization and Aerodynamics," *Fluid Dynamics and Co-located Conferences*, American Institute of Aeronautics and Astronautics, June 2013.

[15] Vassberg, J., Dehaan, M., Rivers, M., and Wahls, R., "Development of a Common Research Model for Applied CFD Validation Studies," *Guidance, Navigation, and Control and Co-located Conferences*, American Institute of Aeronautics and Astronautics, Aug. 2008.

[16] Eliasson, P. and Peng, S.-H., "Influence of Turbulence Modelling and Grid Resolution In Computations of the DPW4 CRM Configuration," *Aerospace Sciences Meetings*, American Institute of Aeronautics and Astronautics, Jan. 2010.

[17] Mani, M., Rider, B., Sclafani, A., Winkler, C., Vassberg, J., Dorgan, A., Cary, A., and Tinoco, E., "RANS Technology for Transonic Drag Prediction; A Boeing Perspective of the 4th Drag Prediction Workshop," *Fluid Dynamics and Co-located Conferences*, American Institute of Aeronautics and Astronautics, June 2010.

[18] Vassberg, J., "Introduction: Drag Prediction Workshop," *Journal of Aircraft*, Vol. 45, No. 3, May 2008, pp. 737–737.

[19] Hashimoto, A., Murakami, K., Aoyama, T., Yamamoto, K., Murayama, M., and Lahur, P., "Drag Prediction on NASA CRM Using Automatic Hexahedra Grid Generation," *Aerospace Sciences Meetings*, American Institute of Aeronautics and Astronautics, Jan. 2010.

[20] Sclafani, A., Vassberg, J., Mani, M., Winkler, C., Dorgan, A., Olsen, M., and Coder, J., "DPW-5 Analysis of the CRM in a Wing-Body Configuration Using Structured and Unstructured Meshes," *Aerospace Sciences Meetings*, American Institute of Aeronautics and Astronautics, Jan. 2013.

[21] Rivers, M. and Dittberner, A., "Experimental Investigations of the NASA Common Research Model (Invited)," *Fluid Dynamics and Co-located Conferences*, American Institute of Aeronautics and Astronautics, June 2010.

[22] Rivers, M., Hunter, C., and Campbell, R., "Further Investigation of the Support System Effects and Wing Twist on the NASA Common Research Model," *Fluid Dynamics and Co-located Conferences*, American Institute of Aeronautics and Astronautics, June 2012.

[23] Vassberg, J., Tinoco, E., Mani, M., Rider, B., Zickuhr, T., Levy, D., Brodersen, O., Eisfeld, B., Crippa, S., Wahls, R., Morrison, J., Mavriplis, D., and Murayama, M., "Summary of the Fourth AIAA CFD Drag Prediction Workshop," *Fluid Dynamics and Co-located Conferences*, American Institute of Aeronautics and Astronautics, June 2010.

[24] Bidwell, C. S. and Potapczuk, M. G., "Users Manual for the NASA Lewis Three-Dimensional Ice Accretion Code (LEWICE3D)," *TM 105974*, NASA, 1993.

[25] Wright, W., "Validation Results for LEWICE 3.0," *Aerospace Sciences Meetings*, American Institute of Aeronautics and Astronautics, Jan. 2005.

[26] Paul, B., Malone, A., and Vassberg, J., "Personal communications to the author," 2013.

[27] Robinson, B., Verhoff, A., and LaBozzetta, W., "Preliminary findings in certification of OVERFLOW," *Fluid Dynamics and Co-located Conferences*, American Institute of Aeronautics and Astronautics, June 1994.

[28] Jespersen, D., Pulliam, T., Buning, P., Jespersen, D., Pulliam, T., and Buning, P., "Recent enhancements to OVERFLOW," *Aerospace Sciences Meetings*, American Institute of Aeronautics and Astronautics, Jan. 1997.

[29] Buning, P. G., P., Chiu, I. T., Obayashi, S., Rizk, Y., and Steger, J., "Numerical simulation of the integrated space shuttle vehicle in ascent," *Guidance, Navigation, and Control and Co-located Conferences*, American Institute of Aeronautics and Astronautics, Aug. 1988.

[30] RENZE, K., BUNING, P., and RAJAGOPALAN, R., "A comparative study of turbulence models for overset grids," *Aerospace Sciences Meetings*, American Institute of Aeronautics and Astronautics, Jan. 1992.

[31] Bidwell, C., "Personal communication to the author," 2013.

[32] Vargas, M., "Current Experimental Basis for Modeling Ice Accretions on Swept Wings," *Journal of Aircraft*, Vol. 44, No. 1, Jan. 2007, pp. 274–290.

[33] DRELA, M. and GILES, M., "ISES - A two-dimensional viscous aerodynamic design and analysis code," *Aerospace Sciences Meetings*, American Institute of Aeronautics and Astronautics, March 1987.

[34] Drela, M., "XFOIL: An Analysis and Design System for Low Reynolds Number Airfoils," *Lecture Notes in Engineering*, edited by T. Mueller, Vol. 54, Springer Berlin Heidelberg, 1989, pp. 1–12.

[35] Bragg, M. B., *Rime Ice Accretion and Its Effect on Airfoil Performance*, Ph.D. thesis, Ohio State University, 1981.

[36] Selig, M. and Maughmer, M., "A multi-point inverse airfoil design method based on conformal mapping," *Aerospace Sciences Meetings*, American Institute of Aeronautics and Astronautics, Jan. 1991.

[37] McLean, D. J., *Understanding Aerodynamics Argueing from the Real Physics*, John Wiley & Sons Ltd., 2013.

[38] Anderson, D. A. and Steinbrenner, J. P., "Grid-Generation Methodology in Applied Aerodynamics," *Progress in Astronautics and Aeronautics*, American Institute of Aeronautics and Astronautics, 1990.

[39] Steinbrenner, J. and Abelanet, J., "Anisotropic Tetrahedral Meshing Based on Surface Deformation Techniques," *Aerospace Sciences Meetings*, American Institute of Aeronautics and Astronautics, Jan. 2007.

[40] Wenzinger, C., "Pressure distribution over an NACA 23012 airfoil with an NACA 23012 external-airfoil flap," *UNT Libraries*, National Advisory Committee for Aeronautics, 1938.

[41] Clark, K., Malinowski, M., Loth, E., Zante, J. V., Steen, L.-C., and Ide, R., "Air Flow and Liquid Water Concentration Simulations of the 2012 NASA Glenn Icing Research Tunnel," *Fluid Dynamics and Co-located Conferences*, American Institute of Aeronautics and Astronautics, June 2012.

[42] Wright, W., "A summary of validation results for LEWICE 2.0," *Meeting Paper Archive*, American Institute of Aeronautics and Astronautics, Jan. 1998.

[43] Tsao, J.-C. and Lee, S., "Evaluation of Icing Scaling on Swept NACA 0012 Airfoil Models," *NASA/CR*, National Aeronautics and Space Administration, 2012.

[44] Shah, A., Patnoe, M., and Berg, E., "Droplet size distribution and ice shapes," *Aerospace Sciences Meetings*, American Institute of Aeronautics and Astronautics, Jan. 1998.

[45] Papadakis, M., Rachman, A., Wong, S.-C., Yeong, H.-W., Hung, K., and Bidwell, C., "Water Impingement Experiments on a NACA 23012 Airfoil with Simulated Glaze Ice Shapes," *Aerospace Sciences Meetings*, American Institute of Aeronautics and Astronautics, Jan. 2004.

[46] Malone, A., "Personal communication to the author," 2013.

[47] RUFF, G., "Verification and application of the icing scaling equations," *Aerospace Sciences Meetings*, American Institute of Aeronautics and Astronautics, Jan. 1986.

[48] Bragg, M., Gregorek, G., and Shaw, R., "An analytical approach to airfoil icing," *Aerospace Sciences Meetings*, American Institute of Aeronautics and Astronautics, Jan. 1981.

[49] Reshotko, E. and Beckwith, I., "Compressible Laminar Boundary Layer Over a Yawed Infinite Cylinder with Heat Transfer and Arbitrary Prandtl Number," *NACA Rep. 1379*, National Advisory Committee for Aeronautics, 1957.

[50] Kreith, F., *Principles of Heat Transfer*, International Textbook Co., 1958.

[51] Poinsatte, P. E., "Heat Transfer Measurements from a NACA 0012 Airfoil in Flight and in the NASA Lewis Icing Research Tunnel," *NASA/CR*, National Aeronautics and Space Administration, 1990.